



HAL
open science

Precipitation in confined droplets - development of microfluidic and imogolite Pickering emulsion approaches

Tobias Lange

► **To cite this version:**

Tobias Lange. Precipitation in confined droplets - development of microfluidic and imogolite Pickering emulsion approaches. Other. Université Paris Saclay (COMUE), 2019. English. NNT : 2019SACLV069 . tel-03035023

HAL Id: tel-03035023

<https://theses.hal.science/tel-03035023>

Submitted on 2 Dec 2020

HAL is a multi-disciplinary open access archive for the deposit and dissemination of scientific research documents, whether they are published or not. The documents may come from teaching and research institutions in France or abroad, or from public or private research centers.

L'archive ouverte pluridisciplinaire **HAL**, est destinée au dépôt et à la diffusion de documents scientifiques de niveau recherche, publiés ou non, émanant des établissements d'enseignement et de recherche français ou étrangers, des laboratoires publics ou privés.

Precipitation in Confined Droplets - Development of Microfluidic and Imogolite Pickering Emulsion Approaches

Thèse de doctorat de l'Université Paris-Saclay
préparée à l'Université de Versailles-Saint-Quentin-en-Yvelines

Ecole doctorale n°573 Interfaces -
Approches Interdisciplinaires: Fondements, Applications et Innovation
(Interfaces)
Spécialité de doctorat: chimie

Thèse présentée et soutenue à Gif-sur-Yvette, le 22.11.2019, par

Tobias Lange

Composition du Jury:

Hafsa Korri-Youssofy Directrice de Recherche, Université Paris-Sud (UMR 8182)	Présidente
Barbara Bonelli Prof. Associato Confermato, Politecnico de Torino (DiSAT)	Rapporteuse
Sébastien Teychené Maître de conférences, INP Toulouse (UMR 5503)	Rapporteur
Laurent Michot Directeur de Recherche, Sorbonne Université (UMR 8234)	Examineur
Romain Grossier Chargé de recherche, Aix-Marseille Université (UMR 7325)	Examineur
Fabienne Testard Chercheur CEA, CEA Paris-Saclay (UMR 3685)	Directrice de thèse
Sophie Charton Chercheur CEA, CEA Marcoule (SA2I)	Co-directrice de thèse
Antoine Thill Chercheur CEA, CEA Paris-Saclay (UMR 3685)	Co-directeur de thèse
Florent Malloggi Chercheur CEA, CEA Paris-Saclay (UMR 3685)	Invité

Acknowledgements

I would like to express my thorough gratitude to Fabienne Testard and Sophie Charton for the challenging and interesting topic, their support and their mentorship during my stay in France.

Furthermore, I would like to thank Antoine Thill for synthesizing the imogolite samples, his input and guiding me through the field of imogolite.

I would also like to thank Florent Malloggi for teaching me microfluidics and all our discussions around this topic.

Additionally, I wish to acknowledge the help provided by: Thibault Charpentier and Mélanie Moskura for discussions, practical guidance regarding the preparation of MAS NMR sample holders and for conducting the actual NMR experiments; Frédérick Gobeaux for his practical work and guidance regarding TEM investigations; Olivier Taché for his practical help and discussions regarding SAXS and Python; Geraldine Carrot for the discussions and her efforts regarding the work on polydopamine; Patrick Guenoun for his help regarding AFM measurements; Philippe Surugue and Thierry Bernard for their help and practical work in creating sample holders for microfluidics; Elodie Barruet for her help in and around the laboratory; Pierre Picot for our plentiful discussions regarding imogolite; and also all former and current members of the *Laboratoire Interdisciplinaire sur l'Organisation Nanométrique et Supramoléculaire*.

I would also like to acknowledge funding for the thesis from the CEA *amont-aval* program.

Furthermore, I am thankful for the provided beamtime by the synchrotron SOLEIL at the beamline SWING and the support of Thomas Bizien and all people that participated to the experimental session (proposals 20181598 and 20181790).

FEGSEM & EDX instrumentation was facilitated by the *Institut des Matériaux de Paris Centre* (IMPC FR2482) and was funded by *Sorbonne Université*, CNRS, and by the C'Nano projects of the *Région Ile-de-France*.

(Cryo-)TEM observations were made, thanks to "*Investissements d'Avenir*" LabEx PALM (ANR-10-LABX-0039-PALM).

TEM observations were performed at the "TEM-team" platform (iBiTec-S/SB2SM).

Finally, I would like to thank my friends, my family and especially Stefanie for their support during these three years abroad.

Contents

I	General Introduction	1
II	A Droplet Microfluidic Device for In-situ Small Angle X-ray Scattering Studies	5
1	Introduction	5
2	Fundamentals	8
2.1	Microfluidics	8
2.2	Small Angle X-ray Scattering	14
2.3	Combining SAXS and Microfluidics	19
2.4	Isolating the Droplet Signal	19
3	Materials and Methods	21
3.1	Microfluidic Device Fabrication	21
3.2	Characterization of OSTE+ Microfluidic Devices	25
3.3	Microfluidic experiments	26
3.4	X-ray Scattering Experiments	28
4	Results and Discussion	29
4.1	Microfluidic Device Fabrication	29
4.2	Characterization of OSTE+ Microfluidic Devices	32
4.3	Results from Bench-top Experiments	35
4.4	OSTE+ X-ray Characterization	41
4.5	Results from the In-situ SAXS Synchrotron Experiments	46
5	Conclusion and Perspective	60
III	Transformation of Imogolite into a Lamellar Phase with Interfacial Properties by Decylphosphonic Acid	63
1	Introduction	63
2	Materials and Methods	70
2.1	Synthesis of Imogolite	70
2.2	Reaction of Decylphosphonic Acid and Imogolite	70
2.3	Infrared Spectroscopy	71

2.4	Magic Angle Spinning Nuclear Magnetic Resonance Spectroscopy .	72
2.5	Small Angle X-Ray Scattering	72
2.6	Scanning Electron Microscopy	73
2.7	Transmission Electron Microscopy	73
2.8	Fluorescence Microscopy	73
2.9	Dispersibility, Emulsification and Interfacial Activity	73
3	Results and Discussion	74
3.1	Reaction of Imogolite and Decylphosphonic Acid	74
3.2	Dispersibility, Emulsification and Interfacial Activity	86
4	Conclusion and Perspective	87
IV	Advances for the Surface Modification of Imogolite	89
1	Introduction	89
2	Materials and Methods	90
2.1	Synthesis of Imogolite	90
2.2	Dispersion Tests	91
2.3	Dialysis	91
2.4	Polymerization of Dopamine	91
2.5	Characterization	93
3	Results and Discussion	94
3.1	Dispersion Tests	94
3.2	Dialysis	96
3.3	Polymerization of Dopamine	99
4	Conclusion	106
V	General Conclusion and Perspective	107
A	Appendix - Characterization of Gold Nanoparticles	I
B	Appendix - Microfluidic Device Holders	III
C	Appendix - Python 3 Code for In-situ SAXS Data Treatment	V
D	Appendix - Additional In-situ SAXS Data	XI
E	Appendix - ²⁷Al MAS NMR Deconvolution of Imogolite Samples	XIII
F	Appendix - Conductivity Measurements	XV

G	Appendix - Dialysis of Methyl Modified Imogolite	XIX
H	Appendix - Additional AFM Images of Imogolite Samples	XXI
I	Appendix - Résumé français	XXVII

I General Introduction

Oxalic acid is a ubiquitous molecule in everyday life. In its anionic form, it is present in most plant families, as a part of different compounds.^[1,2] Insoluble calcium oxalate regulates the calcium levels of plants and acts as protection against herbivores.^[2] The consumption of such plants can lead to the formation of kidney stones, which are a common ailment in modern society.^[2-4] Approximately 80 % of the stones consist of calcium oxalate.^[3,4] Apart from this direct dietary impact, oxalic acid is also encountered in other aspects of life. In beekeeping, for example, it is applied as pest control against the *Varroa* mite.^[5] Furthermore, it is a common precipitant for the recovery of rare earths or actinides in solvent extraction processes.^[6-10]

In precipitation, similar process conditions can yield different polymorphs of a material, which can be detrimental to their usefulness in a specific application.^[11,12] For the above-mentioned application of oxalic acid as precipitant for metal ions, the precipitate properties, e.g. the particle size distribution and the habit have an influence on the ability to separate the precipitate from its mother liquor. Precipitation is a topic of general interest, since it is not only used in metallurgy, but also in other processes, such as the production of pigments, plant protection and pharmaceuticals. In contrast to crystallization, which generally happens at low supersaturation levels, precipitation describes the fast formation of a badly soluble substance from solutions at high supersaturation ratios.^[13] For both cases, nuclei can form from a solution of monomers, as soon as the solution is suitably supersaturated. In the following, these nuclei grow by consuming monomers, reducing the concentration of the solution to its equilibrium value. Classically, such a process is described via the LaMer diagram (Figure I.1), separating the process into different stages. In reality, the formation of a particle can be more complex. Different pathways of crystallization have been evidenced during the last years that cannot always be explained by classical crystallization theory.^[14] Precipitation reactions are even more difficult to study, since precipitation is fast and the involved processes like mixing, nucleation, growth and aggregation can take place at the same time rather than sequentially.^[13] It is however essential to understand how the particles are formed to control the precipitate's properties.^[15]

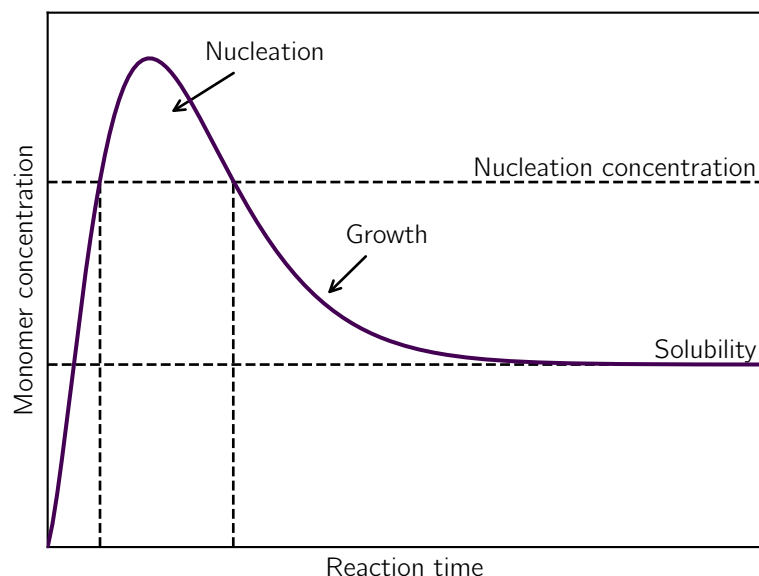


Figure I.1: LaMer diagram describing a separated nucleation and growth process. After initiation, the monomer concentration increases. When a certain concentration is exceeded, nucleation starts and the monomer concentration decreases. As soon as the concentration falls below the nucleation threshold, no more nuclei are formed and the already existing nuclei grow from the monomers in solution until the respective equilibrium concentration is reached.

Cerium oxalate is one of the many compounds for which there is a strong interest in controlling the precipitate shape. However, so far almost nothing is known about its formation mechanisms. It is a precursor of cerium oxide, which has many technological applications, among others, mimicking several biorelevant activities,^[16] as a surrogate for plutonium oxide^[17] and as a catalyst.^[18] When synthesized from cerium oxalate, the shape of the precursor particles was shown to directly influence the shape of the final cerium oxide particles and consequently their catalytic properties, e.g. for the oxidation of carbon monoxide.^[19] Cerium oxalate is also used as substitute to study the oxalic acid precipitation of plutonium, without actually using radioactive material.^[9] Although the precipitate can be influenced by experimental parameters,^[9,20,21] the fundamental mechanisms in the formation of cerium oxalate are not well understood. Cerium oxalate can be precipitated by oxalic acid from aqueous cerium nitrate solutions as cerium oxalate decahydrate^[22]:



Different observations have been made for the formation of cerium oxalate particles. In

an emulsion based synthesis, the formation of 20 nm sized primary particles was described that aggregated and formed spheres. Direct mixing, however, yielded divergent particle morphologies.^[21,23–25] Beyond that, an intermediate amorphous phase has been identified before crystal formation.^[25] The particle morphologies have also been reported to depend on concentration ratios, temperature, the order of addition and the used solvent.^[21,23,26,27] By switching from water to mixtures of water and organic molecules as solvent, the thereby induced nanostructuration of the solvent was observed to influence the aggregation behaviour and the shape of the formed particles.^[26,27] Identification of the dominating mechanisms during particle formation might be the crux to understand this rich behaviour.

The presented thesis concentrates on the development of new approaches to investigate and control the first instants of precipitation reactions by locally confining them into droplets with a focus on the formation of cerium oxalate. Two directions were explored in this work:

i) Studying the reactivity of a precipitating system. Based on the success of droplet microfluidic devices to study the nucleation rate of neodymium oxalate^[28] and to observe gold nanoparticles by SAXS,^[29] the first chapter focuses on the development of a droplet microfluidic tool able to withstand organic solvents and compatible with SAXS. A protocol is presented to prepare thin microfluidic devices from off-stoichiometry thiol-ene-epoxies. The material is characterized regarding its suitability to perform microfluidic in-situ SAXS experiments. Furthermore, the experimental conditions to study cerium oxalate reactivity in the developed device are explored and an original approach that allows isolating the SAXS patterns of droplets and carrier phase from microfluidic in-situ experiments is presented. The results are a first step and guide the path for future kinetic and mechanistic investigations of the cerium oxalate system and other fast reacting systems in which crystallization or precipitation plays a role, e.g. the production of pigments, catalysts, plant protection and pharmaceuticals.

ii) Controlled reactant feeding through imogolite nanotubes. Mixing and more generally transport phenomena play a major role in the course of a precipitation reaction. In the case of emulsion precipitation,^[8,9,23,26] transport can be triggered by the coalescence of droplets containing the different reagents. Hence, it is rather difficult to obtain control over the process. The second chapter was inspired by the stabilization of droplets by imogolite Pickering emulsions, which might be an innovative way of controlling reactant transport into droplets.^[30] Imogolite Pickering emulsions might also be a facile way to study the transport properties of imogolite experimentally. Before imogolite nanotubes can

form water-in-oil Pickering emulsions, their surfaces need to be hydrophobized. The most commonly used approach from literature was used to hydrophobize imogolite and in order to obtain coalescence stabilized Pickering emulsions. However, the surface modification approach from literature was evidenced to actually degrade the imogolite structure by conducting the first thorough characterization of the reaction product.

Consequently, in the third chapter new pathways to achieve surface modification of imogolite are explored.

II A Droplet Microfluidic Device for In-situ Small Angle X-ray Scattering Studies

1 Introduction

Small angle X-ray scattering (SAXS) probes structural features in the range of approximately 1 nm to 1 μm , making it an ideal tool to study the structure, organization and dynamics of matter.^[31–34] The technique gives information about the characteristic shape, the average size, polydispersity, internal composition, inter-particle interactions and organization of a sample.^[35,36] Additionally, information about the dynamics of a system is accessible when the sample is out of equilibrium and time-resolved SAXS is used to follow the temporal sample evolution. For a typical experiment, the sample is prepared by introducing it into a sample environment (e.g. a quartz capillary) and the corresponding scattering pattern is collected. If the sample changes over time, slow kinetics can be observed by repeatedly acquiring the scattering pattern of the same sample under static conditions or under continuous flow.^[37] For fast kinetics, the problem is however more complex and different approaches have to be used. As a precondition, the acquisition time has to be shorter than the reaction time to obtain a sufficiently high temporal resolution, making it necessary to use a high brilliance X-ray source. Additionally, the out of equilibrium state has to be reached fast enough to decouple the evolution of the system from the change of state. Different strategies have been developed to explore the transformations, e.g. rapid mixing, a pressure jump or a temperature jump.^[38]

One of the most frequently used ways to obtain fast mixing are stopped flow apparatuses.^[39] Therein, the samples are rapidly mixed and injected into a sample chamber with an abrupt stop of the flow. This method allows mixing of a sample within a few milliseconds and gives access to the very first moments of a process.^[39] The obtained scattering patterns allow to follow the process over time and to identify intermediate steps. Time-resolved SAXS has been applied to study micellar transformations^[40] or the nucleation and growth of gold nanoparticles,^[37,41] quantum dots^[42] and metal organic frameworks.^[43] In these and many

other studies,^[31] the time-resolution of SAXS was crucial to identifying the presence of intermediate steps and to understand the evolution of a system.

Microfluidic devices can also be used as a sample environment for SAXS studies.^[44–46] They are used to manipulate fluids in channels with a characteristic length scale from 1 to 1000 μm . As a consequence, the dominating physical phenomena are different from what we are generally used to in our macroscopic environment.^[47]

For example, the flow pattern of fluids inside microfluidic channels is generally laminar rather than turbulent, meaning each fluid molecule moves parallel to the channel borders instead of chaotically as in turbulent flow. As a result, two separate fluid streams that are joined will not mix automatically, but rather flow side by side and mainly mix by diffusion. This process was utilized in the first combination of SAXS and microfluidics in a hydrodynamic focusing device to study protein folding.^[48,49] By reducing the diffusion path a molecule needs to travel in order to obtain mixing, fast mixing times were achieved.^[50] Time-resolution is obtained through the relation between the relative position of the probed local point and the fluid velocity. Thus, each position along the channel corresponds to a reaction time. This allows probing each reaction time for an extended period, improving the data quality. The mixing time in hydrodynamic focusing depends on diffusion, which can render the approach too slow for some systems. To decrease the mixing time, turbulent^[51,52] or chaotic^[53] micro mixers have been developed. In such devices, a mixing part rapidly mixes the fluids before the conditions go back to laminar flow for observation.

Yet another way of mixing reactants in microfluidics is by creating a segmented flow of two immiscible phases.^[54,55] The created droplets have at least two advantages over continuous phase microfluidics. The segmentation prevents reactant dispersion along the channel axis due to absence of an undisturbed laminar flow profile, which is beneficial to the determination of the actual reaction time of the probed local point.^[55] Furthermore, the confinement of the reactants inside the droplets potentially prevents channel fouling by reactive species that would adsorb to the channel wall in single-phase flow.

Such segmented flow microfluidic devices were first combined with X-ray diffraction for protein crystallography.^[56] The droplets were generated in a microfluidic device, transferred into a capillary and then analyzed under static conditions.

The first work on the combination of SAXS with droplets under flow was presented by Stehle et al.^[29] They combined a polydimethylsiloxane (PDMS) device for droplet generation with glass capillaries for analysis, and collected the signal of pre-synthesized gold nanoparticles and gold nanoparticles under formation. A 50 μm \times 300 μm (vertically \times horizontally) X-ray

beam was used to obtain the scattering signal of the particles, and the signal was integrated over the whole fluid volume, i.e. droplets and carrier phase.

To overcome this limitation, Pham et al. synchronized the shutter and the detector to the passing droplets, so that only signal from droplets was acquired.^[57,58] They prepared a droplet generation device from Norland Optical Adhesive (NOA 81) and coupled it to a 300 μm quartz capillary which was placed under vacuum for SAXS acquisition. A beam of 90 μm \times 165 μm (vertically \times horizontally) was used and yielded 1 to 3 scattering images per droplet at fluid velocities from 1 to 1.4 $\text{mm} \cdot \text{s}^{-1}$. The experiment allowed them to study the impact of NaCl concentration on lysozyme in solution.

In the same year, Saldanha et al. published their approach on coupling SAXS with droplet microfluidics to study the transformation of rod-shaped vimentin into filaments upon salt addition.^[59] They used a Polydimethylsiloxane (PDMS) microfluidic device similar to the one of Zheng et al.^[56] and acquired the scattering signal in a 100 μm diameter quartz capillary with a microfocus beam of 10 μm \times 8 μm (vertically \times horizontally) and a fluid velocity of 5 $\text{mm} \cdot \text{s}^{-1}$. By using short acquisition times, they were able to collect separated scattering patterns for the oil phase, the water droplets and the oil-water interface. The water droplet signal was isolated based on the higher absorbance of the oil and the streak signal from the interfaces. For each probed position, the droplet signal was averaged and related to the reaction time through the fluid velocity.

Levenstein et al. used the same approach to isolate the droplet signal as Saldanha et al. and combined it with X-ray diffraction.^[60] The channel geometry was laser-cut into a polytetrafluoroethylene sheet, which was sandwiched between two layers of polyimide and clamped together by screws and Poly(methyl methacrylate) (PMMA) plates. A slit along the PMMA holder allowed the acquisition of scattering patterns at fixed points along a serpentine channel geometry. The data was collected from a 300 μm \times 300 μm channel with X-ray beams of 12 μm \times 15 μm (vertically \times horizontally) and 80 μm \times 320 μm (vertically \times horizontally) with fluid velocities of 4.8 and 5.9 $\text{mm} \cdot \text{s}^{-1}$. They characterized their device by determining the detection limit of 12 nm magnetite ($\approx 0.31\%$ by weight) and 15 nm gold nanoparticles ($\approx 0.05\%$ by weight). Additionally, they measured the induction time of CaCO_3 crystallization in presence of different nucleants.

To combine SAXS and microfluidics, the used material is required to be compatible with the X-ray experiment and it should facilitate manufacturing relatively thin walls to reduce background scattering. Different materials can be used for the channel geometry and for the walls that close the geometry. While PDMS is probably the most used material to

manufacture microfluidic devices and can be used for SAXS studies, it exhibits high X-ray absorption, strong scattering and is susceptible to beam damage.^[61] Polyimide* is resistant to X-rays^[62] and was used as a window material to close the channel geometry and to make complete devices.^[60,63–66] Polystyrene (PS) was shown to exhibit adequate properties in combination with X-rays and was used to prepare devices^[67,68] and windows.^[64] Silicon nitride was used for windows.^[69] UV curable thiol-ene polymers were also used to make devices.^[70,71] A cyclic olefin copolymer (COC) was shown to be a suitable material for the preparation of complete devices, too.^[72] Off-stoichiometry thiol-ene^[64] (OSTE) and off-stoichiometry thiol-ene-epoxies^[25,73] (OSTE+) were used in combination with different window materials. However, no devices for in-situ SAXS were made from OSTE+ alone. OSTE+ is a relatively new polymer class for microfluidics, based on the OSTE platform, and only a few protocols to prepare microfluidic devices therefrom have been reported.^[25,74–79]

After giving some of the fundamentals, a protocol on how to prepare a microfluidic device from OSTE+ alone and in combination with polyimide windows will be presented. To examine if OSTE+ can be used for in-situ SAXS experiments, it will be characterized regarding its X-ray compatibility. Additionally, the preliminary bench-top experiments required to define the working conditions for the droplet microfluidic SAXS experiments and the results from the first experimental run at the synchrotron facility SOLEIL will be presented. A custom computer code is developed and used to isolate the droplet and oil signal. The approach is then used to observe gold nanoparticles under continuous flow and in droplets, and to investigate the formation of oxalate particles in water and in a nanostructured binary solvent of 1,2-propanediol and water.

2 Fundamentals

2.1 Microfluidics

Dimensionless Numbers

In microfluidics, the characteristic length scales range from 1 to 1000 μm . Therefore, the dominating physical phenomena differ from our everyday experience. Similarly to other flow systems, dimensionless numbers can be used to characterize microfluidic systems. The dimensional analysis is a convenient way to compare the magnitude of the involved

*commercially available as Kapton

phenomena and to identify the governing phenomenon under given experimental conditions. An in-depth review on dimensionless numbers relevant for microfluidic applications is given by Squires and Quake.^[47] As diffusion, inertia and capillary forces are the main relevant mechanisms in microfluidics, the dimensionless numbers are generally based on the following physical properties and experimental parameters: the density ρ , kinematic viscosity ν , dynamic viscosity $\eta = \nu \cdot \rho$, the surface tension γ , the diffusion coefficient D , the characteristic velocity of the fluid u and the characteristic length scale L . For microfluidics the latter is generally the hydraulic diameter d_h of the microfluidic channel. The hydraulic diameter is defined as:

$$d_h = 4 \cdot \frac{A}{P}, \quad (\text{II.1})$$

where A is the cross-sectional area of the channel and P is the wetted perimeter.

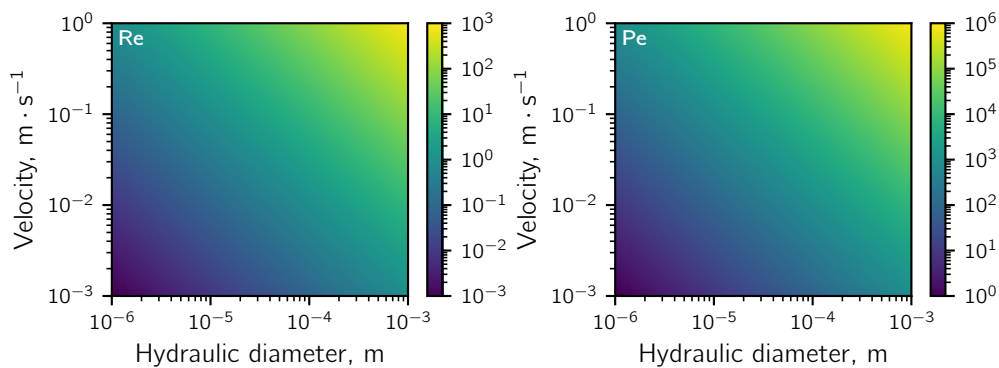


Figure II.1: Left: Typical numerical values of the Reynolds number for water ($\nu = 1 \cdot 10^{-6} \text{ Pa} \cdot \text{s}$) at different hydraulic diameters and fluid velocities. **Right:** Typical numerical values of the Péclet number for small ions in water ($D = 1 \cdot 10^{-9} \text{ m}^2 \cdot \text{s}^{-1}$).

The Reynolds number (Re) relates inertial forces to viscous forces and is defined as:

$$\text{Re} = \frac{u L}{\nu}. \quad (\text{II.2})$$

It gives an indication about the flow regime. Figure II.1 shows values of Re for typical channel diameters and fluid velocities encountered in microfluidics. For $\text{Re} < 1000$ in a straight microchannel the flow is typically laminar, which means that the fluid moves parallel to the channel wall. The flow only becomes turbulent for higher values of Re. Consequently, the fluid molecules are not mixed by convection and diffusion dominates.

The Péclet number (Pe) relates the convection to the diffusion fluxes for a transported

species:

$$Pe = \frac{uL}{D}. \quad (II.3)$$

It enables to estimate the necessary channel length that is required to achieve complete mixing. Figure II.1 shows Pe for a solute ion with a typical diffusion coefficient in the order of $1 \cdot 10^{-9} \text{ m}^2 \cdot \text{s}^{-1}$. Assuming a hydraulic diameter of $100 \text{ } \mu\text{m}$ and a velocity of $1 \text{ mm} \cdot \text{s}^{-1}$ a Pe of 100 is obtained. This means that it would take around 100 channel widths ($\approx 1 \text{ cm}$) for the fluid to mix completely. For larger solutes like proteins with slower diffusion coefficients ($\approx 1 \cdot 10^{-11} \text{ m}^2 \cdot \text{s}^{-1}$) this can be either exploited to separate objects with higher diffusion coefficients or it can be a problem if mixing is desired.^[47] To mix the fluid faster, the channel geometry has to be modified to create a turbulent flow.^[80] Another possibility is to segment the flow into droplets. The droplets have internal flow patterns that were found to mix the content with a mixing time that is logarithmically proportional to Pe .^[81]

When two immiscible fluids are introduced into a microfluidic channel, the surface tension tries to minimize the surface area between them, while the viscous forces drag the interface downstream. The capillary number (Ca) relates the viscous forces to the surface tension:

$$Ca = \frac{\eta u}{\gamma}. \quad (II.4)$$

It allows to estimate the droplet radius $R \propto Ca^{-1}$ and if droplets are likely to be created or not.^[47] For low numbers of Ca droplets will form, while at higher numbers viscosity dominates and tends to form a co-flow of both phases.^[82] Figure II.2 shows capillary numbers for a fluid velocity of $1 \text{ m} \cdot \text{s}^{-1}$.

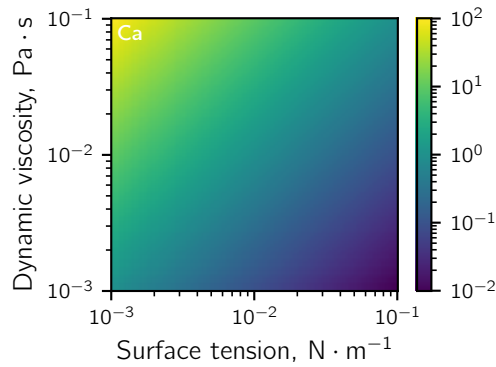


Figure II.2: The capillary number at a fluid velocity of $u = 1 \text{ m} \cdot \text{s}^{-1}$.

Preparation of Microfluidic Devices

Nowadays, microfluidic systems can be prepared from different materials and by various techniques.^[83–85] The first devices, however, were etched into silicon and glass with the help of photolithography.^[85–87] The high cost associated with these techniques stimulated the development of other preparation techniques and promoted the use of other materials, mostly polymers or even paper.^[83–86] Polymers have the advantage of being relatively cheap, available and processable. The probably most used polymer for scientific applications is polydimethylsiloxane (PDMS). It can be cast against a master mold and then be used to prepare a microfluidic device or be used as a mold itself in soft lithography.^[88–90] The master can be prepared in any way e.g. machining or photolithography. For photolithography (Figure II.3), a so called mask is required to create 3D structures from a photoresist. The first step in this procedure is to draw the mask, which defines the microfluidic channel structure, with a computer-aided design program and to print it on a transparent sheet of polymer. In the second step, a flat substrate is coated with a photoresist. After aligning the printed design to the substrate, it is irradiated with light of a certain wavelength to initiate a polymerization reaction in the photoresist. The parts that are protected by ink do not react and can be removed after the polymerization is finished, e.g. by selective dissolution. To obtain the PDMS mold, liquid PDMS monomers are cast against the master and polymerized at elevated temperatures (Figure II.4). The obtained PDMS replica is then usable as part of a microfluidic device or as a mold itself.

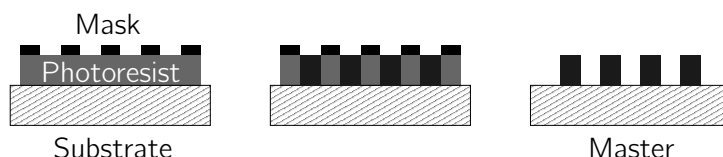


Figure II.3: Photolithographic process. **Left:** The mask is aligned to the substrate and the layer of photoresist. **Center:** The assembly after exposure to light. The exposed parts of the photoresist are polymerized. **Right:** 3D structures are created by dissolving the unreacted photoresist.

Off-Stoichiometry Thiol-Ene-Epoxyes

Off-stoichiometry thiol-ene-epoxyes (OSTE+) are a relatively new class of polymers for the preparation of microfluidic systems.^[91] They were developed from the off-stoichiometry thiol-enes polymer platform^[92] and are commercially available from Mercene Labs AB,

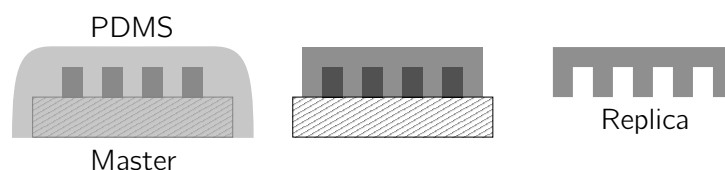


Figure II.4: Replication molding process. **Left:** PDMS monomers are cast against the master. **Center:** After heat exposure PDMS is cured and can be cut free. **Right:** 3D structures are replicated after demolding the PDMS piece.

Sweden. The liquid pre-polymer is composed of thiol, alkene and epoxide monomers (Table II.1), a photoinitiator and a photolatent base.^[93] After mixing, it can be cast against a PDMS mold for soft lithography. For OSTE+ the first curing step is initiated by UV radiation and is based on thiol-ene click chemistry.^[94] The resulting polymer is flexible and sticky when touched. In the second curing step the epoxide groups react with the excess thiol groups under the influence of heat and the polymer stiffens when it is cooled down.^[93] The second curing step can be used to bond the OSTE+ to other surfaces via the epoxy chemistry. Before the final curing step, the excess surface thiol groups can also be used for surface modification.^[95]

Table II.1: Generic functional groups in the OSTE+ pre-polymer.

Thiol	Alkene	Epoxide
$R-S-H$	$R-CH=CH_2$	$R-CH \begin{array}{c} \diagup O \diagdown \\ -CH_2 \end{array}$

Droplet Microfluidics

In the following, the most basic ideas regarding droplet microfluidics will be summarized. For more in-depth information, many reviews are available on this vast topic.^[96–103]

To generate droplets, two immiscible fluids have to be introduced into one microchannel. This happens usually by applying a direct pressure difference between the inlet and the outlet or by using syringe pumps that drive the fluids at a certain flow rate. The use of two fluids creates new requirements regarding the device material since it should be resistant to both. PDMS, for example, tends to release oligomers or swells when brought into contact with certain organic fluids.^[104] Another consideration that has to be made beforehand is

the phase preference of the used materials. To obtain water droplets in an oil phase, the channel walls should be hydrophobic so that the oil phase wets the walls and the water droplets do not. If the wetting behavior is not sufficient, it can also be influenced by the addition of surfactants.^[105,106] Adding surfactants or particles also helps stabilizing the formed droplets.^[105,107] When choosing a surfactant, special care should be taken so that the surfactant does not influence the droplet content.^[108]

Active and passive methods can be used for the generation of droplets. While active methods make use of electrical, thermal, magnetic and mechanical controls, passive methods rely on the geometry, the flow rates and the physico-chemical properties of the system alone.^[98,99] The three principle geometries to generate droplets are co-flow, flow focusing and cross flow (Figure II.5). In co-flow, the two phases meet in flow direction (parallel streamlines),

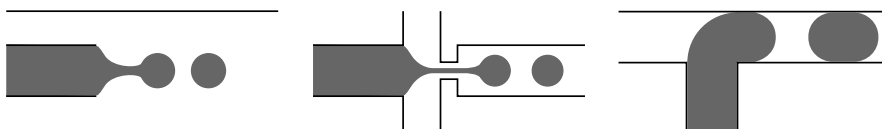


Figure II.5: Examples for different droplet generation geometries for a fluid flow. **Left:** Co-flow. **Center:** Flow focusing. **Right:** Cross flow (T-junction).

while they meet at an angle in cross flow. For flow focusing, an obstruction narrows down the channel to promote the droplet formation.^[103] The T-junction is the simplest example for the cross flow geometry and was used in the first report on droplet generation.^[109] As predicted by the capillary number, the droplet generation pattern depends on the flow rates, the fluid viscosities and the channel geometry.^[110] Three principle flow behaviors can be observed for the T-junction: squeezing, dripping and jetting (Figure II.6).^[97,98,111]

Squeezing is observed at low capillary numbers. The dispersed phase protrudes into the continuous phase and fills the channel. As the distance between the dispersed phase and the channel wall decreases the pressure in the carrier phase increases. When the pressure is larger than the pressure of the dispersed phase, a neck forms and the liquid breaks at this point. This position is referred to as pinch-off position. The formed droplets are highly monodisperse^[112] and have an elongated shape due to their high volume that is constrained by the channel geometry.

Dripping appears when the capillary number is increased and the viscous forces start to dominate the interfacial stabilization of droplets. Droplet break-up occurs close to the junction, but the dispersed phase does not touch the opposite wall before pinch-off. The droplets are also monodisperse but smaller than in the squeezing regime.

Jetting occurs for high capillary numbers. The dispersed phase is pulled downstream into the carrier phase and breaks into small polydisperse droplets due to the Plateau-Rayleigh instability^[113] of the liquid thread.

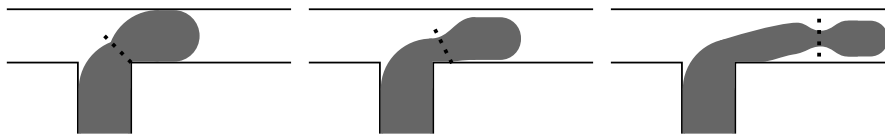


Figure II.6: Droplet flow behaviours in a T-junction. The carrier phase flows from left to right. The dotted line indicates the pinch-off position. **Left:** Squeezing. **Center:** Dripping. **Right:** Jetting.

For a droplet that flows in a straight channel the shear stress at the channel walls create circulating flow patterns inside the droplet. The patterns are symmetrical and parallel to the flow direction of the droplet. While mixing is promoted along the flow axis, it remains slow and stays dominated by diffusion across the symmetry axis. To overcome this limitation, chaotic advection can be introduced by a winding channel geometry.^[81] When passing the winding channel, the interface between the two droplet halves reorients into the flow direction and the droplet content is folded and stretched, which leads to faster mixing.^[81] The mixing time t_{mix} was found to scale for high Pe as:

$$t_{mix} \sim \left(\frac{a d_h}{u} \right) \log (Pe), \quad (II.5)$$

where a is the dimensionless droplet length measured relative to the hydrodynamic diameter of the microfluidic channel d_h . Mixing times as rapid as $\approx 500 \mu s$ have been achieved in a microchannel with a hydrodynamic diameter of $10 \mu m$ at fluid velocities of $400 \text{ mm} \cdot \text{s}^{-1}$.^[81] Such low mixing times allow to decouple mixing and reactivity to probe reaction kinetics.^[54]

2.2 Small Angle X-ray Scattering

In the following, some basics regarding SAXS will be discussed that are necessary throughout the manuscript. More details on this topic can be found in specialized articles and books.^[33,34,114–116]

X-ray radiation has a wavelength between 0.01 and 10 nm. Upon interaction with matter, it can be absorbed or scattered. Absorption of X-rays depends on the atomic species present in the material and on the energy of the radiation. The mass attenuation coefficient $\left(\frac{\mu}{\rho} \right)$

describes the property of a material to be penetrated by X-rays of a certain energy. It is tabulated^[117] for different atoms and is calculated from the linear attenuation coefficient μ and the density ρ . To calculate the mass attenuation coefficients of any material $(\frac{\mu}{\rho})_x$, the coefficients of its components in their respective mass ratio need to be summed up:

$$(\frac{\mu}{\rho})_x = \sum \frac{m_i}{m_x} (\frac{\mu}{\rho})_i. \quad (11.6)$$

The transmitted intensity I_T of an incident intensity I_0 is:

$$I_T = I_0 e^{(-\mu d_s)}, \quad (11.7)$$

where d_s is the sample path length. The transmittance is defined as the ratio of transmitted intensity over incident intensity:

$$T = \frac{I_T}{I_0}. \quad (11.8)$$

Upon interaction with an atom, the X-ray can also be scattered by its electrons, either with loss of energy (Compton or inelastic scattering) or without energy loss (Thomson or elastic scattering). In elastic scattering, the incident wave causes the electron to emit radiation at the same wavelength. Hence, all the atoms in a particle that scatter the incident radiation emit the scattered radiation at the same wavelength, which enables it to interfere. The interference patterns carry the structural information of the particle.

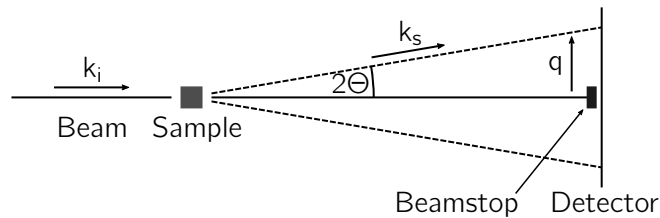


Figure II.7: Schematic representation of a SAXS experiment showing the incident, the transmitted and scattered part of the beam.

A scheme of a typical scattering experiment is depicted in Figure II.7. The incident beam of wavelength λ hits the sample and propagates until it is absorbed by a so called beamstop, which protects the 2D detector. A beamstop is necessary because the dynamic range of the detector is limited and the incident beam is highly more intense than the scattered part of the beam. The number of scattered photons is measured by the detector as a function of the scattering angle 2Θ . In the SAXS experiment, the magnitudes of the incident and

scattered wave vectors are equal:

$$|\vec{k}_i| = |\vec{k}_s| = \frac{2\pi}{\lambda}. \quad (\text{II.9})$$

The scattering vector is:

$$\vec{q} \equiv \vec{k}_s - \vec{k}_i, \quad (\text{II.10})$$

and its magnitude is:

$$q \equiv |\vec{q}| = \frac{4\pi}{\lambda} \sin \Theta, \quad (\text{II.11})$$

which has the unit of nm^{-1} and is referred to as the reciprocal space. Combined with Bragg's law:

$$2d \sin \Theta = n \lambda, \quad (\text{II.12})$$

one obtains:

$$q = \frac{2\pi}{d}, \quad (\text{II.13})$$

which links the reciprocal space to the real space d .

Each electron that is illuminated by the X-ray beam has the same contribution to the observed scattering, which is described by the scattering cross section σ . The ratio between the photons that are scattered into any unit solid angle (Ω) per unit time Φ_s and the total number of photons per unit time Φ_0 gives the differential scattering cross section:

$$\frac{d\sigma}{d\Omega}(q) = \frac{\Phi_s}{\Phi_0}. \quad (\text{II.14})$$

The differential scattered cross section per unit volume, defined as:

$$\frac{d\Sigma}{d\Omega}(q) = \frac{1}{V} \frac{d\sigma}{d\Omega}(q) \quad (\text{II.15})$$

gives the scattering on the absolute scale. To obtain it from the measured intensities, the detector counts $I(q, t)$ need to be corrected for the acquisition time t , the subtended solid angle $\Delta\Omega$, the sample thickness d_s , the transmission T and the incident intensity I_0

$$I(q) = \frac{d\Sigma}{d\Omega}(q) = \frac{1}{d_s T I_0 \Delta\Omega t} I(q, t). \quad (\text{II.16})$$

Depending on the detector, different other corrections have to be applied, e.g. dark current correction for the base read out of the detector.^[118] Furthermore, it is necessary to subtract

background scattering from the sample environment (e.g. solvent, the windows of the sample holder, air) to obtain the scattering pattern of the sample alone.

Calibration standards like silver behenate^[119] (peaks at $q = 2\pi n/5.84 \text{ nm}^{-1}$) or tetracanol^[120] (peaks at $q = 2\pi n/1.58 \text{ nm}^{-1}$) can be used to calibrate the sample-detector distance. With a known sample-detector distance and the incident position of the direct beam, the 2D detector image can be azimuthally integrated to yield the scattering pattern as $I(q)$ versus q . The intensity can be calibrated when the intensity of the incident beam can be measured with the same efficiency as the scattered beam or by secondary standards like water^[121,122] ($I(q)=1.6 \cdot 10^{-2} \text{ cm}^{-1}$ for $q < 4 \text{ nm}^{-1}$), Lupolen^[123] ($I(q)=6 \text{ cm}^{-1}$ for $q = 0.35 \text{ nm}^{-1}$) or calibrated glassy carbon^[124,125].

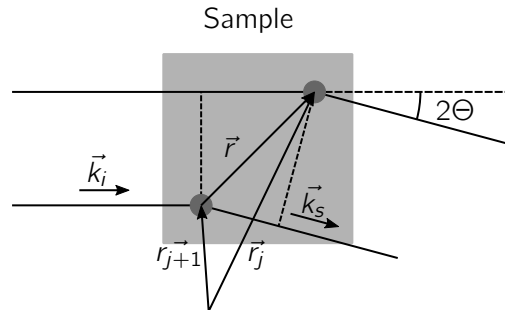


Figure II.8: Scattering of two points. Their relative positions are characterized by \vec{r} .

The interference of the scattered waves of two points can be described in terms of its phase difference $\Delta\phi$. With the relative position of the scatterers $\vec{r} = \vec{r}_j - \vec{r}_{j+1}$ (Figure II.8), the phase difference of the scattered waves is:

$$\Delta\Phi = \vec{r}(\vec{k}_i - \vec{k}_s) = -\vec{r} \vec{q}. \quad (\text{II.17})$$

Since X-rays are scattered by electrons, a pair of scattering objects can be described in terms of its scattering length density $\rho(\vec{r})$:

$$\rho(\vec{r}) = \sum \rho_i(\vec{r}) b_i, \quad (\text{II.18})$$

where $\rho(\vec{r})_i$ is the local density of scatterers of type i and the Thomson scattering length $b = e^2/(4\pi \epsilon_0 m c^2) = 2.82 \cdot 10^{-15} \text{ m}$.

Under the assumption that the scattering of an object is independent of the scattering by other scatterers (Born approximation), the local scattered amplitudes are added up:

$$A(q) = \int_V \rho_i(r) e^{-i q \vec{r}} d\vec{r}. \quad (\text{II.19})$$

The scattered amplitude is the Fourier transform of the scattering length density and the scattered intensity per unit volume V is:

$$I(q) = \frac{A(q) A^*(q)}{V}. \quad (\text{II.20})$$

With Equation II.19 the intensity can be written as:

$$I(q) = \frac{1}{V} \int_V \int_V \rho_i(\vec{r}) \rho_i(\vec{r}') e^{-i q(\vec{r}-\vec{r}')} d\vec{r} d\vec{r}'. \quad (\text{II.21})$$

With the correlation function:

$$\gamma(\vec{r}) = \frac{1}{V} \int_V \rho_i(\vec{r}') \rho_i(\vec{r} + \vec{r}') d\vec{r}', \quad (\text{II.22})$$

the scattered intensity can be expressed as:

$$I(q) = \int_V \gamma(\vec{r}) e^{-i q \vec{r}} d\vec{r}, \quad (\text{II.23})$$

highlighting the fact that the scattered intensity is the Fourier transform of the spatial correlation function.

To describe the observed scattering of monodisperse centrosymmetric particles, the scattering intensity can be written as:

$$I(q) = N V^2 \Delta\rho^2 P(q) S(q), \quad (\text{II.24})$$

where N is the number of particles per unit volume, V is the volume of the particle, $\Delta\rho^2$ is the relative scattering length density, $P(q)$ is the form factor and $S(q)$ the structure factor. $\Delta\rho^2$ describes the contrast between the scattering object and the background and determines the scattering power. The form factor $P(q)$ is the result of the interference of all the scattered photons from a single particle and is typical for its shape. If there are several particle shapes present, the observed scattering pattern will be an average of the form factors. The structure factor $S(q)$ describes the interparticle interactions. To observe the form factor of monodisperse particles the system has to be dilute, so that no particle-particle interactions are present ($S(q) \approx 1$). For a more concentrated system, the

interference pattern will contain information about neighboring particles, too. A decrease in intensity is generally indicative of a repulsive interaction, while an increase indicates attraction or particle aggregation. When such bumps develop into peaks it indicates highly ordered structures. The order of the peak positions enables to identify the symmetry of such (crystalline) structures.

2.3 Combining SAXS and Microfluidics

For the combination of SAXS and microfluidics, some implications arise from the equations above. First, the attenuation by the device material and the path length of the beam through this material should be small to obtain a strong signal from the sample. Second, the number of scattered photons depends on the scattering volume. The optimum sample thickness is $1/\mu$ and yields a transmission of $T \approx 0.37$. For water, this path length is rather large (1 mm at 8 keV) compared to the channel size in microfluidic devices. Therefore, the channel depth should be optimized to improve the signal. Third, the number of scattered photons depends on the number of incident photons. Thus, the photon flux of the beam should be rather high to compensate the non-optimum path length in microfluidic channels. A high photon flux is also particularly important for the combination of droplet microfluidics and SAXS, since the isolation of the droplet signal requires relatively short acquisition times. Overall, these requirements make it necessary to use a high intensity X-ray source, e.g. a synchrotron facility. Additionally, the beam cross section has to be small enough to collect the signal of the channel without any contribution from the device bulk material. Otherwise, parasitic scattering from the channel interface might be observed.

2.4 Isolating the Droplet Signal

In the following, some thoughts on how to isolate the scattering pattern of droplets from the carrier phase are discussed.

The microfluidic device generates a segmented flow of oil and water (Figure II.9). For a given water to oil flow rate ratio the length of the water segment l_w is constant. During the experiment the water droplets pass the X-ray beam, which is characterized by its length l_b along the channel axis. To isolate the signal of the droplets:

$$l_w > l_b \tag{II.25}$$

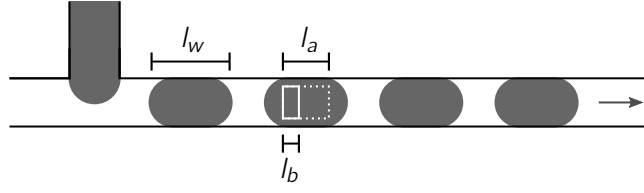


Figure II.9: Droplet generation in a microfluidic device in the path of a rectangular X-ray beam. The droplet length l_w , beam length l_b and acquisition length l_a are indicated. The beam is shown as solid white rectangle, while the broken white rectangle shows the part of the droplet that already moved through the beam during the acquisition time.

has to be fulfilled, otherwise l_b will never be completely filled by the water segment. During the acquisition time t_a , the droplets move with a velocity v through the channel. Thus, the acquisition time corresponds to an acquisition length l_a over which the signal is collected:

$$l_a = t_a \cdot v. \quad (\text{II.26})$$

To optimize the acquisition time, the shorter dimension of an asymmetric beam should be perpendicular to the flow direction. The acquisition length for which only water signal is obtained is:

$$l_a \leq l_w - l_b. \quad (\text{II.27})$$

By choosing a l_a that is smaller than l_w , the probability to collect the signal of the droplet alone increases and several patterns of the same droplet can be acquired for $l_a \ll l_w$. The frequency of acquisition f_a can be equal to, lower or higher (Figure II.10) than the droplet frequency f_d . However, for $f_a = n \cdot f_d$ ($n \in \mathbb{N}$) the acquisition should be synchronized with the passing droplets. For this case, a phase shift between the acquisition and the passing droplets might result in a convolution of the droplet and carrier phase patterns or patterns that are only from the carrier phase. Figure II.10 depicts a typical experimental sequence. The frequency of acquisition is higher than the frequency of the droplets. The acquisition time ($\propto l_a$) is shorter than the droplet residence time in the beam ($\propto l_w$). As a result there are three different cases (Figure II.11): *i*) patterns from the oil phase alone, *ii*) mixed scattering patterns from oil and droplet, and *iii*) patterns of the droplets alone.

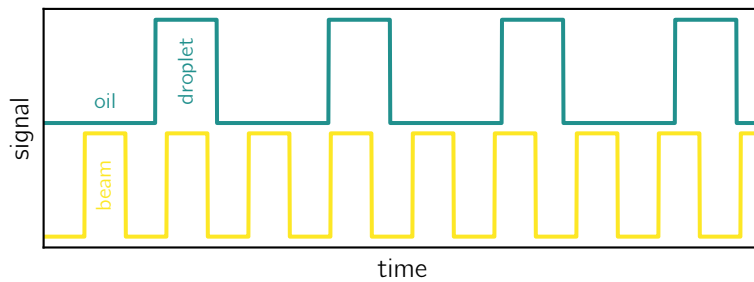


Figure II.10: Example for an acquisition frequency that is higher than the droplet frequency. The obtained scattering patterns are isolated droplet and oil phases and mixtures of both.

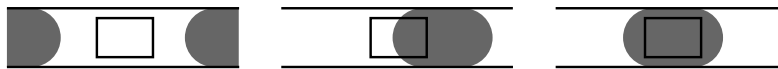


Figure II.11: The three potential acquisition possibilities in droplet microfluidics. The rectangle represents the probed area by the X-ray beam. **Left:** Only the scattering of the oil phase is acquired. **Center:** The scattering of oil and droplet is acquired. **Right:** Only the scattering of the droplet phase is acquired.

3 Materials and Methods

3.1 Microfluidic Device Fabrication

WBR/Si Masters

WBR/Si masters were prepared by laminating layers of dryfilm (50 μm thick WBR2050 and 100 μm thick WBR2100, Dupont) with a hot roll laminator onto a Si wafer (Sil'Tronix Silicon Technologies). After the lamination, microstructures were created by photolithography. To create a photomask the device structure was designed with the help of a computer-aided design program and printed on a flexible polyester film by a commercial service (JD Photo Data).

Before laminating the wafer it was degreased with acetone (99 %, Honeywell) and blow-dried with pressurized air. The first film layer was roughly cut to size and the protective polyethylene layer was removed by using sticky tape, before placing the wafer on a supporting metal plate (Cu, 1 mm thick). Then, the dryfilm was aligned to it with the unprotected

side facing the wafer. To reduce wrinkling of the film, the dryfilm was brought into contact with the metal support on the advancing side of the wafer before starting the roll laminator and the film was kept under tension during the lamination (Figure II.12). The lamination temperature was $85\text{ }^{\circ}\text{C}$ and the lamination speed was approximately $24\text{ mm}\cdot\text{s}^{-1}$. After lamination, the wafer was turned upside down and the excess dryfilm was removed. To apply a second layer of dryfilm, the protective polyester layer on top of the wafer-WBR stack was removed by using sticky tape and the procedure was repeated. The adhesion between the film and the substrate was improved by baking the piece over night at $60\text{ }^{\circ}\text{C}$ in an oven. After the item reached room temperature, the protective polyester layer was removed by using sticky tape, a photomask was aligned and brought into contact with the film. The assembly was then exposed to UV light for 20 s at $48.8\text{ mW}\cdot\text{cm}^{-1}$ (365 nm, UV-Kub 2, Kloeé). Before development, the excess of dryfilm was removed with a razor blade and it was baked at $100\text{ }^{\circ}\text{C}$ for 60 s on a hot plate (C-MAG HP 10, IKA). After cooling down, it was developed by applying a stream of 1% K_2CO_3 solution with a peristaltic pump (101U, Watson Marlow) until no undeveloped film was visible anymore. To finish the development it was washed with tap water and carefully blow dried with pressurized air.

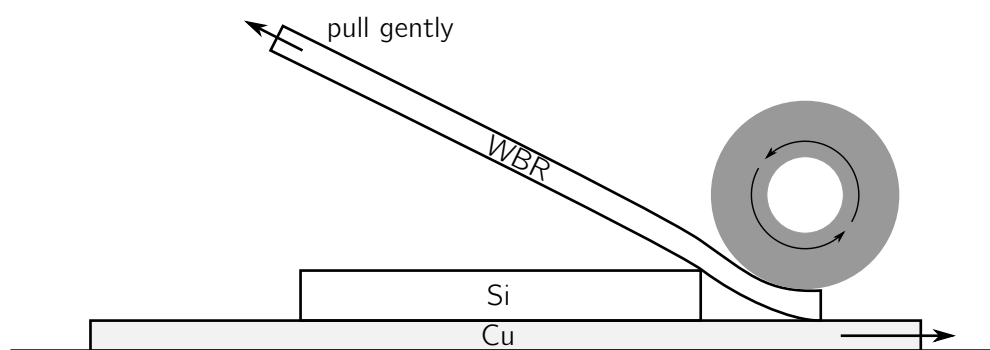


Figure II.12: Lamination of WBR dryfilm onto a Si wafer with a hot-roll laminator. By gently pulling the dryfilm during lamination it is kept under tension and the final laminate is wrinkle free.

PDMS Molds and Flat

PDMS negatives and flats were prepared by mixing PDMS elastomer base with its curing agent in a 10:1 ratio (Sylgard 184, DOW). After thorough mixing, the mixture was poured on the master and left under reduced pressure to remove air bubbles. The polymer was cured overnight in an oven at $60\text{ }^{\circ}\text{C}$. The PDMS pieces had to be relatively thin to fit into the UV-Kub 2 in the next preparation step, so only around 30 g of PDMS were used per

piece.

Off-stoichiometry Thiol-ene-epoxy Device

Off-stoichiometry thiol-ene-epoxy (OSTE+) pre-polymers (OSTEMER 322, Mercene Labs) were mixed in the indicated ratio (1.00:1.09) with a vortex mixer and shaken by hand until all haziness disappeared. Before use, it was left to rest until no air bubbles were visible anymore. OSTE+ was then poured on the PDMS mold and covered by another piece of PDMS, stabilized by a glass microscopy slide. By applying pressure, the excess OSTE+ was removed and recovered. To remove air bubbles that appear during the pouring step and are trapped on the design features, the PDMS molds were placed under reduced pressure beforehand and the filled mold stack was left alone until no bubbles were visible anymore. The assembly was then irradiated with approximately $24.4 \text{ mW} \cdot \text{cm}^{-1}$ for 120 s (365 nm, UV-Kub 2, Kloé). Afterwards, the PDMS mold was removed and the UV-cured OSTE+ carefully peeled off. Removing excess OSTE+ on the edges with sticky tape proved to facilitate the demolding. The flexible piece of OSTE+ was then placed on a flat sheet of polytetrafluoroethylene (PTFE) with the structured part facing down and cured in an oven at 90°C overnight. Access holes were machined into the fully cured piece with a bench-top drill. To align the drill with the device and to obtain reproducible hole distances a PMMA template was used. The cured and drilled piece was then rinsed with alcohol, blow dried with pressurized air and cleaned with sticky tape. Afterwards, it was aligned and bubble-free laminated onto a UV-cured flat piece of OSTE+ at room temperature. The assembled piece was then transferred onto a PTFE sheet and again cured at 90°C overnight in an oven. The process is sketched in Figure II.13.

Polyimide Composite Devices

To decrease the wall thickness of the device and the OSTE+ contribution to the wall, a commercial polyimide foil (Kapton, DuPont) with a thickness of $25 \mu\text{m}$ was used as wall material. The preparation protocol is similar to the pure OSTE+ device. The OSTE+ pre-polymer was mixed as described above and poured on the PDMS mold. It was then covered by a polyimide foil and a microscopy support slide, which were pressed against the bottom part to remove excess OSTE+ prepolymer. Then, the assembly was turned so that the polyimide foil was below the OSTE+ prepolymer and cured with UV light (365 nm , $24.4 \text{ mW} \cdot \text{cm}^{-1}$, 120 s, UV-Kub 2, Kloé). Note that if the polyimide foil is between the

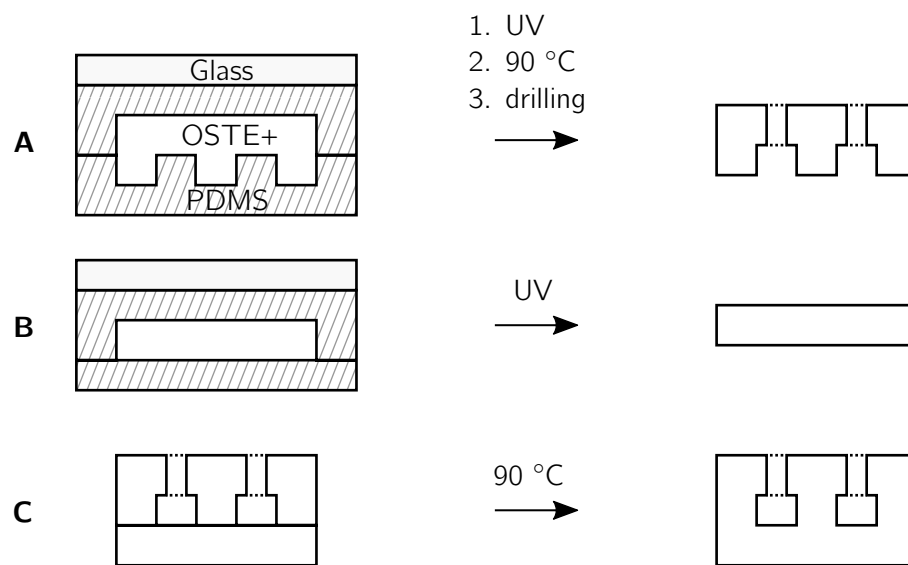


Figure II.13: OSTE+ device fabrication. **A:** PDMS molds are consecutively filled with OSTE+ pre-polymer, aligned, exposed to UV and demolded. The flexible OSTE+ is then cured at 90 °C and access holes are drilled into the material. **B:** PDMS molds are consecutively filled with OSTE+ pre-polymer, aligned, exposed to UV and demolded. **C:** The flexible bottom part is aligned to the rigid top part and cured at 90 °C.

prepolymer and the light source no curing occurs due to absorption by polyimide. Afterwards, the OSTE+/polyimide is demolded and access holes were punched with a biopsy puncher (Ted Pella). To obtain reproducible hole patterns, a template was printed on paper and aligned to the device before punching. The device was closed by bonding the OSTE+ part to a second polyimide foil at 90 °C.

Surface Modification of OSTE+

To increase the hydrophobic character of OSTE+ surface, it was hydrophobized by flushing the channels with a solution of a fluorosilane polymer (Novec 1720, 3M) before putting it on a hot plat at 110 °C for 30 min. The process was repeated for a total of three times.

Fabrication of Polydimethylsiloxane Devices

PDMS devices were directly obtained from WBr/Si by mixing PDMS elastomer base with its curing agent in a 10:1 ratio (Sylgard 184, DOW), pouring the prepolymer onto the master and degassing it under reduced pressure. The polymer was cured in an oven over night at 60 °C. To increase the hydrophobic character of the PDMS surface it was hydrophobized with the same procedure as the one described for OSTE+.

3.2 Characterization of OSTE+ Microfluidic Devices

Surface Homogeneity and Channel Height

The channel height of the WBR master and the OSTE+ device, and the surface of the OSTE+ were probed by a white light interferometry microscope (smartWLI basic, Gesellschaft für Bild- und Signalverarbeitung (GBS) mbH) and analyzed by commercial software (MountainsMap, Digital Surf).

Device Thickness

The total thickness of one finished and one half-finished device was measured at different locations with a digital micrometer (293-521 N, Mitutoyo, precision of 1 µm) with a probing head diameter of 6.35 mm².

3.3 Microfluidic experiments

Materials

Oils. Several oils were tested as inert carrier phase. FC-40, FC-70, FC-3283, perfluorodecaline, 3-octanol, hexadecane and light mineral oil were acquired from Sigma-Aldrich.

Surfactants. To stabilize the droplets and to improve the wetting behavior of the oil phase several surfactants were tested. Span 80 (sorbitan monooleate) was acquired from CRODA and used in combination with hexadecane and light mineral oil. ABIL EM 90 was acquired from CRODA and used in combination with light mineral oil.

Reactant Solutions. Cerium nitrate ($\text{Ce}(\text{NO}_3)_3$, Sigma-Aldrich) and oxalic acid ($\text{H}_2\text{C}_2\text{O}_4$, Sigma-Aldrich) solutions of various concentrations were prepared with high purity water ($18.2 \text{ M}\Omega \cdot \text{cm}$) and a binary mixture as solvent. The binary solvent consisted of high purity water and 1,2-propanediol (Sigma-Aldrich) in a 25:75 ratio by weight.

Gold Nanoparticles. Gold nanoparticles were produced from a reverse Turkevich method following the protocol described by Siveraman et al.^[126] 250 μL of aqueous 25.4 mM HAuCl_4 solution is added rapidly to 24.75 mL of 5.2 mM boiling citrate solution under vigorous stirring. Boiling is stopped after 250 s and the solution is let without stirring for 12 h before being used. The nanoparticles are characterized by SAXS and TEM (see Appendix A) and have a diameter of $9.4 \pm 1.0 \text{ nm}$.

Fluid control

The microfluidic device was connected to computer controlled (neMESYS UserInterface, Cetoni) syringe pumps (neMESYS system, Cetoni) via a customized device holder (ICH-01K, IMT). Polyether ether ketone (PEEK) tubing was connected to gas tight syringes (SGE Analytical Science) by Luer adapters on one side and to the device holder by hollow screws with a PTFE gasket on their tip on the other side (Figure II.14). To use the device holder in the X-ray scattering experiments an adapter was machined from stainless steel (Figure B.1).



Figure II.14: Left: IMT device holder with tube connector. Right: IMT tube connector with PTFE gasket.

Preliminary Experiments on Droplet Formation and Reactant Mixing

Observations were made through a microscope (IMT-2, Olympus) with a mounted and computer controlled (Phantom Camera Control 2.2, Ametek) high speed camera (Phantom v7.3, Vision Research). Droplets were generated by uniting three streams of water and feeding it into a T-junction with an immiscible phase. The flow rates, the wetting behaviour, and the droplet pinch-off were optimized. To observe reactivity in the formed droplets, two of the three water streams were substituted by a stream of cerium nitrate and oxalic acid solution (Figure II.15). The two channels were separated by a stream of solvent in the center channel to avoid reactivity before the mixing part of the device. The droplets were then allowed to mix in a passive serpentine mixer and to age in a 24 cm long channel before being collected.

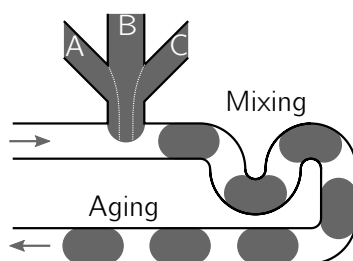


Figure II.15: Schematic representation of the microfluidic device. A T-junction into which an oil phase and three aqueous phases are fed. The generated droplets mix in a passive serpentine mixer and age in a long channel. By varying the content and flow rate of the channels A, B and C, the droplet content is varied.

Estimation of the Mixing Time

Observations were made through a microscope (CKX41, Olympus) with a mounted and computer controlled (Micromanager, Open Imaging) camera (pco.edge 5.5, PCO). To estimate the mixing time an aqueous solution of a fluorescent dye (fluorescein, Sigma-Aldrich) was fed to the device and mixed with water in water-in-oil droplets. Fluorescence was initiated by a UV-source (U-RFLT50, Olympus) and the traveled distance to reach a homogeneous fluorescence in the droplet was observed.

3.4 X-ray Scattering Experiments

X-ray scattering experiments were performed *i)* at the SWAXS Lab Saclay on a Xeuss 2.0 laboratory beamline (Xenoxs) at a photon energy of 8.04 keV with a Pilatus3 R 1M detector (Dectris) at a sample detector distance of 42.4 cm and *ii)* at the small and wide angle X-ray scattering (SWING) beamline of the SOLEIL synchrotron facility in France, at photon energies of 12.00 and 16.00 keV with a Eiger 4M detector (Dectris) at a sample detector distance of 52.2 and 616.5 cm. Sample detector distances were verified using tetradecanol as calibrant.

X-ray Transmittance of OSTE+ and its Linear Attenuation Coefficient

Calculations were made with the help of xraylib,^[127] values for the X-ray mass attenuation coefficient are listed in different databases like the NIST Standard Reference Database 66.^[117]

Standard Data Treatment

Each raw scattering pattern was masked and azimuthally averaged to yield the scattering curve $I(q)$. The intensity was normalized by the solid angle, the acquisition time and the transmitted flux. After background subtraction, the intensity was normalized by the sample thickness and brought to absolute scale by calibration measurements of Lupolen or water.

Material Aging

In order to investigate on the impact of X-rays, OSTE+ was repeatedly irradiated at 16.00 keV with a $50 \mu\text{m} \times 400 \mu\text{m}$ (vertically \times horizontally) beam for 500 ms and a gap

time of 250 ms between each individual acquisition, for a total irradiation time of 500 s. The same procedure was applied to OSTE+ that was additionally cured at 150 °C for seven days before X-ray irradiation.

Data Treatment for In-situ X-ray Scattering Experiments

A custom Python 3 code was developed and used for data treatment. The `nexusformat`[†] package was used to read data from the Nexus data files, obtained from the SWING beam line. Each frame was radially averaged with the help of the `pyFAI`^{[128]‡} package and normalized by the solid angle, the acquisition time and the transmitted flux. For static samples, several frames were averaged to give a single 2D data file. Data from droplet experiments was analyzed regarding the variation in scattering. Oil and droplet phase have different scattering curves and intensities. A segment of the scattering vector was defined in which the intensity of each curve was averaged. The data was then categorized based on threshold values, rejecting a certain percentile of the data and assigning the remaining data as droplet or oil phase based on their value. Data where the signal of oil and droplet is mixed has an intermediate value and was rejected. After sorting the data, each phase was separately averaged to yield one data file. If possible, the background scattering was subtracted and the data was normalized by the channel thickness and a normalization factor to obtain the absolute scattering intensity. The full code is provided in Appendix C.

4 Results and Discussion

4.1 Microfluidic Device Fabrication

The process to develop a protocol for the preparation of OSTE+ devices with a suitable thickness in a reproducible way was rather time consuming and challenging. In the following, some of the key choices in the described protocol are discussed.

Si Master

The first masters were prepared with SU-8 (MicroChem) as photoresist. After adapting the initial device design to the requirements of the experiment, it became apparent that SU-8

[†]<https://github.com/nexpy/nexusformat>

[‡]<https://pyfai.readthedocs.io>

has some drawbacks, i.e. for the preparation of thick layers. In contrast to SU-8, WBR dry film can be stacked and gives access to thick layers of photo resist in a reproducible fashion. However, WBR has some drawbacks, e.g. its relatively poor adhesion properties. To improve the adhesion to the substrate it was useful to extend the post-lamination bake overnight at 60 °C instead of 20 min only, as suggested in the data sheet. A finished master is depicted in Figure II.16.

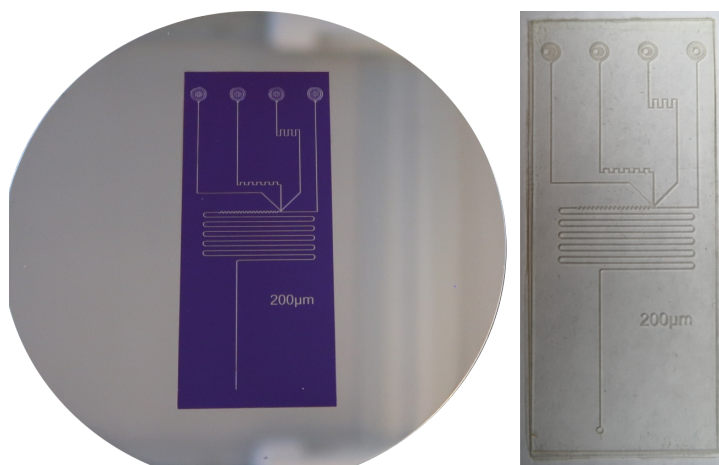


Figure II.16: Left: WBR/Si Master. Right: Finished OSTE+ device.

PDMS Molds

The use of PDMS molds instead of directly using a Si master has several benefits. First, it is less time consuming to replace a PDMS mold than a Si master and PDMS molds can easily be prepared from the masters. Second, PDMS is transparent to visible and UV light, which allows spotting potentially trapped bubbles and enables the OSTE+ prepolymer curing by UV light. Third, the porosity of PDMS facilitates the elimination of trapped air bubbles after filling in the OSTE+ pre-polymer by degassing the PDMS mold before use. Finally, PDMS is flexible and simplifies the demolding after the UV curing step. However, the elasticity of PDMS is a problem during the stacking step of the molds to give a fixed height (Figure II.13). Without support, the PDMS roof tends to collapse onto the chip design under pressure. This problem can be addressed by supporting the PDMS mold with a glass slide. For ease of use, the glass slide can be permanently bonded to the PDMS piece by plasma treatment.

OSTE+ Device Preparation

There are several considerations in the presented protocol that deserve to be discussed.

- i)* Using two molds for the preparation of the device parts, allows to prepare devices with different designs and wall thickness simply by switching the bottom or top mold. In a one-mold approach, each design would have a fixed wall thickness and would require the preparation of a new master in a two-step photolithography process. The first step would define the wall thickness, while the second step creates the design. Additionally, a flat piece of OSTE+ needs to be prepared to close the device. Thus, the mold that defines the wall thickness can be used for both pieces.
- ii)* Instead of removing excess OSTE+ prepolymer after aligning and pressing the molds together, the molds could be aligned beforehand and then be used for injection molding^[78] or they could be filled by capillary forces.^[129] Both alternative approaches were tested and should be viable after adaptation, but were not used further.
- iii)* After filling the molds with liquid pre-polymer, a UV curing step follows to polymerize the material. The irradiation time was rather long and the lamp was only operated at half of its maximum power to obtain a complete reticulation without generating too much heat, which would trigger the second curing step.
- iv)* The final wall thickness of 200 μm that is imposed by the PDMS mold. For thinner walls, the structured part teared easily during demolding after the first curing step. One solution to reduce this thickness is the use of a thin X-ray compatible wall material like polyimide foil or other commercial foils. Another would be to pre-fabricate thin, fully cured sheets of OSTE+ as support material and to use them instead of the second mold.
- v)* OSTE+ sticks to many materials thanks to the epoxy groups. These groups are activated during the heating step and some sort of support is necessary to hold the OSTE+ items. Although OSTE+ should not adhere to aluminum, the thin devices could not be removed without damaging them. Thus, a sheet of PTFE was used as support material.
- vi)* The first half of the chip was fully cured before the device was assembled, since drilling into fully cured OSTE+ gave cleaner holes than using biopsy punchers on only UV cured pieces. Punching the holes also creates sticky debris, which is tricky to remove afterwards. The debris from machining the fully cured workpiece is not sticky and can be easily removed by pressurized air and sticky tape. A drawback of fully curing

OSTE+ before assembling the final device is that it limits the choices for surface modification. OSTE+ that is only cured by UV can easily be surface modified to show more hydrophobic or more hydrophilic behavior.^[95] However, modification of the whole piece, instead of the channels only, prevents bonding in the heat-curing step due to the loss of the respective functional groups. The bonding capacity can be retained by adding allyl glycidyl ether to the modification cocktail. The downside of using allyl glycidyl ether is its acute and reproductive toxicity, and its mutagenic and carcinogenic properties. Due to these safety concerns in combination with local conditions and limitations in the laboratory, the surface modification was carried out after the device was assembled and fully cured.

- vii) The alignment and lamination of the two OSTE+ parts are the probably most delicate steps in the preparation of the device. To achieve a bubble-free assembly the two parts can be laminated either by a roll laminator or by applying the necessary pressure by hand. Another, untested method might be the use of a bench-top press. Whatever the method, it is important that there are no remaining trapped particles or air bubbles. Both might result in an unusable device after the final bonding step.

Polyimide Composite Devices

A polyimide/OSTE+ composite device is depicted in Figure II.17. In contrast to the devices that are made of OSTE+ only, the structured part of the polyimide composite devices cannot be cured before finishing the device, otherwise the OSTE+ layer would lose its binding capacity with the second polyimide layer. Since the structured part is not fully cured, the access holes cannot be drilled, but have to be punched. However, this is less of a problem, since the layer thickness of OSTE+ is lower and almost no debris is formed while using biopsy punchers to create the holes. A similar manufacturing approach has been recently reported in literature.^[25]

4.2 Characterization of OSTE+ Microfluidic Devices

Surface Homogeneity and Channel Dimensions

White light interferometry microscopy was used to probe the surface roughness of the finished device and the channel height of the master and finished device. The channel width in a finished device was probed by bright-field microscopy. As can be seen in Figure II.18, the



Figure II.17: A finished polyimide/OSTE+ composite device.

surface structure is rather smooth and only varies within $5\ \mu\text{m}$ locally. The WBR/Si master and the final OSTE+ piece achieve a channel height of $150\ \mu\text{m}$ (Figure II.19). The channel width deviates from the intended design by $10\ \mu\text{m}$ and measures $190\ \mu\text{m}$ (Figure II.19). Overall, the quality of reproduction is high, and the height control with WBR dry film is facile and excellent.

Device Thickness

By design the device thickness should be $550\ \mu\text{m}$ due to the $150\ \mu\text{m}$ channel height and two times $200\ \mu\text{m}$ wall thickness to close the structure. Measurements of typical devices with a digital micrometer (Table II.2) show that the thickness of both a closed device and an open device, which was not closed yet, is below this theoretical value. The results in Table II.2 are representative of the produced chips, but vary from chip to chip individually. Pressing the molds together to remove the pre-polymer excess seems to compress the molds more than intended, resulting in thinner walls. The data shows that the thickness in position 2 and position 5 is smaller than at the other positions (Figure II.20). It seems like the used glass slide is not able to entirely prevent the collapse of the elastic PDMS molds under pressure. Thinner walls are better for in-situ SAXS measurements, since thinner walls mean less background scattering of OSTE+. However, the thickness variation along the channels will result in a different SAXS background for each position. It is therefore absolutely necessary to record the background signal at each probed position. For the polyimide composite

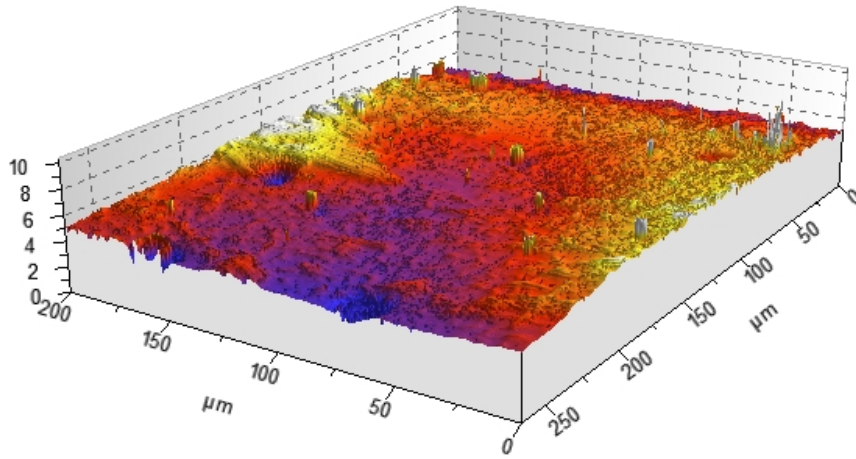


Figure II.18: Surface roughness profile of the flat side of a OSTE+ device in μm .

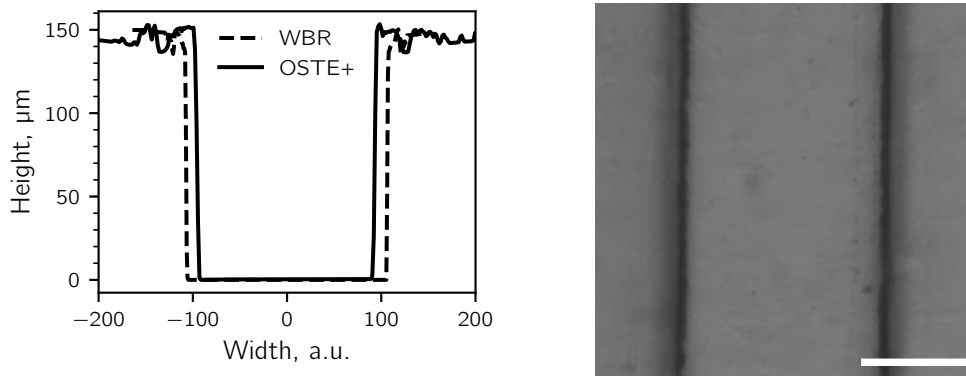


Figure II.19: Left: Height profile for the channels on the WBR/Si master and in the finished device. **Right:** Microscopy image for a channel in an open OSTE+ Device. The channel has a width of 190 μm . Scale bar is 100 μm .

chips, the measurements show that the chip thickness is higher than the expected value. By design the devices should have a thickness of 200 μm coming from the channel height of 150 μm and two layers of polyimide with 25 μm each. Thus, the additional thickness has to be OSTE+, which will add an additional signal to the SAXS background of the polyimide composite chip.

Summary

The presented approach to prepare OSTE+ based microfluidic devices is similar to protocols from literature.^[25,79,130] The main difference is the focus on obtaining thin OSTE+ walls to reduce the background signal for in-situ SAXS. For the all-OSTE+ devices a total wall thickness below 400 μm has been achieved. To reduce the device thickness even more, polyimide-OSTE+ composite devices were prepared similar to an approach in literature.^[25] The reproduction and surface quality of OSTE+ were excellent and the yield, in terms of finished devices that are without defects, is rather high ($\approx 80\%$). Achieving thinner OSTE+ walls would be desirable, but will need more development effort.

4.3 Results from Bench-top Experiments

In the following paragraphs the major observations and results regarding the preliminary experiments to set up the in-situ X-ray scattering experiments are described.

Interchangeability of PDMS and OSTE+ Devices

Although the developed protocol allows a reasonably quick preparation of OSTE+ devices, it is still easier to prepare PDMS devices. This is especially important for applications where channels might be blocked regularly, like the exploration of precipitation reactions. Since the geometry and wetting properties of both device types were practically the same, most of the initial tests were made in PDMS devices and were only transferred to OSTE+ devices to optimize the chemical conditions for SAXS experiments when a reasonable stability was obtained. This was possible since both device types had the same geometry and the same surface properties after the surface treatment. The use of surfactants made the surface treatment redundant, although PDMS is slightly more hydrophobic compared to OSTE+. Consequently, the transition from PDMS to OSTE+ had no significant influence on the droplet generation. The main differences between both materials is their rigidity and their

Table II.2: Digital micrometer measurements for the thickness of a closed device and a device before closing. Probed positions can be seen in Figure II.20

	Closed device	Open device
Position	Thickness, μm	
1	488	332
2	424	313
3	492	316
4	475	337
5	436	311
6	486	320

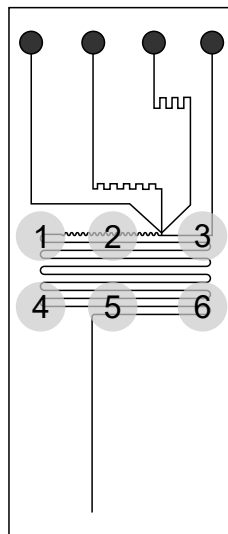


Figure II.20: Regions probed by a digital micrometer. Grey circles indicate the diameter of the probe head. Sketch is to scale. Results are listed in Table II.2

different solvent resistance, which allows to use alkanes without swelling in OSTE+.

Usable Carrier Phases and Need for Surfactants

To be a usable carrier phase the compound needs to be immiscible with the aqueous phase, it has to wet the channel walls and it has to be compatible with the channel material. Furthermore, its physical-chemical properties have to allow the formation of droplets at the considered flow rates and it should not interact with the droplet content.

Aqueous System. Without the addition of surfactants or surface modification of the channel walls, only 3-octanol was successfully tested to form droplets. After surface modification, it was possible to generate water droplets with 3-octanol, hexadecane and FC-40. When the experiments transitioned from pure water droplets to the exploration of the cerium oxalate precipitation, crystals appeared after some time outside of the droplets and blocked the channel due to their subsequent growth. Since no crystals were observable inside the droplets, it is highly probable that the crystals originated from nuclei that were formed inside the droplets and passed the water-oil interface or at their interface. After passing into the oil phase, they deposited on the channel wall and grew from passing droplets that provided them with fresh reagents. Consequently, surfactants were added to the carrier phase to block the droplet interface and to prevent any nuclei to pass it. Solutions of hexadecane and light mineral oil with at least 1 % (w/w) of Span 80 were used. With the added surfactants, the droplets were stabilized and no crystal formation outside the droplets was observed. The droplets were also stable enough to be collected and observed after leaving the device.

Binary Solvent System. Using structured solvents potentially influences the resulting morphology or kinetics of a reaction.^[27] A binary solvent that was reported to influence the final particle shape is investigated.^[23,26,27] Due to its high content in 1,2-propanediol it has different wetting properties and is more viscous than pure water. Hexadecane is not usable as a carrier phase, since it seems to dissolve into the binary solvent. However, light mineral oil does not and is able to form droplets at the inlet after adding 1 % (w/w) of Span 80.

Flow Rates

The experimental setup can sustain flow rates of at least $100 \mu\text{L} \cdot \text{min}^{-1}$. However, lower flow rates of $15 \mu\text{L} \cdot \text{min}^{-1}$ ($\approx 9 \text{ mm} \cdot \text{s}^{-1}$) and below make more sense to obtain sufficiently long acquisition times for the SAXS experiment. The flow rate ratio between the carrier phase and the droplet phase to obtain suitably sized droplets is mainly dictated by the physico-chemical properties of the liquids. Another important flow rate ratio is the one between the buffer phase and the two reactant phases, which are united to form the droplets. If the ratio of buffer is too low, the reactants can diffuse through the buffer and react before they are encapsulated in the droplet. For a system of aqueous solutions of $\text{Ce}(\text{NO}_3)_3$ and $\text{H}_2\text{C}_2\text{O}_4$ and water as buffer, a 1:1:8 ratio is necessary to prevent the formation of a precipitate at the inlet (Figure II.21). This precipitate grows in the inlet and eventually detaches from the channel, resulting in a blocked device. For a buffer with a different diffusion coefficient, the ratio can be lower.

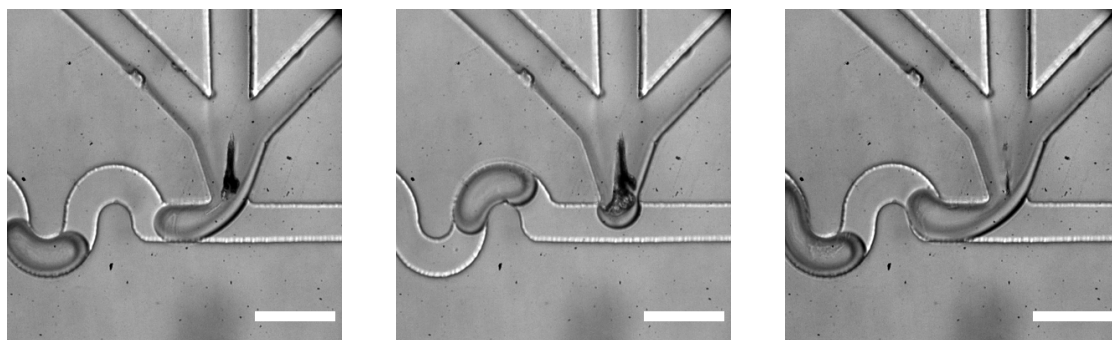


Figure II.21: Left to right: Growth of precipitate in the inlet and subsequent break-off for too low center channel flow rates. Scale bars are $200 \mu\text{m}$.

Mixing Time

To obtain an estimate of the mixing time within a droplet, droplets containing a fluorescent dye were generated and the path length to homogenize was observed. From the path length and the flow rate, it is possible to calculate the time until homogenization was reached. The droplets in Figure II.22 need 7 to 8 turns at a flow rate of $15 \mu\text{L} \cdot \text{min}^{-1}$ to reach a homogeneous fluorescence, which corresponds to a velocity of $8772 \mu\text{m} \cdot \text{s}^{-1}$ in the $150 \mu\text{m} \times 190 \mu\text{m}$ (height \times width) channel. The traveled path corresponds to approximately $4000 \mu\text{m}$ and a travel time of 450 ms . Calculating the mixing time for a droplet length of $480 \mu\text{m}$ with Equation II.5 yields 433 ms for fluorescein and 435 ms for $\text{Ce}(\text{III})$ with

diffusion coefficients of $6.4 \cdot 10^{-10} \text{ m}^2 \cdot \text{s}^{-1}$ and $6.2 \cdot 10^{-10} \text{ m}^2 \cdot \text{s}^{-1}$, respectively.^[131,132] The experimentally approximated data and the calculated data agree well. However, the mixing time is far away from the fast literature values of $\approx 500 \mu\text{s}$, which was achieved for droplets in a channel with a cross section of $10 \mu\text{m}$ and a velocity of $400 \text{ mm} \cdot \text{s}^{-1}$.^[81] At such velocities and droplet sizes, the isolation of droplet signal would require microsecond acquisition times and an appropriately high photon flux. This is not feasible for the in-situ SAXS study.

To improve the mixing time for future designs, the droplet length to channel width ratio should be reduced^[81,133,134] or a different channel cross section could be used for the mixing and observation part to decrease the droplet velocity after mixing. Another option might be to use fast mixing along the channel axis by coalescing two reactant containing droplets, as demonstrated by Vitry et al.^[28] To improve the probability of coalescence an alternating current electric field might be used.^[135] However, the achieved mixing time of $\approx 450 \text{ ms}$ is well suited for the planned experiments.

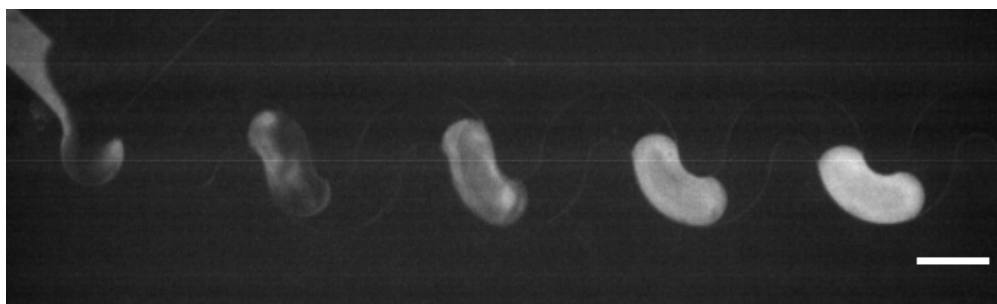


Figure II.22: A fluorescent colorant is mixed with water inside the droplets at a total flow rate of $15 \mu\text{L} \cdot \text{min}^{-1}$. The fourth droplet shows homogeneous fluorescence. Scale bar is $300 \mu\text{m}$.

Concentration Range for the Cerium Oxalate Precipitation System

Due to the dilution by the buffer phase, the maximum achievable concentration inside the droplets is one tenth of the feeding solution concentration. Thus, the upper concentration limit is naturally determined by the solubility limit which is around 1 M for $\text{H}_2\text{C}_2\text{O}_4$ and 4 M for $\text{Ce}(\text{NO}_3)_3$ at ambient temperature.^[136,137] The lower limit is given by the solubility constant. Is the reactant concentration below this limit, all reactants stay solubilized and no precipitation occurs. However, for $\text{Ce}_2(\text{C}_2\text{O}_4)_3$ the solubility product is rather low ($p_S = 1.84 \cdot 10^{-28}$)^[138] and the detection limit of the SAXS experiment will dictate the

lower concentration limit. Stoichiometric reactant ratios were chosen for the experiments to simplify the system. Note that off-stoichiometry reactant ratios were shown to yield different crystal habits, and could also be easily studied in the device.^[23] For feeding solutions with a concentration of 0.010 and 0.10 M in $\text{Ce}(\text{NO}_3)_3$ and 0.015 and 0.15 M in $\text{H}_2\text{C}_2\text{O}_4$ a suitable reactivity was achieved.

In the following, the used flow rates for the different phases are $10 \mu\text{L} \cdot \text{min}^{-1}$ for the oil phase, $4 \mu\text{L} \cdot \text{min}^{-1}$ for water in the central channel and $0.5 \mu\text{L} \cdot \text{min}^{-1}$ each, for solutions of $\text{Ce}(\text{NO}_3)_3$ and $\text{H}_2\text{C}_2\text{O}_4$ in the left and right channel leading to the T-junction.

At feeding concentrations of 0.010 M $\text{Ce}(\text{NO}_3)_3$ and 0.015 M $\text{H}_2\text{C}_2\text{O}_4$ a concentration of 0.0010 M $\text{Ce}(\text{NO}_3)_3$ and 0.0015 M $\text{H}_2\text{C}_2\text{O}_4$ is achieved in the droplets and no precipitation is observable within the device. However, growth of microscopic star shaped crystals can be observed under the microscope inside the droplets shortly after they left the device (Figure II.23).

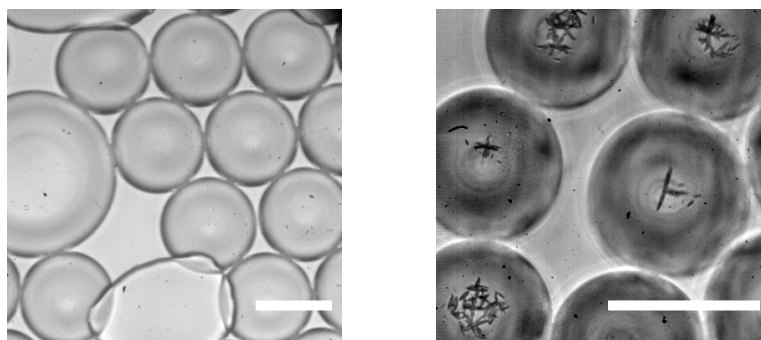


Figure II.23: Droplets with a concentration of 0.0010 M $\text{Ce}(\text{NO}_3)_3$ and 0.0015 M $\text{H}_2\text{C}_2\text{O}_4$. **Left:** Droplets right after leaving the device. **Right:** Crystals have grown inside the droplets after some time. Scale bars are 200 μm .

For the feeding concentrations of 0.10 M $\text{Ce}(\text{NO}_3)_3$ and 0.15 M $\text{H}_2\text{C}_2\text{O}_4$ the droplets have a concentration of 0.010 M $\text{Ce}(\text{NO}_3)_3$ and 0.015 M $\text{H}_2\text{C}_2\text{O}_4$ and the observations are different. Directly after the droplet generation, translucent aggregates with a different refractive index can be observed inside the droplets. Those aggregates mature to dense, dark particles that remain inside the droplets (Figure II.24). The aggregates probably form during the droplet formation and the mixing time is too slow to isolate mixing from nucleation and growth.

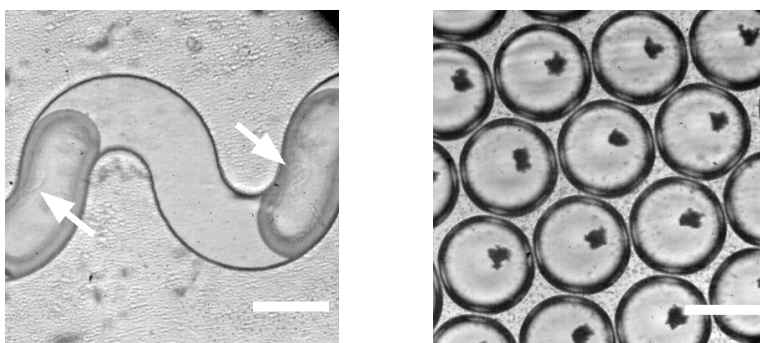


Figure II.24: Droplets with a concentration of 0.010 M $\text{Ce}(\text{NO}_3)_3$ and 0.015 M $\text{H}_2\text{C}_2\text{O}_4$. **Left:** Droplets right after droplet generation. Arrows point at translucent material inside the droplet. **Right:** Droplets right after leaving the device showing aggregated dark spots. Scale bars are 200 μm .

Summary

The prepared OSTE+ devices exhibit practically the same geometrical features and properties as PDMS devices and can be used interchangeably for bench-top experiments. However, OSTE+ has a different solvent resistance and can be used with organic oil phases like hexadecane. Furthermore, the OSTE+ devices are thin and rigid, which makes them suitable for in-situ SAXS studies. The selected microfluidic design produces controllable and reproducible trains of droplets and potentially allows to follow a reaction kinetic.^[54] To study the precipitation of cerium oxalate in aqueous and binary solvent droplets, the use of surfactants is necessary to prevent the device from blocking. By carefully tuning the flow rates and concentrations, two different regimes of crystal formation inside the droplets have been identified. The observed difference is presumably linked to an increased reaction rate with higher concentrations that is faster than the mixing. However, the mixing time of approximately 450 ms is well suited for the intended use.

4.4 OSTE+ X-ray Characterization

X-ray Transmittance of OSTE+ and its Linear Attenuation Coefficient

In order to use OSTE+ as a wall material for in-situ X-ray investigations, it is important to know the transmittance at the photon energy of interest. Transmission values of samples with a thickness of 335, 511, 537 and 685 μm are plotted in Figure II.25. From Equations

II.7 and II.8 the linear attenuation coefficient μ can be calculated as:

$$\mu = \frac{-\ln T}{d_s} \quad (II.28)$$

from the measured transmission T and the sample thickness d_s . The calculation yields an experimental linear attenuation coefficient μ of 24.4 cm^{-1} at 8.04 keV for OSTE+.

The linear attenuation coefficient can also be calculated from the chemical composition and density of the material (see Equation II.6). Since, the composition and density of the used OSTE+ sample is not known, values from literature were taken for the calculation. Table II.3 summarizes the main components of OSTE+ and the relative ratios of a published composition. [93,139,140]

The calculation yields $\mu = 24.9 \text{ cm}^{-1}$ at 8.04 keV for a density of $\delta = 1.15 \text{ g} \cdot \text{cm}^{-3}$. [139] Since collected and calculated data agree well, μ is calculated for other relevant energies. The theoretical transmission at different energies is calculated from Equation II.8 as function of the thickness and plotted in Figure II.25.

Table II.3: Main components of an OSTE+ formulation from literature and its relative composition used to calculate the linear attenuation coefficient. [93,139,140]

Name	C	H	N	O	S	Ratio
Pentaerythritol tetrakis(2-mercaptoacetate)	13	20	0	8	4	1.5
1,3,5-Triallyl-1,3,5-triazine-2,4,6(1H,3H,5H)-trione	12	15	3	3	0	1
Bisphenol A diglycidyl ether	21	24	0	4	0	0.5
OSTE+ relative composition	42	57	3	17	6	

At 8.04 keV, the transmission decreases relatively quickly and falls below 30 % for a thickness above 500 μm . As expected, the transmission is higher at higher energies, and thus larger chip diameters could be used without losing too many photons by absorption. The linear attenuation coefficient of OSTE+ is compared to other relevant materials (Table II.4) in the fields of microfluidics and X-ray scattering in Figure II.26.

The linear attenuation coefficients can be grouped into three groups. Quartz is the first and has the highest values due to its high density and the presence of heavier elements compared to the organic polymers. The second group consists of OSTE+ and PDMS, which have higher coefficients due to the presence of S and Si, respectively. The last group is composed of the organic polymers, which contain only elements from the first and second

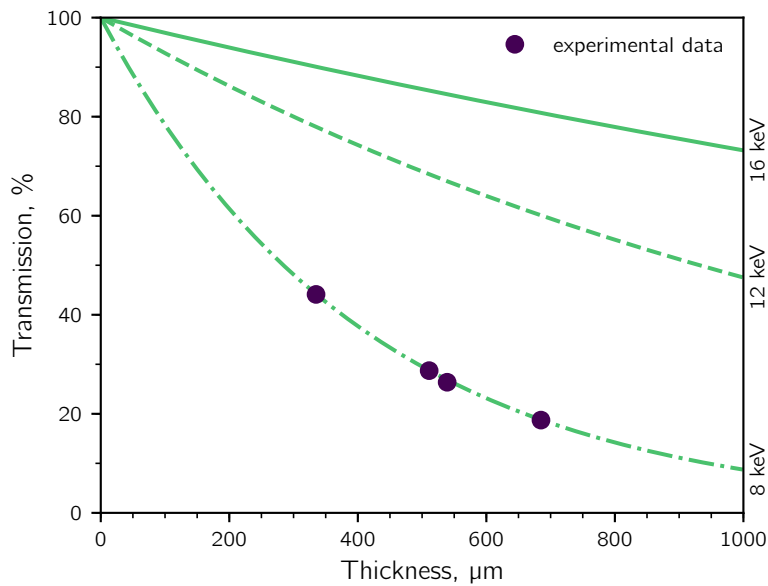


Figure II.25: Calculated transmission of OSTE+ at different sample thickness and different photon energies. Data was calculated with the help of xraylib.^[127]

Table II.4: Generic repeat unit formulas and densities used in the calculation of the linear attenuation coefficient for the different materials.

Name	Repeat unit formula	Approximate density, $\text{g} \cdot \text{cm}^{-3}$
Cyclic olefin copolymer (COC)	C_9H_{14}	1.02
Polydimethylsiloxane (PDMS)	$\text{C}_2\text{H}_6\text{OSi}$	0.965
Polyether ether ketone (PEEK)	$\text{C}_{19}\text{H}_{12}\text{O}_3$	1.32
Polyethylene terephthalate (PET)	$\text{C}_{10}\text{H}_8\text{O}_4$	1.38
Poly(methyl methacrylate) (PMMA)	$\text{C}_5\text{H}_8\text{O}_2$	1.18
Polyimide	$\text{C}_{22}\text{H}_{10}\text{N}_2\text{O}_5$	1.43
Quartz	SiO_2	2.65

period. Compared to polyimide, which is a commonly used material in X-ray scattering, OSTE+ will absorb more photons at any given thickness.

Scattering Pattern of OSTE+ and Polyimide

The absolute scattering intensity of polyimide and OSTE+ are plotted against the scattering vector q in Figure (II.27). Polyimide shows the typical bump between 0.3 to 2 nm^{-1} and the typical peaks at 4 and 8 nm^{-1} .

Compared to polyimide, OSTE+ has a similar scattering profile between 10 to 20 nm^{-1} but does not have any defined peaks. At lower values of q , the scattering intensity of OSTE+ is up to 180 times lower than from polyimide. Consequently, OSTE+ produces less background scattering for the same thickness when it is used as sample environment.

Aging of OSTE+ under Influence of X-rays and Heat

In order to check if the scattering pattern of OSTE+ alters under the influence of X-rays, OSTE+ of $511 \mu\text{m}$ thickness was irradiated for a total of 500 s by repeatedly acquiring the scattering images. The photon flux at SWING is typically $1 \cdot 10^{12} \text{ s}^{-1}$ for 16 keV. The same procedure was repeated for a piece of $538 \mu\text{m}$ thick OSTE+ that was additionally cured at 150°C . During the additional curing, the color changes to orange (Figure II.28). After the SAXS experiments, an orange stain is observed at the beam position for both chips (similar to Figure II.29), but vanishes after some weeks. Figure II.30 shows the SAXS patterns of the two OSTE+ samples. For OSTE+ that was cured under normal conditions the bump between 0.07 and 1 nm^{-1} increases while the slope below 0.07 nm^{-1} slightly decreases with increasing irradiation time. Above 1 nm^{-1} the scattering does not change significantly. For the sample that was cured at 150°C no changes with increasing irradiation time are observable. The similarities of the two patterns and the saturation curve for the sample that was cured at 90°C suggest that the observed changes are induced by heat and that the magnitude of change is influenced by the reached temperature. By choosing an appropriate curing temperature, structural changes in the polymer can be prevented during the experiment. Additionally, the stream of liquid in the microfluidic experiments is expected to cool down the material and may delay or prevent any changes in the pattern of OSTE+. Nonetheless, staining was observed during the in-situ microfluidic experiments (Figure II.29). The origin of staining is not very clear, since it was also observed for OSTE+ that was cured at 150°C , while no changes in the scattering pattern of this material were observed.

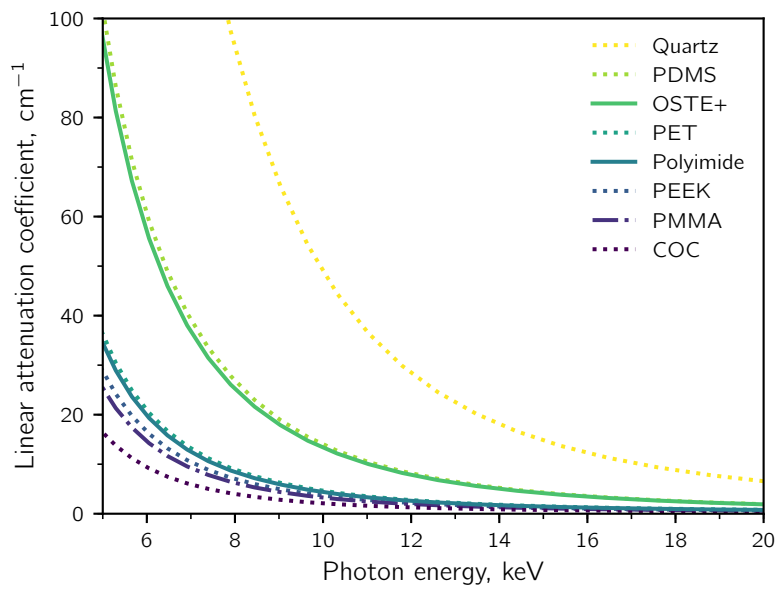


Figure II.26: Calculated linear attenuation coefficient μ of different polymers including polyimide and OSTE+ for photon energies from 5 to 20 keV. Data was calculated with the help of xraylib.^[127] Legend entries are in the same order as the curves are ordered from top to bottom.

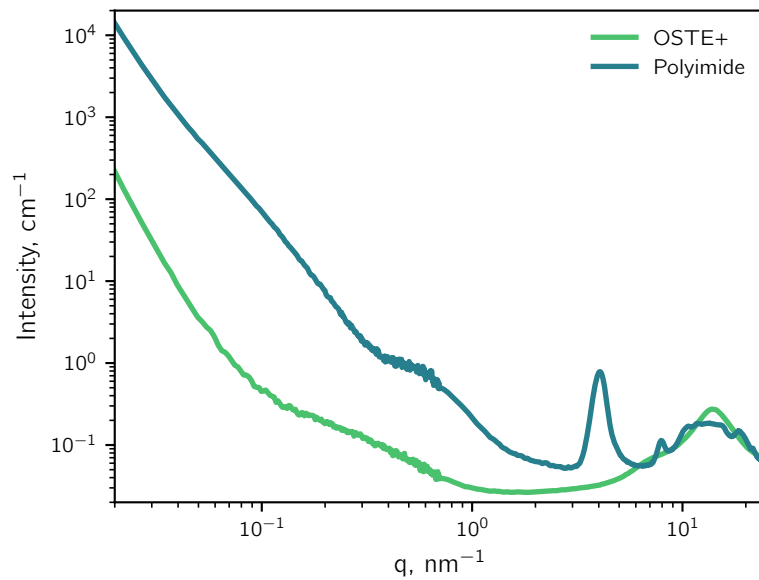


Figure II.27: Scattering patterns of OSTE+ and polyimide.

Hence, the stain might not have an influence on the scattering pattern.

Summary

OSTE+ has a rather high X-ray attenuation coefficient that is similar to PDMS and higher than polymers such as polyimide. The scattered intensity of OSTE+ is however up to 180 times lower than the one of polyimide, giving a lower background when used as window material. Compared to polyimide, OSTE+ is less resistant to irradiation. The scattering pattern of OSTE+ that is cured at 90 °C alters when irradiated, potentially due to the thermal impact of the X-ray beam. Although OSTE+ that is cured at 150 °C does not alter, it shows staining similar to OSTE+ that is cured at 90 °C. However, neither the alteration nor the staining is a big problem for the use of OSTE+ for in-situ SAXS. In order to use OSTE+ without potential changes in the scattering pattern, the devices just have to be subjected to an appropriate curing temperature.

4.5 Results from the In-situ SAXS Synchrotron Experiments

In the previous sections, a OSTE+ microfluidic device was developed, which was characterized regarding its compatibility with X-rays. Beyond that, the working conditions were developed to study the precipitation of cerium oxalate in droplets by in-situ SAXS. In the following, the method for isolating the droplet signal will be presented and applied to different systems. It will be used to isolate pure water droplets and droplets that contain gold nanoparticles. Furthermore, the method will be used to study the precipitation of cerium oxalate in pure water and in a binary solvent.

The SAXS experiments were conducted at the beamline SWING of the synchrotron SOLEIL at ambient temperature and pressure. In order to achieve a beam that is small enough for the microfluidic channel, its size was set to 50 μm \times 125 μm (vertically \times horizontally) by adjusting the alignment slits. This reduces however, the photon flux. The acquisition was shutter-controlled and the beam was aligned to the microfluidic channels by a periscopic camera and transmission scanning. Each sampling position was probed by repeatedly acquiring a scattering image with an acquisition time of 20 to 50 ms and a gap time of, at least, half of the acquisition time before the next acquisition. The experimental setup is depicted in Figure II.31.

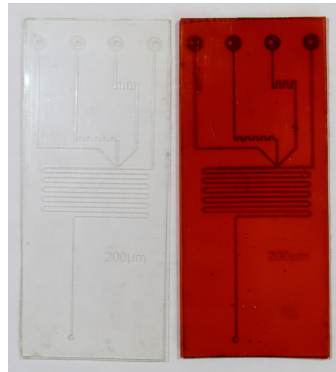


Figure II.28: Left: OSTE+ device after normal curing at 90 °C. Right: OSTE+ device after additional curing at 150 °C for 7 days.



Figure II.29: Staining observed on an OSTE+ device after an in-situ experiment.

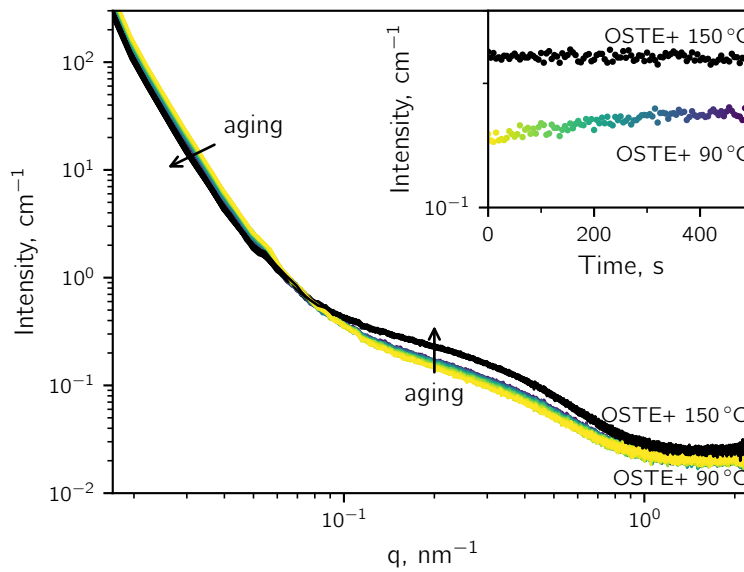


Figure II.30: Comparison of the aging behaviour of OSTE+ that was normally cured at 90 °C (OSTE+ 90 °C) and after additional curing at 150 °C (OSTE+ 150 °C) under the influence of X-rays at 16 keV. Inset shows the variation of the intensity at 0.2 nm⁻¹ with irradiation time.

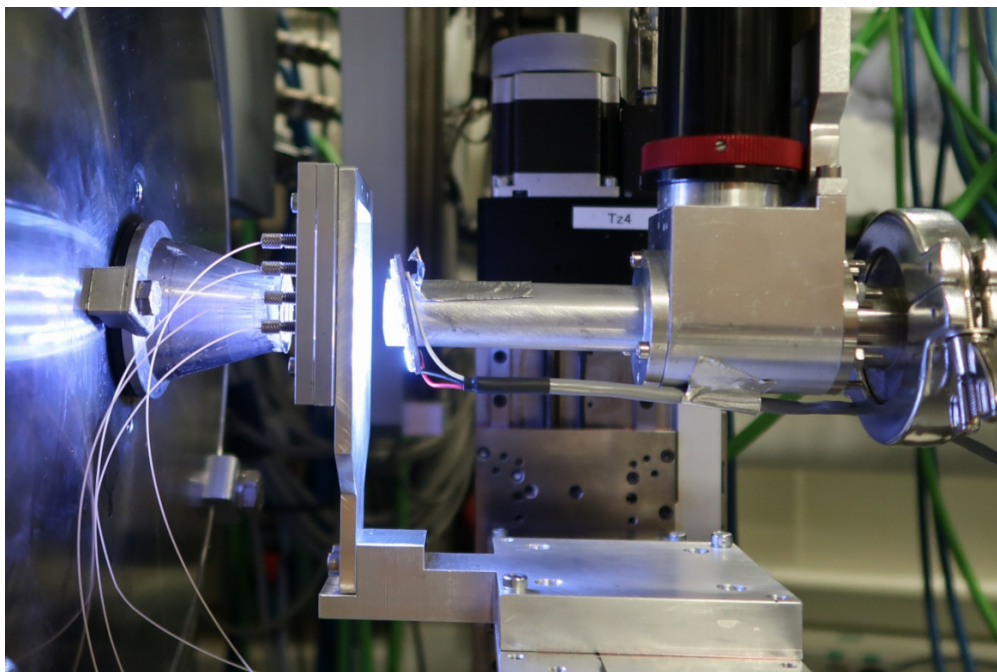


Figure II.31: Device mounted on the SWING beamline.

Data Treatment for Droplet Selection

For a segmented stream of oil and droplets, the described acquisition method results in scattering patterns from the oil phase, the droplet phase and patterns that have contributions from both phases (Figure II.11). Other authors solved this problem by treating and selecting the scattering images directly.^[59,60] In the present case, the selection takes place after azimuthal averaging of all images. Instead of integrating the intensity over the whole image, only a section is selected. Good selectivity was achieved in the region between 10 and 11.6 nm⁻¹ (Figures II.32 and II.33). In this region, no Bragg peak of cerium oxalate appears that might influence the selection. Furthermore, the scattering profiles of the two phases do not evolve in this region. They stay constant and different in intensity. The presented method also gives easy access to the scattering patterns of the oil phase, since they are not discarded before treatment (Figure II.33). This allows the analysis of both phases at the same time and might give insights into more complex systems that include the carrier phase into the reaction.

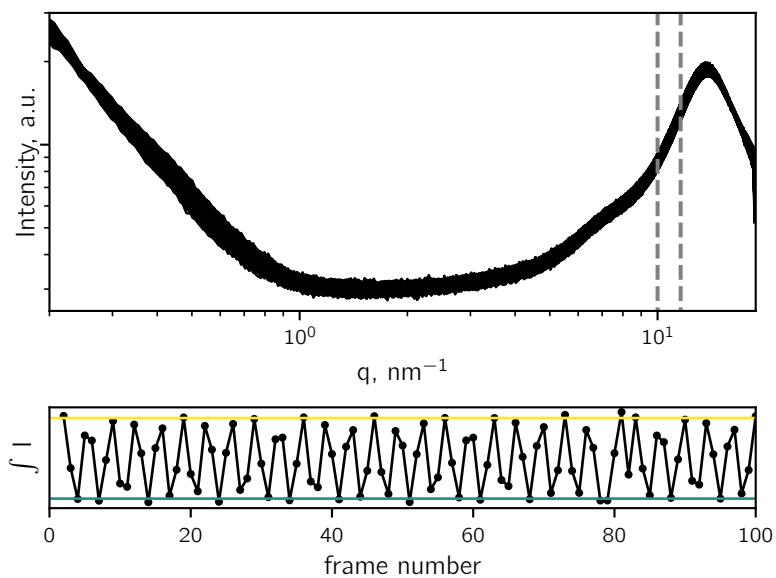


Figure II.32: Top: 100 scattering patterns that were acquired at one sampling point. The area between the grey lines is integrated for curve selection. **Bottom:** The integrated intensity is plotted for each frame. Based on their different scattering intensity, oil and droplet patterns can be isolated by defining threshold values (yellow line for oil, green line for droplet). The patterns between these threshold values are discarded, as they are associated with scattering from mixed oil/droplet sections.

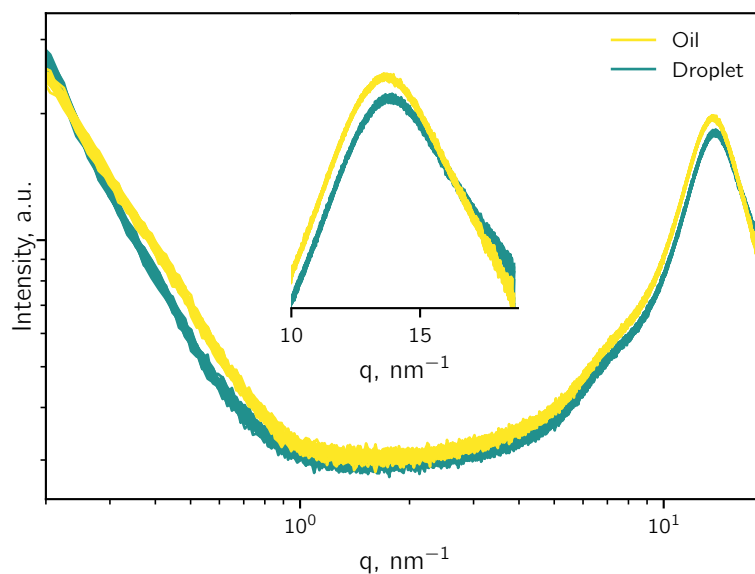


Figure II.33: Scattering patterns after selection (Figure II.32). Oil and droplet phase are separated. The inset is a zoom on the region above 10 nm^{-1} .

Gold Nanoparticles in Droplets

In order to test if scattering objects can be identified inside the droplets, a gold nanoparticle suspension was investigated. They were prepared as described in Materials and Methods at a gold concentration of $254 \mu\text{M}$ and diluted to $212 \mu\text{M}$ inside the droplets by the microfluidic device. The characterization by SAXS and TEM evidenced a particle diameter of $9.4 \pm 1.0 \text{ nm}$ (Appendix A). The carrier phase was hexadecane with 0.2% (w/w) of Span 80 and the flow rates were $5 \mu\text{L} \cdot \text{min}^{-1}$ for the gold dispersion, two times $0.5 \mu\text{L} \cdot \text{min}^{-1}$ for water and $4 \mu\text{L} \cdot \text{min}^{-1}$ for the oil phase. Measurements were carried out in a OSTE+ device without surface treatment at 16 keV.

Figure II.34 shows the scattering curves of spherical gold nanoparticles, measured in a capillary as reference, in the device feeding channel and inside droplets. For the reference capillary, the larger sample diameter and a longer acquisition time result in a smooth curve, showing the first two oscillations of the gold nanoparticles. The data from the microfluidic chip is rather noisy due to the low intensity of the X-ray beam, but still allows the observation of the first part of the gold nanoparticle form factor below 1 nm^{-1} . The observed absolute signal intensity of the particles inside the capillary is 1.6 times larger than the signal obtained in the feeding channel and 3.2 times larger than the signal obtained in the droplets. This

might indicate a lower concentration in the feeding channel compared to the reference capillary and an even lower concentration in the droplets. However, the same concentration was used for the reference and the feeding channel and the dilution in the droplet does not explain the decrease in intensity. The cause for this quantitative mismatch is probably a consequence of the low beam intensity. Nevertheless, the identification of the particles inside the droplets in a 150 μm channel at a concentration of 212 μM is possible. In order to probe the impact of the beam intensity and to follow reactions in the microfluidic chip, the intensity should be increased by using a microfocused beam.

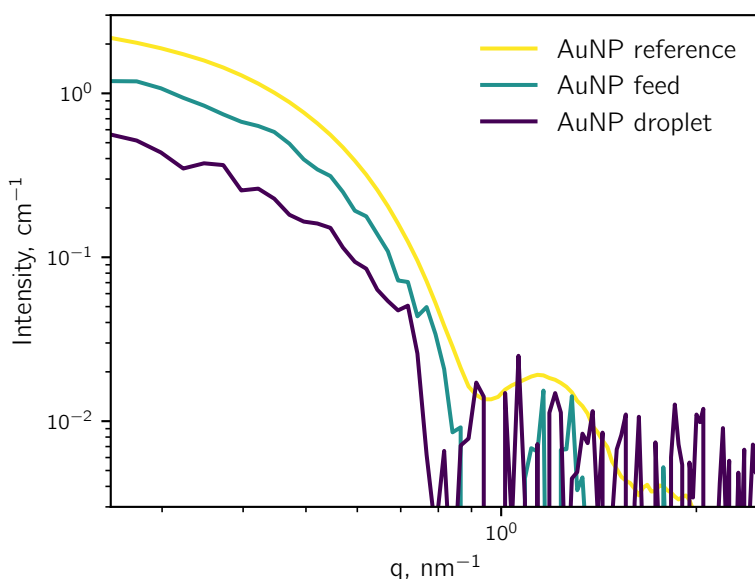


Figure II.34: SAXS patterns of gold nanoparticles (AuNP) from a Kapton capillary as reference and inside the microfluidic device from the feeding channel and from the droplets. Data collected at 16 keV.

Cerium Nitrate and Oxalic Acid in Water Droplets

In order to observe temporal changes during the precipitation of cerium oxalate, the precursor solutions were encapsulated into a droplet, mixed and several positions along the microfluidic channel were probed. The energy was changed from 16 to 12 keV in order to increase the photon flux. Measurements were carried out in OSTE+ devices and polyimide/OSTE+ devices with surface treatment. The flow rates were 4 $\mu\text{L} \cdot \text{min}^{-1}$ for water in the central channel of the junction, 0.5 $\mu\text{L} \cdot \text{min}^{-1}$ for 0.10 M $\text{Ce}(\text{NO}_3)_3$, 0.5 $\mu\text{L} \cdot \text{min}^{-1}$ for 0.15 M $\text{H}_2\text{C}_2\text{O}_4$ and 6 to 10 $\mu\text{L} \cdot \text{min}^{-1}$ for the oil phase (light mineral oil with 1% (w/w) of

Span 80).

Due to the exploratory character of the experimental run, the appropriate background scattering was not collected for each measurement point. In order to compensate, the following strategies were applied for the presented results. For the observation of the oil phase, the scattering of the empty corresponding positions on the device and a proportionate amount of the pure oil scattering were subtracted. Background subtraction for the droplet phase was carried out by subtracting the scattering signal of the water inlet. For the droplet signal, the lack of the proper background potentially leads to artifacts in the scattering pattern from the over- or underestimation of the OSTE+ wall thickness, but should not interfere with the qualitative trends. Artifacts from the oil lubrication film around the droplet, should not appear since its thickness can be estimated to be below 1 μm in total.^[141]

Figure II.35 shows the temporal evolution of the scattering in the oil phase. For each point, a signal is visible that has a higher intensity than the background and that decreases in intensity from low to high values of q . This is characteristic of electronic density fluctuations in the solution and indicates the presence of nanometer sized objects. From the first sampling point to the last, the observed minimum between 1 and 2 nm^{-1} shifts to lower values, while the intensity below 1 nm^{-1} increases. After P4, the changes are only minimal and the process appears to be finished. This observation could be explained by the presence of reverse micelles in the oil phase that swell by extracting water or reactants from the droplets. The high similarity between the in-situ experiment and patterns of the same oil phase that was equilibrated with different aqueous solutions (oil:water, 50:50, v/v) supports this interpretation (Figure II.36). Before equilibration, the scattering of small spherical objects is visible. After equilibration with water, the scattering intensity decreases. The observation can be probably linked to the swelling of the reverse micelles due to the integration of water into the micelle core. By transitioning from a micelle core that consists of surfactant head groups alone to a mixture of head groups and water, the scattering length density of the micelle core decreases. Due to the corresponding decrease in electronic contrast between the micelle core and the alkyl chain of the surfactant, the observed scattering intensity decreases as well. No decrease is observable for the solutions that contain reactants, which might indicate a higher scattering length density in the reverse micelle core caused by the presence of oxalic acid or cerium nitrate. In addition, the scattering signal intensity decreases at a lower q value, which indicates a larger particle size for the reverse micelles that contain $\text{Ce}(\text{NO}_3)_3$ or oxalic acid, compared to water alone. Fitting the equilibrated scattering patterns with a model of polydisperse spheres yields an approximate size of $3.6 \pm 0.8 \text{ nm}$ for the Span 80 alone, $4.4 \pm 0.6 \text{ nm}$ for equilibration with 0.10 M oxalic acid

and 4.6 ± 0.6 nm for equilibration with 0.15 M $\text{Ce}(\text{NO}_3)_3$. The lower scattering intensity of the sample that was equilibrated with water alone renders it difficult to determine an object size. Due to the similarity of the position of the slope however, it is possible to estimate the size to be quite similar to the object size for Span 80 alone.

For the in-situ data, relative information regarding the object size can be obtained from the curve shape. Due to the low signal to noise ratio, direct fitting was not possible. Compared to the SAXS patterns of the equilibrated samples, the observed minima shift from around 2 nm^{-1} towards 1 nm^{-1} , indicating the presence of larger objects. By comparing the experimental data to a model of polydisperse spheres (Figure II.35) the objects can be estimated to grow from 4.0 to 6.5 nm. Compared to the objects in the equilibrated mineral oil, the difference in size is probably not only related to an extraction, but could be explained by the growth of cerium oxalate particles inside the reverse micelles. For future experiments pre-equilibrated light mineral oil with 1 % (w/w) Span 80, or an entirely different oil/surfactant combination, should be used in order to reduce the influence of the extraction on the reaction.

The scattering patterns of the droplets show slopes that scale with $\approx q^{-3}$ and a small bump below 1 nm^{-1} (Figure II.37). With increasing droplet age, the bump shifts its position towards smaller q values, indicating the growth of scattering objects. After subtraction of a q^{-3} slope, the bump gets even more pronounced, evidencing the growth of globular objects (Figure II.38). The position of the bump is similar to the patterns that were observed in the oil phase. From the comparison to the theoretical curves of polydisperse spheres, it can be estimated that these objects grow from 4.0 nm at P1 to 6.5 nm at P6. Comparing the plateaus of the scattering curves of the spherical objects at small q -values shows that the scattering intensity in the oil phase is approximately 10 times larger than in the droplet phase. Due to the similarity in shape, a probable explanation is a convolution of the oil and droplet signal, due to a slightly too long acquisition time for a flow rate of $15 \mu\text{L} \cdot \text{min}^{-1}$. The q^{-3} slope at low q values however, indicates the presence of a 3-dimensional organization inside the droplets.

For a slower flow rate ($10 \mu\text{L} \cdot \text{min}^{-1}$) the droplet data still shows the q^{-3} slope at low q values, but no contribution by the oil phase is apparent (Figure D.2). Unfortunately, the correct background scattering for this data set was not collected. Hence, it is not considered any further.

Rodríguez-Ruiz et al. probed the cerium oxalate precipitation up to a reaction time of 0.7 s in a single phase microfluidic SAXS experiment.^[25] However, the scattering vector

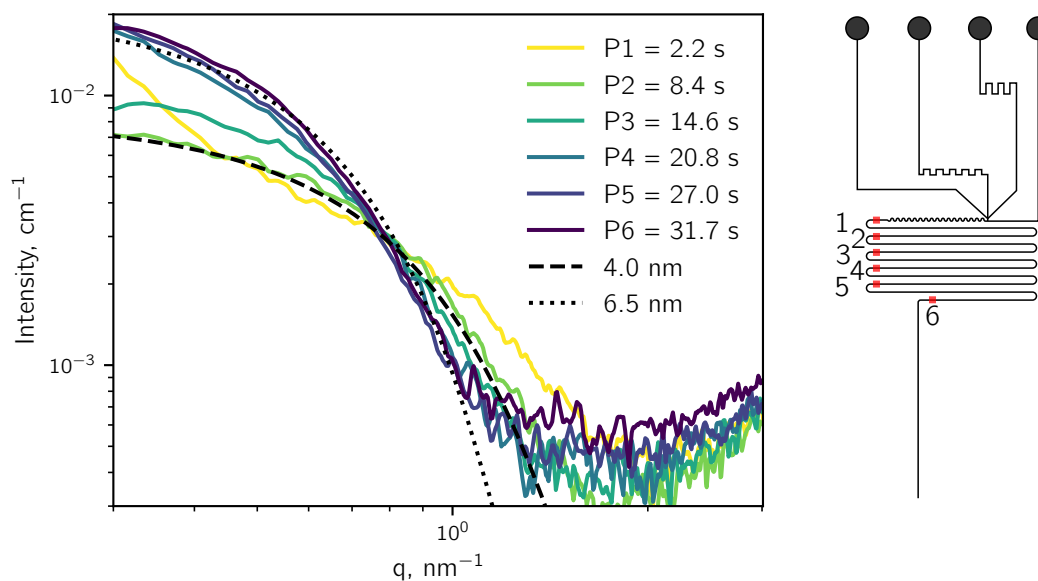


Figure II.35: Left: SAXS patterns of the oil phase at different points in the microfluidic channel. The broken lines indicate the scattering signal that would be generated by spherical objects of 4.0 ± 1.0 and 6.5 ± 1.0 nm diameter. Right: Sampled points on the microfluidic device. Data collected at 12 keV.

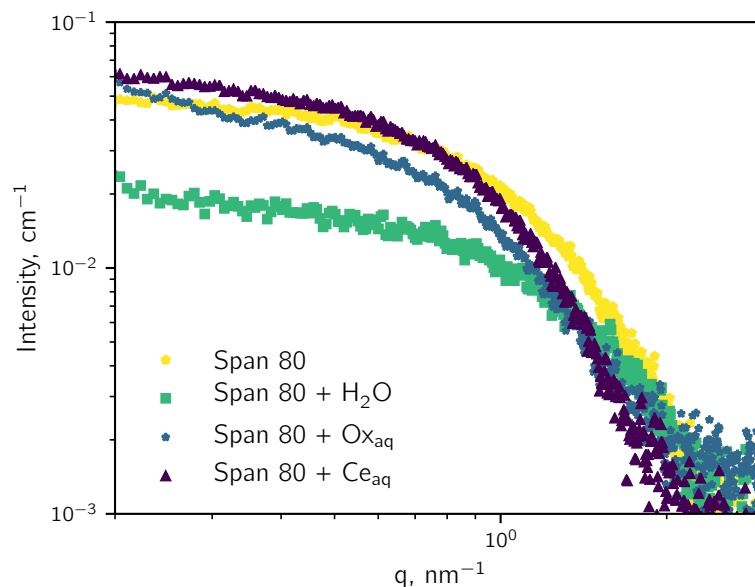


Figure II.36: SAXS patterns of 1% Span 80 (w/w) in light mineral oil before and after equilibration with H_2O , 0.15 M $\text{H}_2\text{C}_2\text{O}_4$ (Ox_{aq}) and 0.10 M $\text{Ce}(\text{NO}_3)_3$ (Ce_{aq}). Background and scattering of light mineral oil are subtracted. Data collected at 8.04 keV.

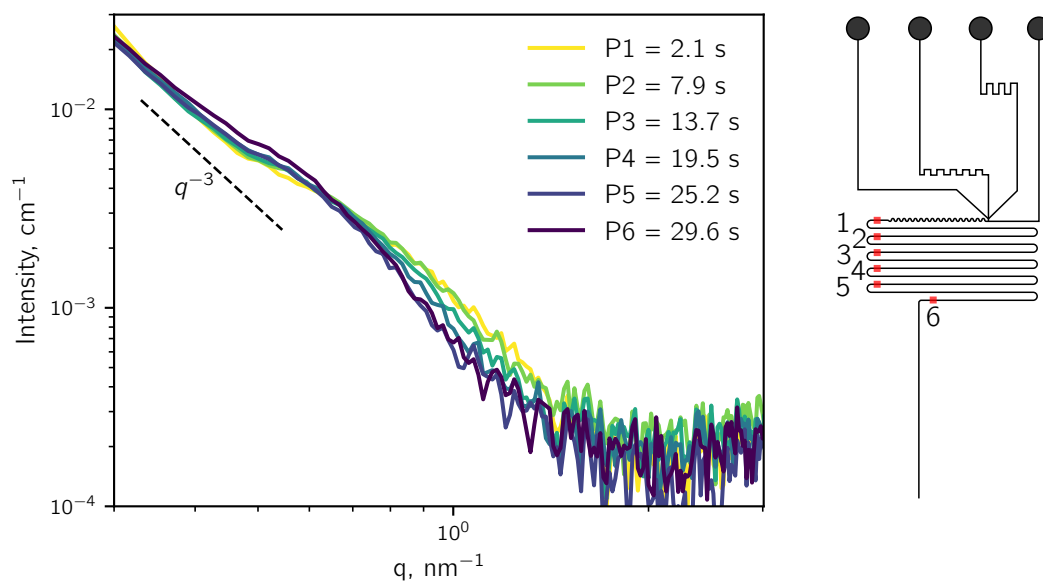


Figure II.37: Left: SAXS patterns of the droplet phase at different points in the microfluidic channel. Right: Sampled points on the microfluidic device. Data collected at 12 keV.

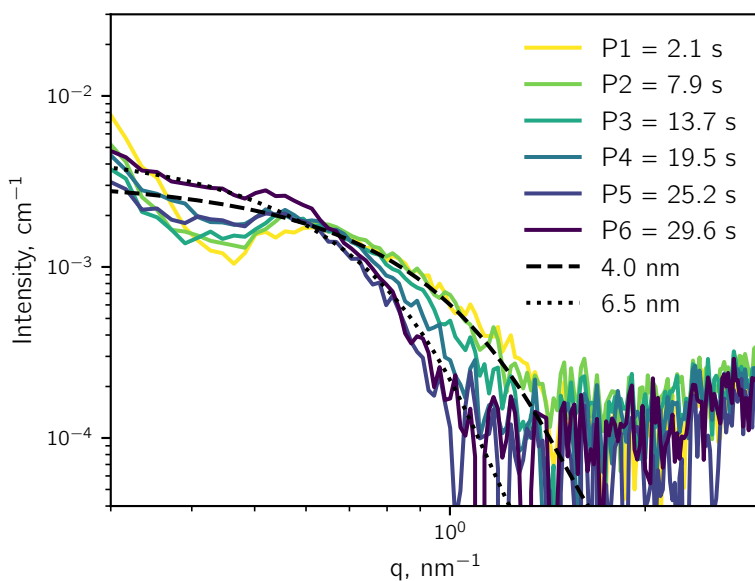


Figure II.38: Droplet scattering patterns after subtraction of the q^{-3} slope. The broken lines indicate the scattering signal that would be generated by spherical objects of 4.0 ± 1.0 and 6.5 ± 1.0 nm diameter.

of their study does not overlap with the present data. They observed a slope of $\approx q^{-3.2}$ for a reaction time of ≈ 0.3 s, which quickly developed into $\approx q^{-4}$ for a reaction time of 0.7 s. This behavior somewhat resembles the observation in Figure II.37, where the q^{-3} slope becomes steeper with increasing reaction time. The timescale however is different. A potential shift in reaction kinetics could be caused by the spatial confinement inside the droplets.

In order to elucidate the origin of the observed scattering signals, a more intense beam is necessary (e.g. a microfocused beam) and an additional oil/surfactant system should be used to probe its influence on the reaction. Nonetheless, the results evidence that it is possible to follow the evolution of a reaction in the OSTE+ microfluidic device by SAXS.

Cerium Nitrate and Oxalic Acid in Binary Solvent Droplets

The use of a binary solvent consisting of water and 1,2-propanediol was reported to yield spherical aggregates of needle like cerium oxalate crystals.^[27] Although the precipitation behavior of cerium oxalate in the binary solvent was described as similar to the behavior in water,^[27] the higher viscosity is expected to influence the reaction kinetics. The use of time-resolved SAXS aims to give insights in understanding its reactivity and aggregation behavior.

The flow rates were $3 \mu\text{L} \cdot \text{min}^{-1}$ for the carrier phase (light mineral oil with 1% (w/w) of Span 80), $1 \mu\text{L} \cdot \text{min}^{-1}$ for the binary solvent (water:1,2-propanediol in a 25:75 (w/w) ratio) in the central channel of the junction, $0.5 \mu\text{L} \cdot \text{min}^{-1}$ for 0.10 M $\text{Ce}(\text{NO}_3)_3$ and $0.5 \mu\text{L} \cdot \text{min}^{-1}$ for 0.15 M $\text{H}_2\text{C}_2\text{O}_4$. Measurements were carried out in a OSTE+ device with surface treatment at 12 keV.

Due to a higher ambient temperature during the in-situ experiments, compared to the bench-top experiments, it was not possible to obtain a controlled droplet pinch-off or stable segmented flow. A change in temperature strongly influences the surface tension and viscosity of a system. Hence, the observed flow patterns can change drastically, as observed in the present case. The carrier phase and the aqueous phase passed the mixer in a co-flow and the reactants were in contact along this path. At the end of the mixer droplets formed, but coalesced again downstream. At the position with droplets present, the droplets were rather small. Due to the use of a too long acquisition time for the reduced droplet size, the obtained droplet scattering signal is convoluted with oil signal.

After subtraction of the background (sample environment and binary solvent) from the

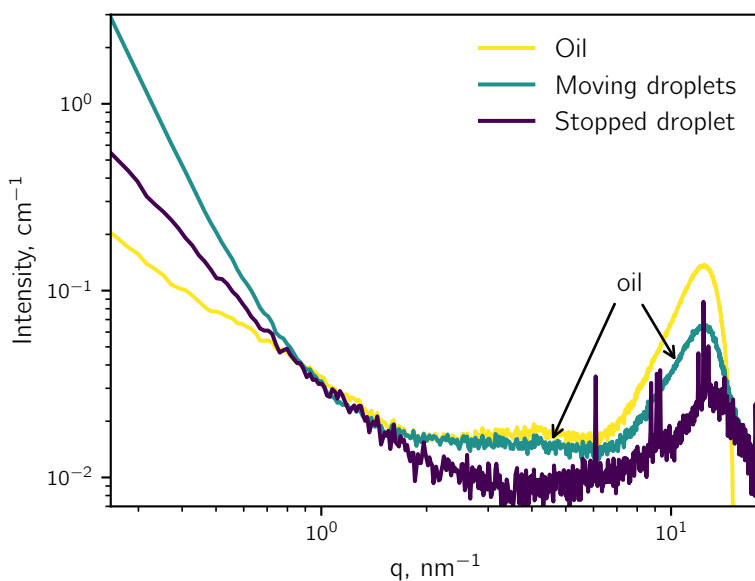


Figure II.39: In-situ scattering patterns of cerium oxalate formation in binary solvent. Data collected at 12 keV.

droplet signal, the oil contribution manifests as a peak above 10 nm^{-1} (Figure II.39) and an overall increased scattering. Subtracting the binary solvent from the pure oil phase yields the same peak and confirms the assignment. Apart from the oil contribution, the scattering pattern also shows a q^{-4} slope below 1 nm^{-1} , which might originate from scattering objects inside the droplets, the interface between oil and droplet, or from both.

To observe the evolution of the droplet signal, the flow was stopped and the scattering pattern of several quasi-stationary droplets was collected. The droplets quickly showed the typical cerium oxalate Bragg peaks and the slope below 1 nm^{-1} decreases to q^{-2} . A decrease of the slope during the reaction is in agreement with observations from macroscopic mixing experiments.^[142] Thus, it should be possible to observe the growth of crystals in the OSTE+ device in future studies. However, a stable oil/surfactant combination for the binary solvent system has to be identified first, or the temperature has to be better controlled.

Identified Problems

During the experimental run several problems arose, that will be discussed in the following.

i) *Photon Flux.* Unfortunately, no microbeam optics were available during the synchrotron experiment. As a consequence, the slit positions were adjusted to obtain a small enough beam size, which reduced the photon flux. Figure II.40 shows a typical scattering image for 16 keV and an acquisition time of 20 ms. Due to the low photon flux many pixels stay unexposed, giving a subpar scattering signal. To increase the possible maximum acquisition time, the device holder was rotated by 90° so that the channel is parallel to the short dimension of the beam (Figure II.41).

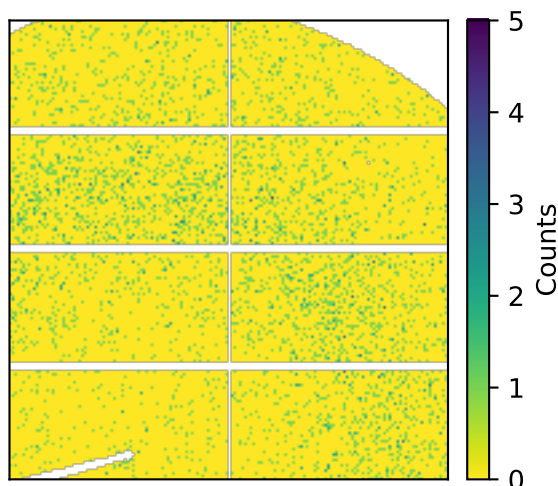


Figure II.40: Typical detector photon counts after 20 ms of acquisition at 16 keV for an in-situ experiment.



Figure II.41: Relative alignment of the beam (solid white line) and the channel. **Left:** The channel is parallel to the long beam dimension. **Right:** The channel is parallel to the short beam dimension, which allows for longer acquisition times (indicated by the dashed white line) compared to the other configuration.

ii) *Temperature Control.* One of the biggest problems was the lack of a temperature control unit. Temperature does not only have an influence on the reaction kinetics, but also on surface tension and viscosity. The temperature differences from the laboratory to the experimental hutch of the beam line were in the range from 5 to 10 °C. This difference was enough to shift the droplet pinch-off and wetting behaviour of the experimental systems.

The only carrier phase that was available and usable for in-situ reactivity experiments was light mineral oil with 1 % (w/w) of Span 80. This oil phase was not previously tested for the reactivity in water droplets.

iii) Device Holder. Another unforeseen problem arose from the way in which the IMT device holder was mounted to the beamline interface. When the screws to hold the device holder on the interface were tightened, the device holder was tightened, too. The exerted force caused a shift of the relative position of the inlets and the access holes in the device, leading to a blocked inlet and missing reactant flow during several experiments. Therefore, a new device holder was designed and machined from PMMA (Figures II.42 and II.43 and Appendix B). It combines a PMMA body with NanoPorts (Upchurch Scientific) and is working for low pressures. It can easily be adapted to the interface of the SWING beamline. One major improvement is the transparency of PMMA, which will allow to check the correct alignment of tubing and microfluidic device.



Figure II.42: Top view on the PMMA device holder.



Figure II.43: Side view on the PMMA device holder.

Summary

The first synchrotron experiments showcased that the developed OSTE+ device can be used to observe particles inside droplets and that it has the capabilities to follow the structural changes of a system during crystal formation, even with low beam intensities. Furthermore, the necessity of using mineral oil as carrier phase and the isolation of the oil signal enabled the observation of an extraction event due to the presence of surfactants in the oil phase.

5 Conclusion and Perspective

So far, droplet microfluidic in-situ SAXS was used for the observation of gold nanoparticles,^[29] to study the influence of different salt concentrations on proteins,^[57] to obtain the time constant for protein self-assembly^[59] and to study the induction time for a precipitation reaction.^[60] For three of them the actual measurement was performed in a capillary after droplet generation in a microfluidic device, while only one performed the experiments directly in the device.^[60] In all of these studies fluorinated oils were used and the total fluid velocity was below $6 \text{ mm} \cdot \text{s}^{-1}$ in studies that isolated the droplet signal. It is however hard to directly compare the performance of the different devices, since some are used under vacuum, while others are not and some use a microfocused beam while others have a standard beam.

In this chapter a protocol has been presented that reliably yields high quality OSTE+ microfluidic devices with a total window thickness of OSTE+ below $400 \mu\text{m}$. The prepared OSTE+ devices are resistant to alkanes and can be used for bench-top and in-situ SAXS experiments on a synchrotron beam line. By using the scattering signal at large q values, the droplet and oil signals can be separated from intermediate ones, even at a low photon flux. The developed method can be used to identify gold nanoparticles in droplets, the growth of reverse micelles in the oil phase and freshly grown cerium oxalate crystals inside droplets. Potentially it is also able to follow the growth of the cerium oxalate crystals inside aqueous droplets. The performance of the experimental set-up should be greatly increased by the use of a microfocused X-ray beam and the new device holder. Although not intended in the studied experiment, the setup is suited to study liquid/liquid extraction by in-situ SAXS and could probably be used to study more complex precipitation reaction that involve both phases, e.g. phase transfer followed by a precipitation reaction. Achieving even thinner OSTE+ walls would be desirable, but more development effort is necessary.

In order to study the precipitation of cerium oxalate in droplets, the use of surfactants is

necessary to prevent the device from blocking. However, the use of a surfactant can also lead to unwanted side-events such as the formation of reverse micelles in the oil phase and the potential extraction of reactants. To ensure well defined experiments, different surfactant-oil systems should be evaluated for future studies. Additionally, a strategy should be developed to work at a defined temperature, especially since temperature control is important for a stable droplet generation and a reproducible reactivity.

After handling the identified problems properly, the OSTE+ device will be able to give more detailed insights into precipitation reactions and is expected to be usable for kinetic studies on different systems, e.g. proteins and particles formation.

Furthermore, it can be imagined that the microfluidic device can be used for in-situ X-ray absorption near edge structure or extended X-ray absorption fine structure experiments.

III Transformation of Imogolite into a Lamellar Phase with Interfacial Properties by Decylphosphonic Acid

The content presented in this chapter has been partially published in Langmuir.^[143]

1 Introduction

Apart from stabilization by surfactants, emulsions can also be stabilized by solid particles (Figure III.1). Such particle-stabilized emulsions were first reported by Ramsden^[144] and Pickering^[145] and are now commonly known as Pickering emulsions. Depending on the phase preference of the particles, water-in-oil or oil-in-water emulsions can form.^[146]

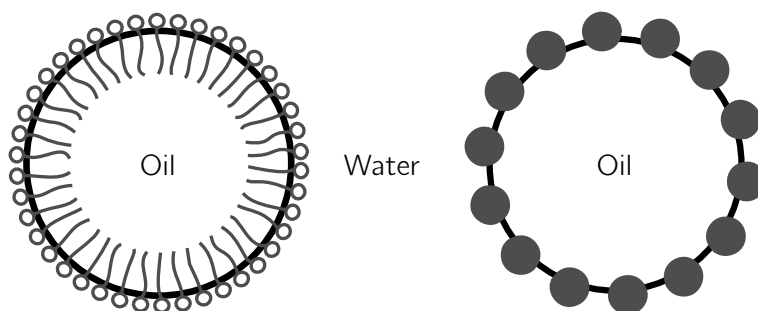


Figure III.1: Scheme of oil in water emulsion droplets. **Left:** Stabilization by surfactant molecules with a hydrophilic head and a hydrophobic tail. **Right:** Stabilization by adsorbed particles in a Pickering emulsion.

Recently, Pickering emulsions stabilized by surface modified imogolite nanotubes have been reported.^[30] Such emulsions might be interesting as model systems to study ion transport through the inner lumen of imogolite and could be used to control reactions inside the

droplets by controlling reactant feeding rates. The usefulness of a similar approach was recently demonstrated for halloysite nanotube Pickering emulsions.^[147]

Imogolite ($\text{Al}_2\text{O}_3\text{Si}(\text{OH})_4$) is a natural clay mineral that appears in volcanic ash soils and is synthetically accessible.^[148–150] The nanotubes have a diameter of 2 to 3 nm and an inner pore diameter of around 1 nm.^[149,151–153] Its structure features a gibbsite-like ($\text{Al}(\text{OH})_3$) sheet with orthosilicate ($\text{O}_3\text{Si}(\text{OH})$) groups on one side (Figure III.2). The Al sites are octahedrally coordinated and each site is coordinated to three other Al by two $\text{Al}-\text{O}(\text{R})-\text{Al}$ bridges. One bridge is protonated ($\text{Al}-\text{O}(\text{H})-\text{Al}$), while the other is coordinated to Si ($\text{Al}-\text{O}(\text{Si})-\text{Al}$). These Si atoms are tetrahedrally coordinated by oxygen. One oxygen is protonated, while the other three are coordinated to six Al octahedra through three $\text{Al}-\text{O}(\text{Si})-\text{Al}$ bridges. The mismatching sizes of the SiO_4 tetrahedra and the AlO_6 octahedra are partially responsible for the curvature, which leads to the formation of a tube (Figure III.3).^[149] On the internal surface, silanol groups ($\text{Si}-\text{OH}$) are present, while the bridging aluminol groups ($\text{Al}-\text{O}(\text{H})-\text{Al}$) are present on the external surface. To represent this structure, the unit formula is often written as $(\text{OH})_3\text{Al}_2\text{O}_3\text{Si}(\text{OH})$. The minimum strain energy for the tubular structure has 12 formula units per circumference giving a diameter of 2.3 nm.^[154] However, the diameter of synthesized and natural samples can differ from this value.

The tube diameter can be modulated by choosing different conditions and precursors during synthesis, e.g. the synthesis temperature,^[157] through the presence of different anions,^[153] substituting Si with Ge^[158] or using a methylated Si precursor.^[159] The latter does not only increase the tube diameter, but also turns the otherwise hydrophilic tube interior hydrophobic.^[152,159] Its versatile nature and typical dimensions make imogolite tubes interesting candidates for nanoconfinement,^[156,160] desalination and water treatment,^[161,162] as well as polymer reinforcement.^[163–166]

The hydrophilic tube exterior limits the applicability of imogolite nanotubes in hydrophobic environments. In order to overcome this limitation, diverse approaches were proposed to modify the surface of imogolite. The studies focusing on the modification after the synthesis of imogolite are summarized in Table III.1. They are grouped by the type of reactant used to anchor organic molecules on the surface of imogolite. The three main groups are silanes, phosphates and phosphonates. Table III.1 also indicates the aggregation state of the used imogolite tubes. In many cases, dispersed imogolite is dried and re-dispersed before modifying the material. Since the individual imogolite tubes aggregate into tube bundles during the drying process, the probability to obtain individually modified tubes instead of

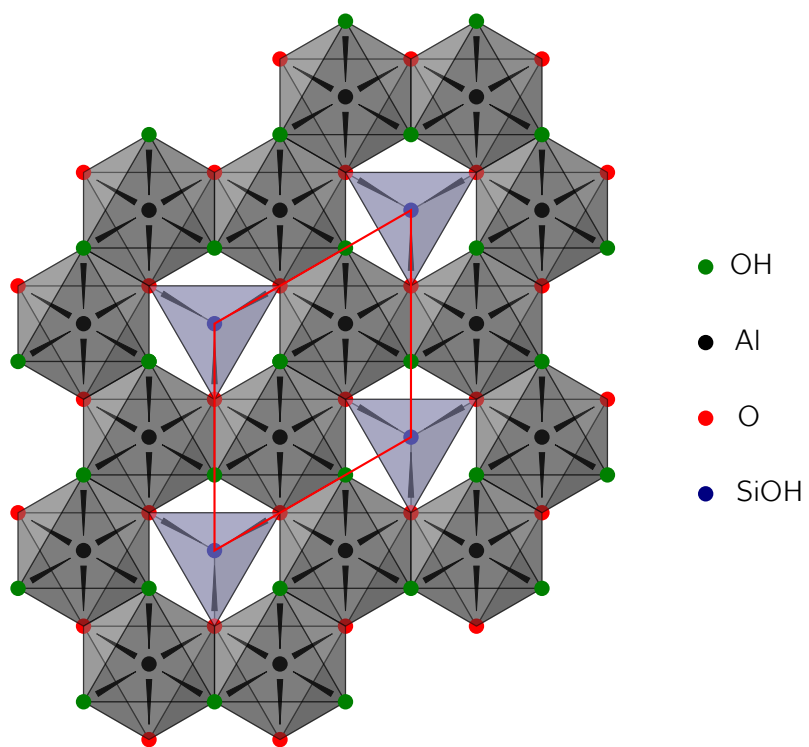


Figure III.2: A segment of the imogolite structure according to Cradwick et al.^[149] The unit cell is highlighted by the red line.

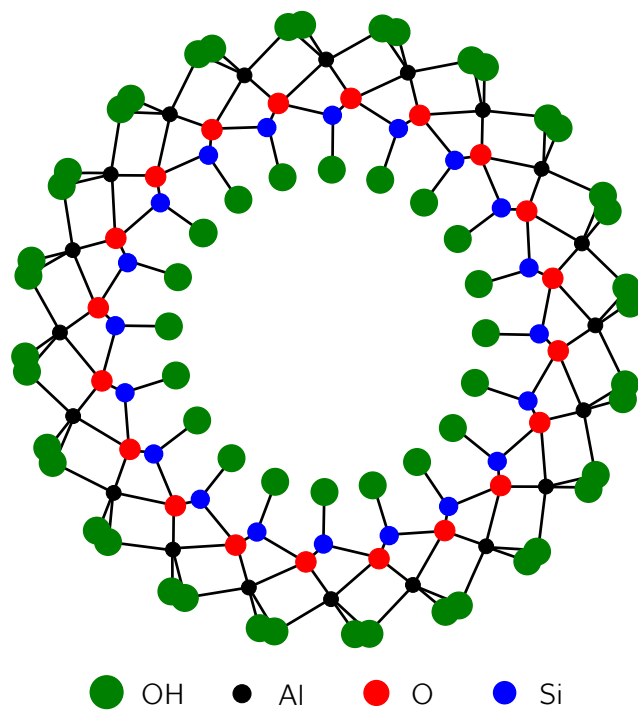


Figure III.3: Imogolite structure viewed down the tube axis as suggested by Cradwick et al.,^[149] adapted from MacKenzie et al.^[155] The tube interior is filled with water.^[156]

modified tube bundles is expected to be low. Studies that work directly with dispersed tubes are more likely to obtain individual surface modified imogolite tubes.

In the following, the main literature results regarding the different reactant groups will be discussed.

Silanes are well-studied reactants for surface modification.^[188–190] They form Si–O–X bonds with various substrates and can condensate with themselves by forming Si–O–Si bonds. The ratio between heterocondensation (Si–O–X) and homocondensation (Si–O–Si) determines the result of surface modification, i.e. monolayer quality and formation of multi-layers or side products.

Johnson and Pinnavaia studied the modification of imogolite by (3-aminopropyl)triethoxysilane in acidic aqueous conditions.^[167,168] They observed the formation of a protonated siloxane polymer on the external surface of imogolite that was labile to hydrolysis. However, they were not able to determine if it was physically adsorbed or chemically linked to imogolite. Zanzottera et al. were neither able to determine the binding mode, but they found some evidence for an increased reactivity of the tube ends towards (3-aminopropyl)triethoxysilane.^[173] Studies using (3-mercaptopropyl)trimethoxysilane^[169] and (3-chloropropyl)triethoxysilane^[171,172] do not report any data on the hydrolysis behavior of the deposited siloxane polymer.

Organophosphorous coupling agents are growing in popularity for the modification of surfaces.^[191] Compared to silanes, they are less prone to homocondensation and should only form strong P–O–X bonds.

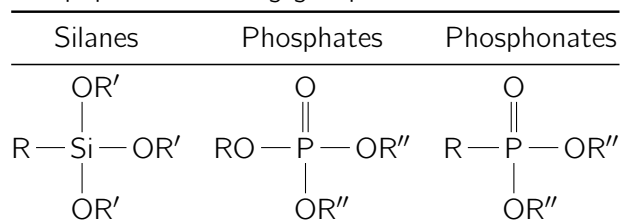
The first results regarding the adsorption of phosphate on imogolite were presented by Parfitt et al. in 1974.^[192] In 2005, Yamamoto et al. used this concept to modify redispersed imogolite powder with 2-(Methacryloyloxy)ethylphosphoric acid and incorporated the obtained material into a poly(methyl methacrylate) matrix.^[164] Ma et al. used diammonium phosphates for the modification.^[174–176] By using X-ray photoelectron spectroscopy, they were able to identify evidence for the formation of covalent links between the Al sites and the anchoring group for diammonium dodecylphosphate,^[174] whereas only electrostatic interactions were observed when using diammonium 8-(2-bromo-2-methylpropanoyloxy)octylphosphate^[176].

Among the different approaches, the phosphonic acid moiety is the most utilized anchoring group. Johnson and Pinnavaia were the first who suggested this compound group, but did not follow up with a publication.^[167] Ten years later, the first results on the chemisorption of octadecylphosphonic acid (ODPA) on imogolite were published by Yamamoto et al.^[166,177] They concluded that ODPA adsorbs to the surface of imogolite. Park et al. modified imogo-

Table III.1: Literature overview for the external surface modification of imogolite after synthesis. The generic structures of the most popular anchoring groups are listed in Table III.2.

Reactive Group	Compound	State of Imogolite	Authors
Silane	(3-aminopropyl)triethoxysilane	dispersed	Johnson and Pinnavaia [167,168]
	(3-mercaptopropyl)trimethoxysilane	unknown	Guilment et al. [169]
	(3-aminopropyl)triethoxysilane	dried	Qi et al. [170]
	(3-chloropropyl)triethoxysilane	dried	Guerra et al. [171,172]
	(3-aminopropyl)triethoxysilane	dried	Zanzottera et al. [173]
Phosphate	2-(Methacryloyloxy)ethylphosphoric acid	dried	Yamamoto et al. [164]
	Diammonium dodecylphosphate	dried	Ma et al. [174]
	Diammonium 8-(2-bromo-2-methylpropanoyloxy)octylphosphate	dispersed	Ma et al. [175,176]
Phosphonate	Octadecylphosphonic acid	dried	Yamamoto et al. [166,177]
	Octadecylphosphonic acid, Tetradecylphosphonic acid	dried	Park et al. [178]
	Octadecylphosphonic acid	dried	Bac et al. [179]
	(2-(5"-hexyl-[2,2':5',2"-terthiophenyl-5-yl)ethyl)phosphonic acid, (2-(5"-hexyl-1,1-dioxido-[2,2':5',2"-terthiophenyl-5-yl)ethyl)phosphonic acid	dried	Yah et al. [180,181]
	Octadecylphosphonic acid	dispersed	Picot et al. [30]
	Vinylphosphonic acid, Octadecylphosphonic acid	dispersed	Li and Brant [182,183]
Others	Benzaldehyde	dried	Shikkinaka et al. [184]
	1-(3,4-Dihydroxyphenyl)-4-hydroxy-1-butanethione	dried	Miura et al. [185]
	γ -irradiation	dried	Lee et al. [186], Ryu et al. [187]

Table III.2: Most popular anchoring groups for the modification of imogolite.



lite with ODPA and tetradecylphosphonic acid (TDPA).^[178] The product was dispersible in toluene and scanning tunneling microscopy pictures showed regular patterns that were attributed to homogeneously grafted imogolite. Bac et al. studied the reaction between ODPA and germanium imogolite tubes.^[179] They concluded successful grafting, although they observed the formation of a lamellar product in XRD. Picot et al. used ODPA modified imogolite to stabilize oil-in-water Pickering emulsions.^[30]

All studies demonstrate the reactivity of the phosphonic acid moiety with imogolite. However, the evidence for the presence of grafted phosphonic acid on dispersed imogolite tubes is ambiguous. The IR results only reveal the reactivity, but not the nature of the resulting phase.^[30,166,177,179,180,182,183] Changes in the organization of the product were revealed by XRD and SAXS, but led to different interpretations.^[30,178,179] Finally, the investigations by microscopy do not have the required resolution to evidence isolated grafted nanotubes with clarity or lack complementary characterization.^[178,180,181]

A possible alternative reaction path for imogolite is the formation of bulk aluminum phosphonate. This result is already known for the intercalation of gibbsite and kaolinite with phenylphosphonic acid (PPA),^[193] the modification of aluminum oxide by ODPA^[194] and PPA,^[195] as well as the modification of germanium imogolite by ODPA.^[179] Nonetheless, it was shown that choosing favorable conditions prevents the bulk phosphonate formation and enables grafting of alumina by octylphosphonic acid.^[196]

In order to obtain imogolite Pickering emulsions to study the transport through the tubes and to study the influence of transport on a reaction inside the droplets, imogolite tubes are modified with alkylphosphonic acids, the most promising approach from literature. Since the literature lacks a full characterization of the resulting material and all studies are based on the first tentative results, the reaction of imogolite with (decyl)phosphonic acid is revisited, characterized in detail and the observed reactivity is explained by the surface chemistry of imogolite. The chemical and structural modifications of imogolite were studied by a combination of Infra-Red (IR) spectroscopy, Small Angle X-ray Scattering (SAXS), Scanning

Electron Microscopy (SEM), Transmission Electron Microscopy (TEM) and multinuclear Magic-Angle Spinning Nuclear Magnetic Resonance (MAS NMR).

Furthermore, the product obtained from the reaction of DPA and imogolite is used to form water-in-oil Pickering emulsions and to stabilize macroscopic water droplets on an oil-water interface. The behavior at the oil-water interface is related to the observed structure and compared to literature.

2 Materials and Methods

2.1 Synthesis of Imogolite

Chemicals were purchased from Sigma-Aldrich and used as received. The protocol was adapted from Farmer et al.^[150]

Tetraethoxysilane was fed to a stirred 2 mM solution of AlCl_3 until a Si/Al ratio of 0.55 was reached. Then, a 0.1 M NaOH solution was added under vigorous stirring, until an OH/Al ratio of 2 was reached. The suspension was kept for 5 days at 90 °C in an oven. Afterwards, a 10 kDa membrane (SpectrumLabs) was used to concentrate the imogolite dispersion up to $10 \text{ g} \cdot \text{L}^{-1}$ by ultrafiltration. Gibbsite traces were removed by consecutive centrifugation at 10 000 rpm for 1 h. Finally, the dispersion was dialyzed against MilliQ water until a residual conductivity of less than $2 \mu\text{S} \cdot \text{cm}^{-1}$ was reached. The resulting transparent dispersion was stored in a plastic container.

2.2 Reaction of Decylphosphonic Acid and Imogolite

Imogolite nanotubes were modified with decylphosphonic acid (DPA) by adapting the protocols described in literature.^[30,166,177–179] The different sample conditions are listed in Table III.3. For samples A1-A4 and B, 10 mL of aqueous imogolite dispersion ($5 \text{ g} \cdot \text{L}^{-1}$) were diluted with ethanol (CARLO ERBA Reagents, p.a.) under strong stirring. Decylphosphonic acid (DPA, Sigma-Aldrich, 97%) was dissolved in ethanol and then added to the imogolite dispersion. The resulting mixture was stirred at room temperature and turned whitish during reaction. The dispersed precipitate was collected by centrifugation and washed by three dispersion–centrifugation steps in ethanol. The sediment was finally dried under ambient conditions. For sample A5, DPA was dissolved in an aqueous ethanol solution (66:34 v/v, EtOH:H₂O) before adjusting the pH with 0.1 M NaOH (Sigma-Aldrich). The remaining

procedure is unchanged. The reaction was typically stopped after one day (samples A1-A5) to characterize the product. In order to obtain a complete reaction, one sample was kept stirring for 18 days (sample B). Sample A2 is a repetition of sample A1, in order to check the repeatability for a given set of preparation conditions. Samples A3 and A4 have a smaller P:Al ratio compared to sample A1. Sample A5 was prepared in order to observe the influence of the initial acidity. To investigate on the impact of the alkyl chain length, different phosphonic acids were investigated. For sample C octadecylphosphonic acid (ODPA) was used, for sample D butylphosphonic acid (BPA) and for sample E methylphosphonic acid (MPA). The reaction conditions correspond to the described protocol (Table III.3).

Table III.3: Investigated reaction conditions between imogolite and different phosphonic acids. Sample names, the used phosphonic acid, the molar ratio between phosphorous and aluminum, the final concentration in DPA, the volumetric solvent ratio (ethanol:water), and the stirring time for each sample.

Sample	PA	P:Al	c_{PA} , (mmol · L ⁻¹)	Solvent ratio, EtOH:H ₂ O	Reaction time, (days)
A1	DPA	5	5	95:5	1
A2	DPA	5	5	95:5	1
A3	DPA	3	3	95:5	1
A4	DPA	1	1	90:10	1
A5 ^a	DPA	5	5	62.5:37.5	1
B	DPA	5	5	95:5	18
C	ODPA	5	5	95:5	1
D	BPA	5	5	85:15	9
E	MPA	5	5	85:15	9

^a pH adjusted to 5

2.3 Infrared Spectroscopy

IR Spectra were collected from 4000 cm⁻¹ to 400 cm⁻¹ with a resolution of 4 cm⁻¹ (Vertex 70, Bruker). KBr pellets were prepared by compressing a dispersion of approximately 1 mg of sample in 100 mg of KBr.

2.4 Magic Angle Spinning Nuclear Magnetic Resonance Spectroscopy

The data has been collected on a Bruker Avance II 500WB spectrometer operating at a magnetic field of 11.72 T using ZrO₂ rotors with an outer diameter of 4 mm and Bruker HX and HXY CPMAS probes at a spinning frequency of 12 500 Hz.

²⁷Al ($I = \frac{5}{2}$) MAS NMR spectra were acquired using a short single-pulse excitation of 1 μ s (tip angle $\approx 10^\circ$, to ensure quantitiveness of the spectra because of the non-homogeneous excitation of all sites with respect to their quadrupolar interaction strength) and a recycle delay of 1 s. Two-dimensional Multiple Quantum MAS (MQMAS, the triple quantum transition was used) were acquired using the three-pulse Z-filter sequence.^[197] ²⁷Al MAS NMR spectra were fitted using line shape accounting of the distribution NMR parameter.^[198] Parameters are presented in Table III.4.

³¹P ($I = \frac{1}{2}$) MAS NMR spectra were acquired using a presaturation (90°-tau) N=20 period followed by a recovery delay of 32 s to ensure quantitiveness of the spectra.

Additionally, ²⁷Al{³¹P} Rotational Echo DOuble Resonance (REDOR) experiments were performed to investigate the Al-P spatial proximities.^[199]

²⁹Si ($I = \frac{1}{2}$) MAS NMR spectra were collected using a recycle delay of 200 s.

The data was processed using an in-house made code.^[198]

2.5 Small Angle X-Ray Scattering

SAXS was acquired under vacuum with a Xeuss 2.0 apparatus (Xenocs), equipped with a Pilatus3 R 1M detector (Dectris). The intensity is plotted against the scattering vector $q = 4\pi \cdot \sin(\theta) \cdot \lambda^{-1}$, with λ as the wavelength (1.542 Å) and 2θ the scattering angle. The sample detector distance was calibrated with tetradecanol and the detector count was normalized by direct beam measurements. Samples were sealed in glass capillaries (diameter 1.5 mm, wall thickness 0.1 mm, WJM-Glas GmbH). Standard procedures were applied to subtract background scattering and to normalize the intensities.^[33]

The lamellar repeat distances were calculated by the position of their 0k0 progression, using $d = 2\pi \cdot q^{-1}$. The displayed q range from 1.0 nm⁻¹ to 16.0 nm⁻¹ was attained with a single sample to detector distance.

The scattering curve of dispersed imogolite was fitted by a core-shell cylinder with a wall thickness of 0.6 nm and an overall diameter of 2.8 nm. The electronic density of water

($\rho_{water} = 0.334 \text{ cm}^{-3}$) was used for the solvent and the internal cavity. For the wall the electronic density was $\rho_{wall} = 0.669 \text{ cm}^{-3}$. Additionally, a flat background was added.

2.6 Scanning Electron Microscopy

The morphology of imogolite after the reaction with DPA was observed by scanning electron microscopy. The dispersed product was deposited on a plasma cleaned Si surface and left to dry. Observations were conducted on a Hitachi SU-70 microscope operated at 5 kV.

2.7 Transmission Electron Microscopy

The morphology of synthesized imogolite was observed with cryogenic transmission electron microscopy. A drop of the solution was deposited on a copper grid covered with a holey carbon film (Quantifoil R2/2) that was previously treated by a plasma glow discharge. Excess of liquid on the grid was blotted out with filter paper and the grid was quickly plunged in liquid ethane to form a thin vitreous ice film. The whole process was performed using a Vitrobot apparatus (FEI Company). Observations were conducted at low temperature (-180°C) on a JEOL 2010 FEG microscope operated at 200 kV. Images were recorded with a Gatan camera. To observe the morphology of the product dispersed in toluene, the dispersion was deposited on the copper grids and left to dry. The same camera and microscope were used at ambient temperature.

2.8 Fluorescence Microscopy

Images were collected on an Olympus IX81 confocal microscope. To stain the phases, fluorescein was added to water and Nile red to the toluene dispersion before emulsification. The excitation wavelength for fluorescein was 488 nm and 543 nm for Nile red.

2.9 Dispersibility, Emulsification and Interfacial Activity

The modified imogolite was dispersed in toluene (CARLO ERBA, 99.8%) directly after the washing steps (dispersion – centrifugation), and without prior drying. Emulsions were formed by mixing the dispersed modified imogolite suspension at $0.5 \text{ g} \cdot \text{L}^{-1}$ with water in a 1:1 volumetric proportion. Droplets of water were deposited on the interface between water and the above mentioned dispersion. The emulsions were observed on an Olympus

IX81 microscope. High purity water ($18.2 \text{ M}\Omega \cdot \text{cm}$) was used to create emulsions and liquid-liquid interfaces.

3 Results and Discussion

3.1 Reaction of Imogolite and Decylphosphonic Acid

Preliminary Characterization of Imogolite

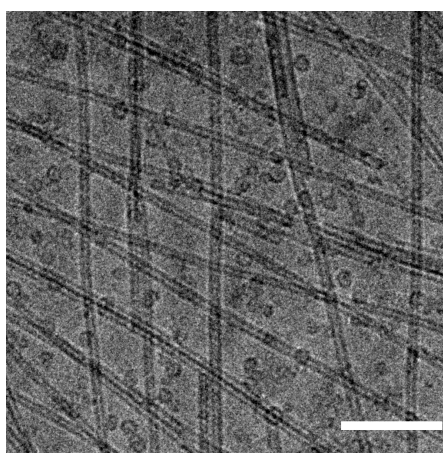


Figure III.4: Cryo-TEM picture of imogolite. Globular structures are allophane and proto-imogolite. Scale bar is 25 nm.

Imogolite was synthesized according to the protocol described in Materials and Methods. Cryo-TEM observations of the obtained aqueous dispersion (Figure III.4) evidence imogolite tubes in coexistence with globular allophane and proto-imogolite. The typical presence of other objects than imogolite reflects in the dampened SAXS curve (Figure III.5) and is in agreement with literature data on imogolite SAXS patterns.^[200–202] Fitting the obtained curve with the scattering pattern of a hollow cylinder gives an outer tube radius of 2.8 nm, which is a typical value for synthetic dispersed imogolite. The reactivity between the suspended particles and DPA is studied for the protocol described in Material and Methods. The products are characterized by IR, SAXS, multinuclear MAS NMR and electron microscopy in order to investigate the evolution with the reaction progress. To identify the occurring transformations, all the prepared samples are systematically compared to pristine imogolite.

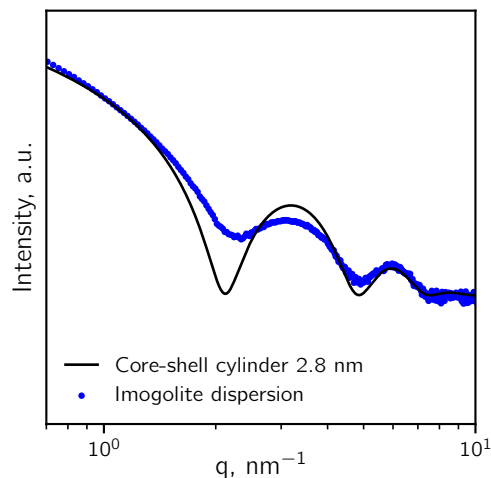


Figure III.5: SAXS pattern of dispersed imogolite and its corresponding fit by a core-shell cylinder, yielding an outer diameter of 2.8 nm.

Infrared Spectroscopy

The IR spectrum of imogolite has three main contributions (Figure III.6). First, the hydroxyl stretching (3510 cm^{-1}) and bending vibrations (1636 cm^{-1}) originating mainly from internal water.^[203] Secondly, the Al-O vibrations at 692 , 596 , 564 , 503 and 426 cm^{-1} , which are characteristic for the imogolite local structure.^[204] Lastly, the doublet appearing at $988\text{ cm}^{-1}/941\text{ cm}^{-1}$, which is related to the asymmetric stretching mode of the isolated SiO_4 tetrahedra and is typical for the tubular shape of imogolite.^[149,157,200,205,206]

After reaction with DPA, all the characteristic regions of imogolite are retrieved in the IR spectra of samples A1 - A5. Only the SiO_4 doublet shifts to 994 cm^{-1} - 992 cm^{-1} / 938 cm^{-1} - 935 cm^{-1} for each of these samples. For sample B, the SiO_4 doublet is not observable, the appearance of the characteristic Al-O region (426 to 692 cm^{-1}) changes, and both the intensity and shape of the hydroxyl bands are different.

Due to the alkyl chain, the infrared spectrum of DPA (Figure III.6) features CH_3 stretching at 2957 and 2873 cm^{-1} , CH_2 stretching at 2921 and 2851 cm^{-1} , CH_2 bending at 1467 and 1404 cm^{-1} , and CH_2 rocking at 718 cm^{-1} .^[207] The broad band centered at 2300 cm^{-1} can be assigned to hydrogen bonding.^[207] The bands from 1130 to 940 cm^{-1} and 530 to 460 cm^{-1} originate mainly from PO vibrations. The region between 1130 and 940 cm^{-1} contains vibrations from PO single and double bonds but the assignment is not unanimous in literature.^[207,208] The peak at 1232 cm^{-1} was assigned to the P=O group.^[209,210]

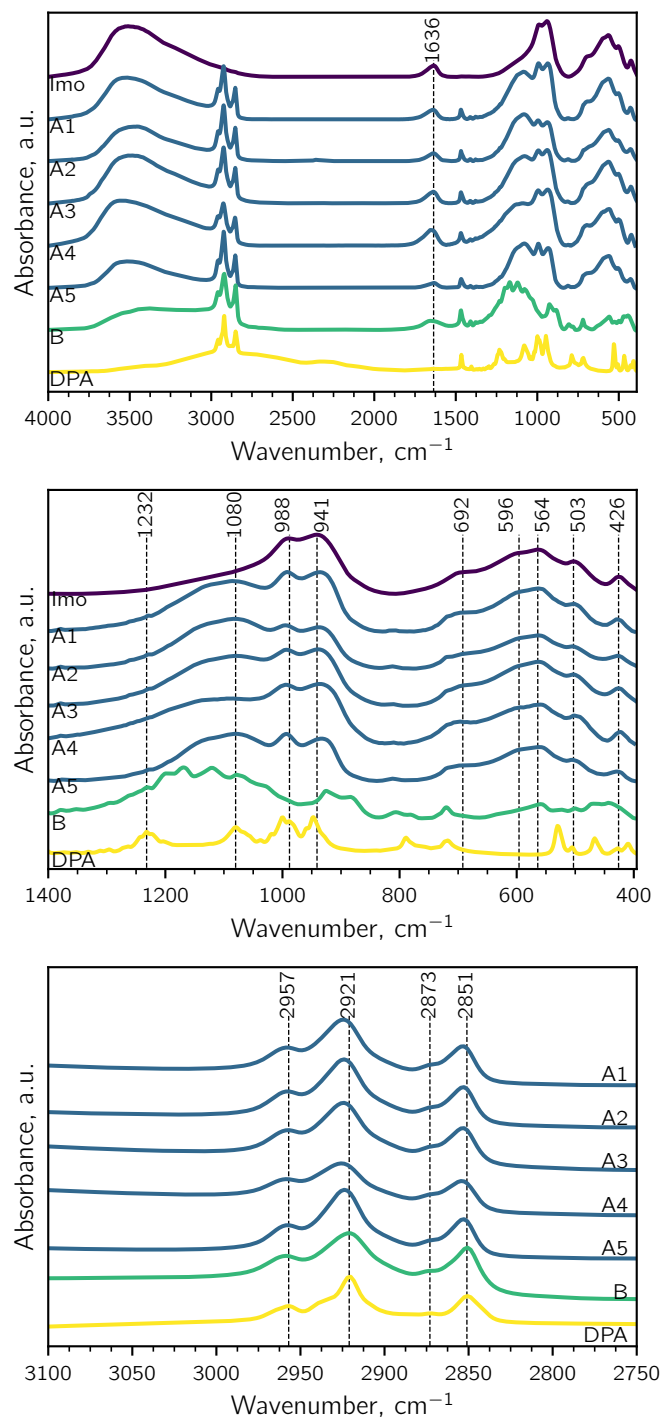


Figure III.6: Top: IR spectra of imogolite, samples A1 – A5, sample B and DPA, normalized to maximum absorbance. **Center:** Zoom from 1400 to 390 cm^{-1} . **Bottom:** Zoom from 3100 to 2750 cm^{-1} .

The appearance of CH_2 and CH_3 vibrations between 2960 cm^{-1} and 2850 cm^{-1} and at 1471 cm^{-1} indicate the presence of alkyl chains in all samples (Figure III.6). Comparing the CH_2 stretching bands of the products to those of DPA reveals no shift for sample B, while a qualitative shift towards higher wavenumbers is observed for samples A1 - A5. This shift of the vibration bands for samples A1 - A5 indicates slightly less ordered chains in contrast to sample B, for which a similar degree of order as in the all-trans DPA is evidenced.^[211]

Furthermore, a shouldered peak appears at 1080 cm^{-1} for samples A1 - A5. The shoulder turns into several sharp bands for sample B. This new contribution indicates the formation of P-O-Al bonds in all samples and therefore a successful reaction between imogolite and DPA. Interestingly, the P=O signal of DPA at 1232 cm^{-1} disappears after reaction. A possible explanation could be a tridentate binding mode in the formed product.^[209,210] In summary, the spectra of samples A1 - A5 show a high content of imogolite and are in good agreement with the findings of Yamamoto et al. for the reaction of ODPA with imogolite, and Bac et al. for the reaction between ODPA and germanium imogolite.^[166,177,179] The spectrum of sample B suggests a rather low amount of residual imogolite due to the modification of the typical hydroxyl, Al-O and Si-O bands. It compares well with the spectrum of ODPA-modified imogolite presented by Picot et al.^[30] The presence of several sharp P-O-Al peaks was also evidenced for aluminum organophosphonates and might indicate the presence of such a phase.^[212] While IR demonstrates that a reaction has occurred between imogolite and DPA, it does not provide sufficient information to assess the integrity of the nanotubes after the reaction.

Magic Angle Spinning Nuclear Magnetic Resonance Spectroscopy

Although MAS NMR is a useful tool for the characterization of imogolite, no NMR study of the reaction between imogolite and phosphonic acids has been reported so far.^[173,213,214] Since no relevant differences were observed between the samples A1 - A5, the NMR investigation was restricted to the unreacted imogolite, sample A1 (short reaction time) and sample B (long reaction time).

The obtained ^{31}P MAS NMR spectra (Figure III.7) show no remaining DPA at 31 ppm for the different products. Sample A1 has a single broad peak from 0 to 35 ppm, while sample B shows pronounced peaks at 2 ppm, 9.5 ppm and 13.5 ppm. The broad peak in sample A1 evidences the formation of P-O-Al bonds with distributed chemical environments. The latter develops into a more ordered structure with prolonged reaction time, as observed for sample B.

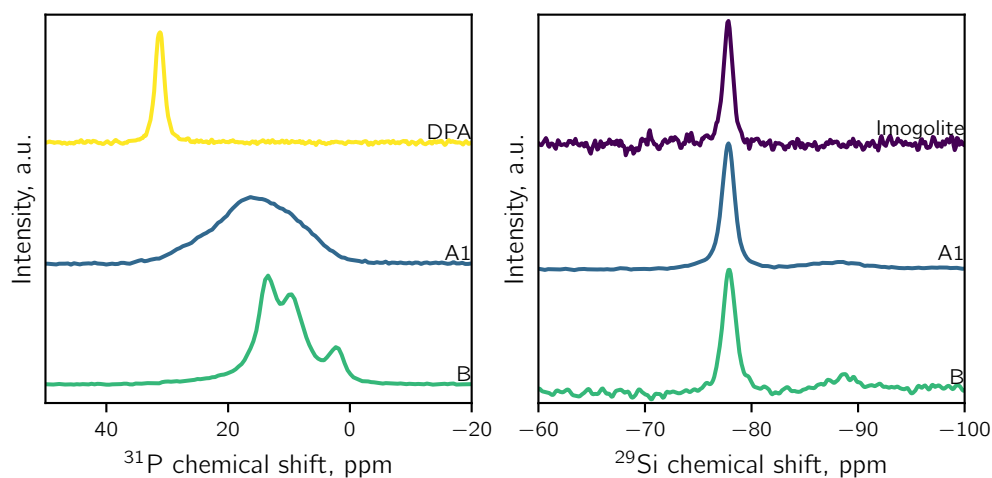


Figure III.7: **Left:** ^{31}P MAS NMR spectra of DPA, sample A1 and sample B. **Right:** ^{29}Si MAS NMR spectra of imogolite, sample A1 and sample B, normalized to highest peak intensity.

In ^{29}Si MAS NMR (Figure III.7), imogolite shows a single narrow peak at -78 ppm assigned to a Q3(6Al) environment.^[213,215] It should be noted, that the peak intensities cannot be compared quantitatively due to experimental parameters. Samples A1 and B show a broad contribution at -88 ppm. The decreased NMR shift indicates a change in the coordination of silicon, either by a defective coordination or by an increase in polymerization of the silicon species.^[214,215] Both indicate the degradation of imogolite through the reaction with decylphosphonic acid.

Pristine imogolite has a single peak at 8 ppm in ^{27}Al MAS NMR (Figure III.8), which is assigned to octahedrally coordinated aluminum and clearly confirms the imogolite local structure.^[213,214] Three peaks are visible in the ^{27}Al MAS NMR spectra for samples A1 and B. The spectra were fitted using lineshape accounting of the distribution NMR parameter (Table III.4).^[198] The peak centers and the corresponding relative areas were obtained by deconvolution of the ^{27}Al MAS NMR spectra (Appendix E). The signals of sample A1 are centered at -5 ppm (24%), 8 ppm (69%) and 47 ppm (7%). The peak at -5 ppm exhibits a noticeable broadness. For sample B, the signals are located at -13 ppm (69%), 8 ppm (28%) and 46 ppm (3%).

By collecting $^{27}\text{Al}\{^{31}\text{P}\}$ REDOR curves (Figure III.8), the spatial proximity of P to Al atoms was probed. The REDOR signal at -5 ppm and 47 ppm in sample A1 rapidly increases with time, suggesting that Al atoms are in close vicinity to P atoms. This is not the case

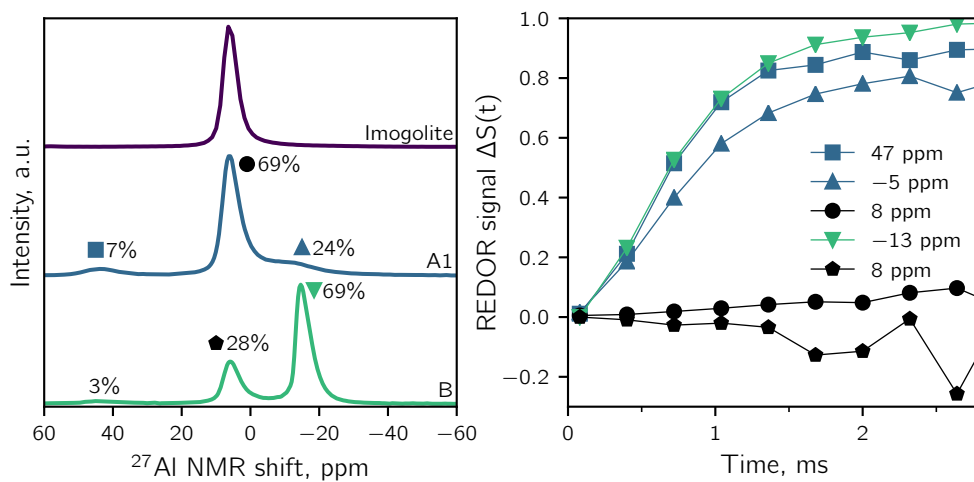


Figure III.8: **Left:** ^{27}Al MAS NMR spectra of imogolite, sample A1 and sample B, normalized to highest peak intensity. **Right:** $^{27}\text{Al}\{^{31}\text{P}\}$ REDOR signals of the sites observed in sample A1 and sample B. Lines between data points are for clarity.

Table III.4: ^{27}Al MAS NMR distribution parameters.

	δ_{iso} , (ppm)	C_Q , (MHz)	fwmh, (ppm)
Sample A1			
AlO_6	8	2.5	7
AlO_6	-5	2.9	24
AlO_4	47	2.9	13
Sample B			
AlO_6	8	2.7	7
AlO_6	-13	2.6	6
AlO_4	46	2.9	13

Uncertainties are $u(\delta_{iso}) = 1$ ppm and $u(C_Q) = 0.2$ MHz.

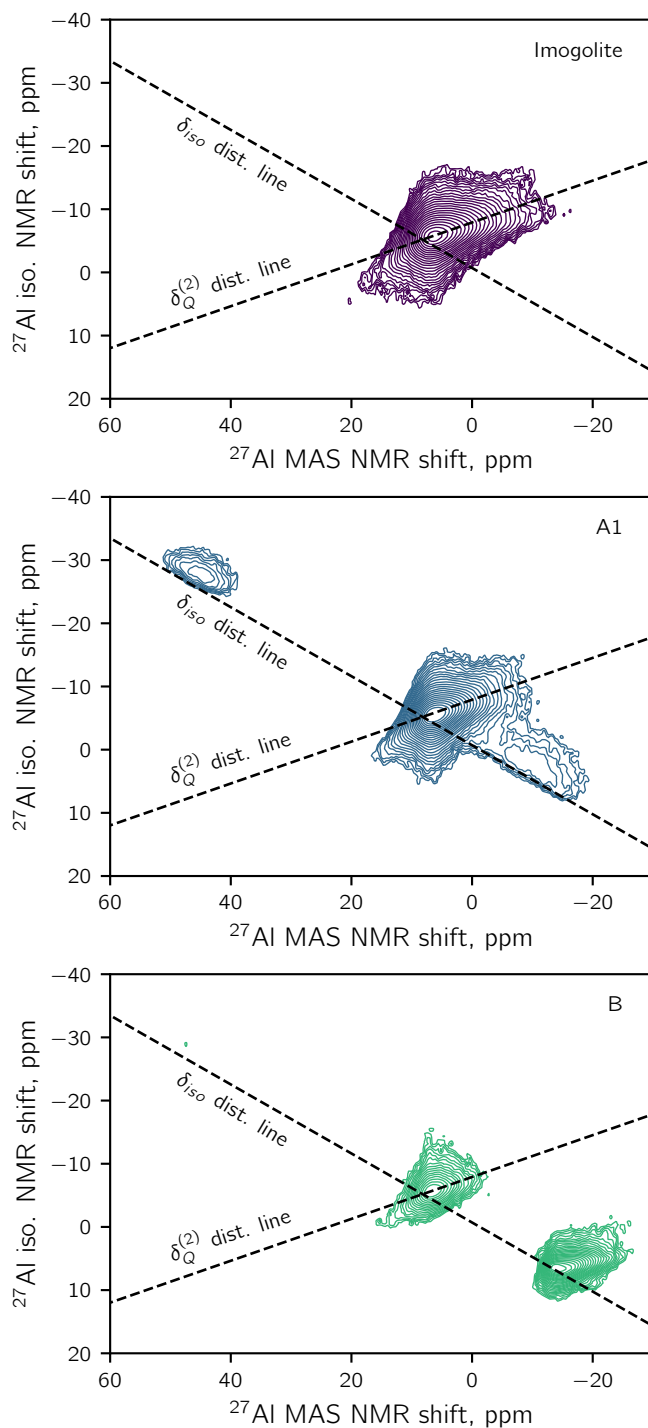


Figure III.9: ^{27}Al MQMAS (triple quantum) spectra. Dashed lines represent the directions of broadening induced by the distribution of isotropic chemical shift (δ_{iso}) and second-order quadrupolar induced shift ($\delta_Q^{(2)}$). **Top:** Imogolite. **Center:** Sample A1. **Bottom:** Sample B.

for the slowly increasing signal at 8 ppm, indicating that this site is able to interact with phosphorous, but does not directly coordinate to it. For sample B, the Al atoms resonating at -13 ppm are close to P atoms, while the 8 ppm peak is not coordinated by P. Low peak intensities made it impossible to collect the data for the signal at 46 ppm and turned the data for the 8 ppm peak noisy.

In ^{27}Al MQMAS NMR (Figure III.9), imogolite shows a NMR shift distribution mainly due to quadrupolar interactions. The MQMAS experiments for samples A1 and B confirm the presence of three sites. For sample A1, the signal at 8 ppm has a similar NMR shift distribution as unmodified imogolite, while the two new peaks at -5 ppm and 47 ppm display mainly a distribution in the isotropic shift (see dashed lines in Figure III.9). This distribution indicates a lower degree of crystallinity in the new environments. For sample B, the signal at -13 ppm has a more pronounced quadrupolar distribution compared to the signal at -5 ppm in sample A1 and is therefore more crystalline.

All samples show a signal at 8 ppm, hinting on the presence of unreacted imogolite tubes. Due to the vicinity of P and Al, the peaks at -5 ppm and -13 ppm can be assigned to AlO_6 octahedra with P in their second coordination shell, while the peaks at 47 ppm and 46 ppm are attributed to Q4(4P) AlO_4 tetrahedra.^[216] Similarly shifted signals were reported for AlO_4 ^[212,217] and AlO_6 ^[218] coordination in aluminum phenylphosphonates. From this result and the previous characterization, it can be concluded that sample B mainly consists of rather crystalline aluminum decylphosphonate. This is supported by the sharp peaks in the ^{31}P spectrum, which were identified as a sign for crystalline aluminum alkylphosphonate.^[194,196,219] Sample A1 still has a high content of imogolite and the new octahedral Al environment is less well defined. Furthermore, the ^{31}P spectrum shows a broad peak, which was identified by Lassiaz et al. as an indicator for a successful grafting reaction on aluminum oxide.^[196,219] However, in the present case, the unresolved ^{31}P peak could also reflect the distributed chemical environments in a not exclusively crystalline phosphonate.

Small Angle X-Ray Scattering

The x-ray scattering pattern of imogolite shows a broad peak at 2.76 nm^{-1} , which is typical for disordered aggregated bundles in the dry powder (Figure III.10). Significant modifications occur after reaction with DPA. For samples A1 - A5, three peaks at 2.26, 4.51 and 6.71 nm^{-1} superimpose the scattering curve of imogolite. Additional peaks are present at higher q values but not clearly visible due to noise. The exact position of these

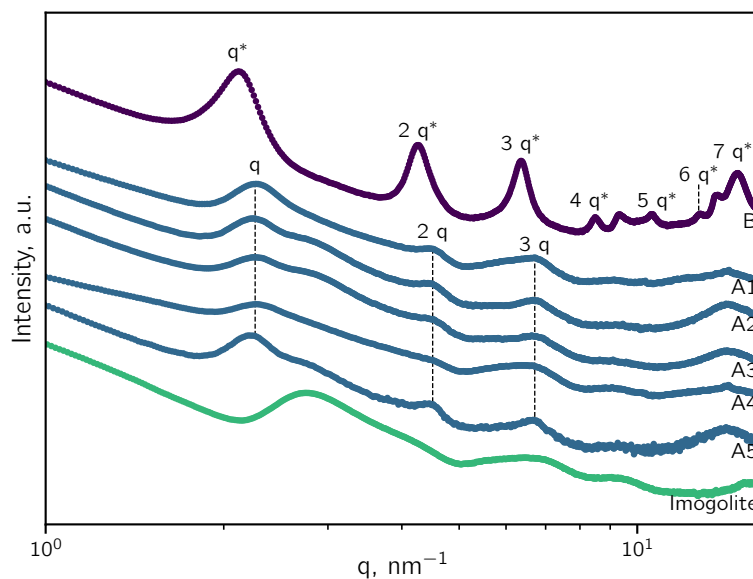


Figure III.10: Powder X-ray scattering patterns of imogolite, samples A1 – A5 and sample B.

reflections vary slightly with the reaction conditions. Sample B shows peaks at 2.11, 4.26, 6.35, 8.49, 9.31, 10.58, 12.73, 13.65 and 14.80 nm^{-1} , while the contribution of imogolite is hardly noticeable. Excluding the peaks at 9.31 nm^{-1} and 13.65 nm^{-1} , all the peaks in sample B are consistent with the 0k0 progression of a lamellar phase. For samples A1 and A4, this is not so evident on the first glance, since the first peak of imogolite bundles seems to shift towards smaller q values. However, the resulting increase in d spacing is not consistent with a DPA grafted tube, since the difference to the radius of an imogolite tube is only 0.6 nm. For sample B, the lamellar peaks are shifted to smaller angles and the reflections are better defined. This effect is consistent with larger lamellar domains and a higher order of organization of the alkyl chain, as observed in IR. The inter-lamellar spacing is 2.8 nm for samples A1 – A5 and 2.9 nm for sample B. It is close to the values reported for lamellar phases obtained with other decylphosphonate metal oxide phases such as aluminium decylphosphate (3 nm), calcium decylphosphate (3.1 nm) and calcium hydroxyapatite modified by decylphosphate (3 nm).^[220–222]

Bac et al. already observed the formation of a lamellar phase following the reaction between germanium imogolite and ODP. ^[179] The reported peak in XRD at 1.65 nm most probably represents the 030 peak of aluminum octadecylphosphonate with a corresponding lamellar repeat distance of 5.0 nm. Picot et al. observed peaks at approximately $q = 1.3, 2.6$ and

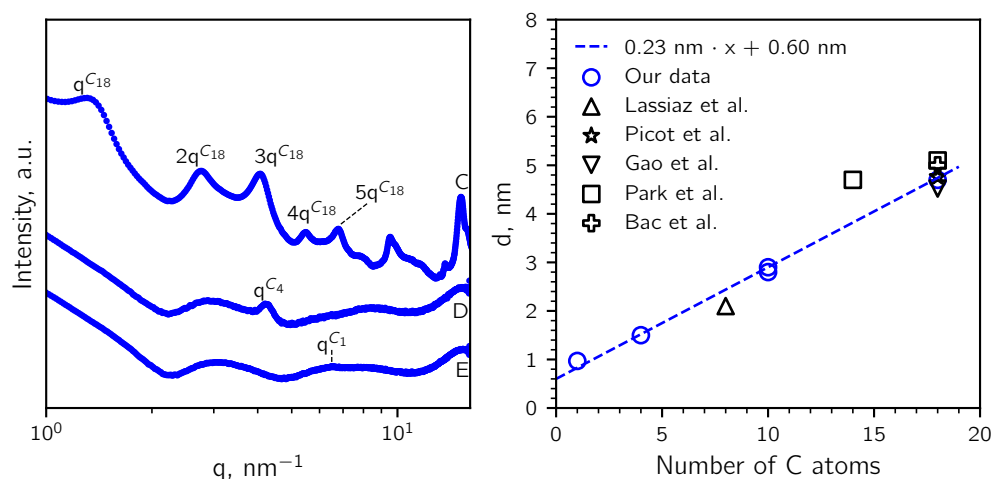


Figure III.11: Left: Scattering patterns of samples C, D and E. Peaks from aluminum alkyl phosphonate are indicated. The scattering patterns of samples D and E were collected from the wet sediment after centrifugation. **Right:** Repeat distance d in relation to the used alkylphosphonic acid chain length in several phosphonate phases by Lassiak et al.,^[196] Picot et al.,^[30] Gao et al.,^[194] Park et al.,^[178] Bac et al.^[179] and the presented data.

3.9 nm^{-1} in SAXS and interpreted them as the k_0 progression of a 2D hexagonal phase.^[30] Calculating the distance for a lamellar $0k_0$ progression from their values yields 4.8 nm , which is consistent with aluminum octadecylphosphonate. Direct comparison with the XRD data of the reaction between ODPa and imogolite reported by Park et al. is difficult, since the used wavelength is not mentioned and the data is noisy.^[178] Nonetheless, the authors present scanning tunneling microscopy pictures where they observe a pattern with a repeat distance of 5.1 nm for ODPa and 4.7 nm for TDPA after reaction with imogolite. These distances correlate to the chain length of the used phosphonic acid, but the presence of imogolite tubes in the structure is not unambiguously proven. The d spacings of all these compounds appear to increase linearly with the carbon number of the alkylphosphonic acid (Figure III.11). This indicates that the length of the alkyl chain is the main factor influencing the thickness, regardless of the nature of the inorganic part. Even for short chained phosphonates, the trend holds true. The only deviation is observed with the microscopy data reported by Park et al. for TDPA. The variation in d spacing for the reported octadecylphosphonates could be associated to different crystal structures, as reported for phenylphosphonates. For aluminum phenylphosphonate, the structure indeed depends on the synthesis condition.^[217] From SAXS, it can be concluded that the reaction of imogolite with alkylphosphonic acid

yields a lamellar phase for all experimental conditions (Table III.3) and that no evidence of grafted imogolite is observed.

Scanning Electron Microscopy and Transmission Electron Microscopy

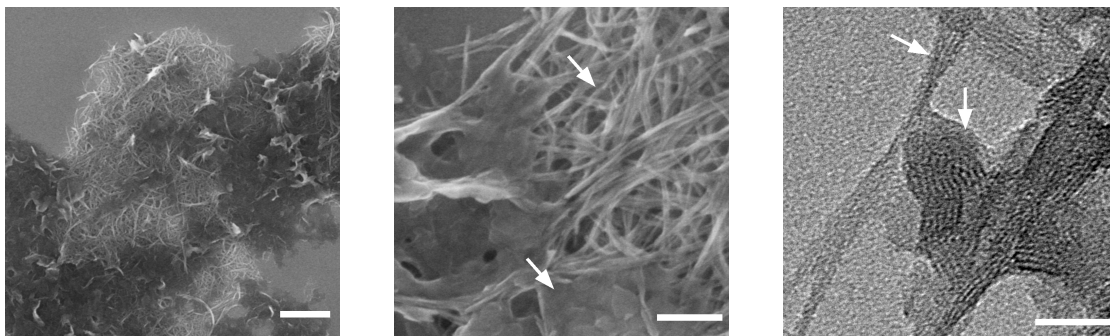


Figure III.12: **Left and center:** SEM image of sample A5. **Right:** TEM image of sample A5. At least two interconnected phases are visible, as pointed out by the arrows: elongated bundles of aggregated imogolite and plate-like objects with a lamellar structuration. Scale bars are 5 μm (left), 100 nm (center) and 25 nm (right).

SEM of sample A5 (Figure III.12) shows aggregates with zones of needle-shape and platelet-like morphologies. Both types of morphologies are connected. These aggregates appear as dark domains in TEM (Figure III.12). In their periphery, assemblies of aggregated nanotubes are visible. In between the network of imogolite bundles, small domains are present. Depending on their orientation in space, the aggregates show a lamellar organization. No structures hinting on grafted imogolite were observed, i.e. imogolite surrounded by a corona of DPA.

Degradation versus Surface Modification

The obtained results challenge the commonly used scheme of grafted imogolite, where the phosphonic acid reacts with OH groups on the external wall of imogolite and forms covalent bonds by condensation. [179,180,182,183] IR, ^{31}P MAS NMR and ^{27}Al ^{31}P REDOR experiments give evidence for the formation of P–O–Al bonds. However, the chemical shift observed in ^{27}Al MAS NMR and the SAXS results underline the formation of a lamellar aluminum decylphosphonate structure. SEM and TEM support these findings by showing a mixture of lamellar phase and imogolite tube bundles interconnected with each other.

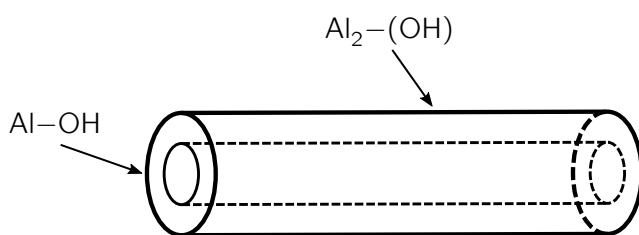


Figure III.13: Schematic representation of an imogolite tube. Arrows indicate the positions of bridging $\text{Al}_2(\text{OH})$ groups that cover the tube wall and $\text{Al}-\text{OH}$ (and $\text{Al}-\text{OH}_2^+$) groups on the terminal points.

Overall, the results do not support a grafting reaction of DPA on imogolite, but give evidence for the formation of a composite material.

The basis for this reactivity is the surface chemistry of imogolite, which is similar to gibbsite. Bridging $\text{Al}_2(\text{OH})$ groups that correspond to the crystal face of gibbsite cover the tube wall, while the terminal points have $\text{Al}-\text{OH}$ and $\text{Al}-\text{OH}_2^+$ groups, similar to the crystal edges of gibbsite (Figure III.13). The difference between those two sites is their affinity to participate in adsorption. The single coordinated hydroxyls are active, while the bridging hydroxyls are inert for adsorption processes at low adsorbate concentrations.^[223,224] For phosphate, gibbsite starts to form aluminum phosphate phases at acidic pH that deposit on the faces of gibbsite.^[225] It was suggested that the complexation of the gibbsite edge is an intermediate in this process.^[225-227] Based on the structural similarity of metal phosphates and phosphonates,^[228] a similar reactivity is presumed for the sorption process of phosphonic acid on imogolite as for phosphate on gibbsite. At the studied conditions DPA does not adsorb or react with the bridging $\text{Al}_2(\text{OH})$ groups of imogolite. It mainly complexes $\text{Al}-\text{OH}$ and $\text{Al}-\text{OH}_2^+$ groups and degrades imogolite tubes by forming lamellar aluminum decylphosphonate. Since those groups are mainly present at the terminal points of the tubes, the degradation is slow and it explains the high amount of residual tubes evidenced for samples A1 - A5.

Another aspect that potentially governs the observed reactivity in the sample is the presence of allophane and proto-imogolite. They share the same local structure as imogolite, but the ratio between $\text{Al}-\text{OH}$ and $\text{Al}_2(\text{OH})$ is different.^[200] Due to their higher relative amount of $\text{Al}-\text{OH}$, they should be more reactive. To observe pure imogolite reactivity proto-imogolite and allophane need to be removed. A process to purify imogolite samples is presented in the next chapter. Although proto-imogolite and allophane are present in the studied sample, the respective mass was relatively low and should not influence the final result.

3.2 Dispersibility, Emulsification and Interfacial Activity

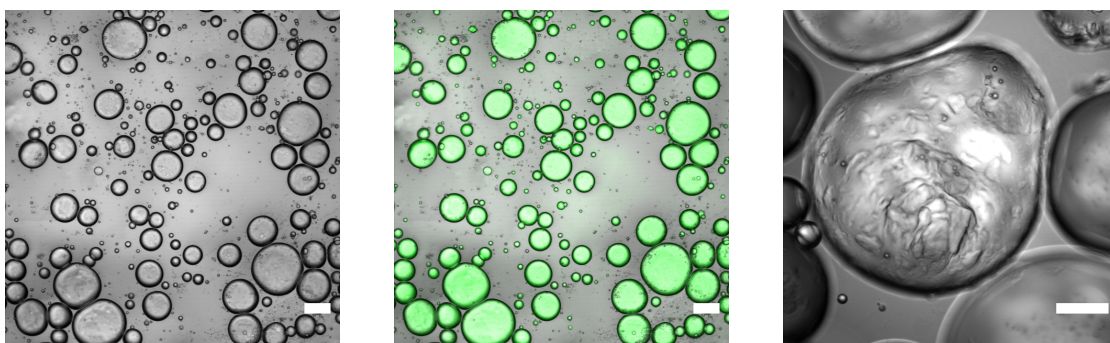


Figure III.14: Water-in-oil emulsion stabilized by sample A5 in toluene. The aqueous phase is stained with fluorescein in the center image. Scale bars are 50 μm .

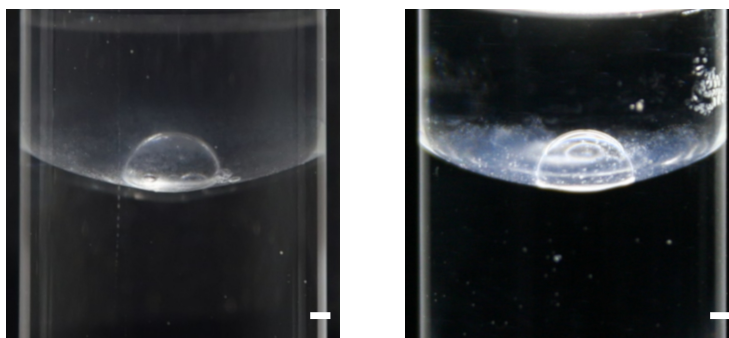


Figure III.15: **Left:** A 20 μL water droplet stabilized by modified imogolite at the toluene/water interface. **Right:** The same stabilized droplet, illuminated from below. Scale bars are 1 mm.

In the majority of the published studies the dispersibility of modified imogolite was taken as a proof for the successful surface modification of imogolite by phosphonic acid. [30,178,179,182] Although our results give no hint for surface modified imogolite tubes, the DPA modified imogolite is dispersible in toluene. It gives an almost clear liquid, which is slightly scattering light. Mixing this dispersion with water stabilizes a water-in-oil emulsion (Figure III.14). In contrast, bare imogolite gives an oil-in-water emulsion, as was already observed for hexane. [30] With the composite material, the droplets do not coalesce and can undergo deformations. This is also observed at the macroscopic scale, where an interface between the dispersed composite material and water is able to stabilize large aqueous droplets against coalescence (Figure III.15). This very specific behavior is related to the DPA modified imogolite and cannot be obtained with the interface between toluene and a bare imogolite

dispersion. The ability to stabilize develops with contact time between the two phases and is generally not instantaneously present, i.e. the droplet was only stabilized after 30 min of preceding contact time. The droplets are stable up to one year (experimental time), but collapse if the toluene evaporates. Illumination of the sample unveils the otherwise almost invisible surface precipitate (Figure III.15), that forms after the contact between the dispersion and water, but does not exist in the toluene dispersion itself. The stabilized droplets can also be moved on the interface (see Supporting Information of Lange et al.^[143]). Thus, characteristics of “liquid marbles” for an oil/water system were retrieved. Liquid marbles are defined for air/liquid systems as stabilized liquid droplets covered with hydrophobic particles. Thanks to the nanoparticles, the droplets are able to maintain their shapes even after deformation by external forces.^[229–231]

The droplet stabilization capabilities of this material were used to probe ion transport properties across a droplet-oil-water interface (Appendix F). The investigations were however stopped after it was evident that the tubes are destroyed during the reaction with DPA.

Up to now, the dispersibility of alkylphosphonic acid modified imogolite in organic solvents was explained by a successful grafting reaction, and the resulting grafted imogolite was sketched as a tube with a brush-like corona of grafting agent.^[30,178–181] The difference in hydrophilicity between the internal and the external surfaces of such a grafted tube was used to explain the formation of Pickering emulsions by ODPMA modified imogolite.^[30] However, the structure of dried modified imogolite (Figure III.12) suggests that the mode of stabilization has to be different.

Presuming similar structures of dispersed and dried state (Figure III.12), the imogolite-lamellar phase network would exhibit zones where either hydrophobic (lamellar phase) or hydrophilic areas (residual imogolite) dominate. While the hydrophobic areas promote the dispersion in toluene, the hydrophilic areas and the nanostructuring of the composite material could be responsible for its surface activity at the toluene/water interface. Further investigations are necessary to elucidate the real stabilization mechanism for this system.

4 Conclusion and Perspective

The full characterization of the reaction product from imogolite and DPA gave evidence that imogolite is consumed during the reaction and is not surface modified by DPA. A lamellar aluminum decylphosphonate is created and forms a composite material with unmodified imogolite tubes. The observed reactivity can be explained by an inert $\text{Al}_2(\text{OH})$ surface

and reactive Al–OH groups at the tube ends of imogolite. The produced material showed interfacial activity, a property that was previously ascribed to surface modified imogolite tubes. Since the material is rather complex and the stabilization mechanism is not well understood, it is not used to study transport and reactivity. Nonetheless, the idea of stabilizing Pickering emulsion droplets by imogolite should be further pursued, since it might give the experimental insights into the transport properties of imogolite nanotubes.

The lack of surface modification due to the presumably low reactivity of the Al₂(OH) groups also challenges the covalent surface modification of imogolite in general. It might be necessary to re-visit already known approaches or to develop new ones. Future studies should pay special attention to collect proof of successfully modified and individually dispersed tubes. These studies should also use the actual surface chemistry of imogolite to communicate the imagined reactivity in the presented sketches.

IV Advances for the Surface Modification of Imogolite

1 Introduction

The surface modification of imogolite by post-synthesis methods is a field that is believed to be mastered by the use of silane, phosphate and phosphonate chemistry.^[232,233] However, an isolated surface modified imogolite tube has never been directly evidenced. Furthermore, the results of the previous chapter strongly question the interpretations regarding the reported compatibility of phosphonate chemistry and imogolite in literature. The phosphonic acid moiety was shown to destroy the imogolite structure and to form a composite material from aluminum phosphonate and residual imogolite tubes.^[143] Another crux is the widespread use of some form of aggregated imogolite in the modification protocol (Table III.1), which prevents individual modification of imogolite tubes. The previous chapter also presented some thoughts on the reactivity of imogolite in respect to its surface chemistry. Under the presumption of validity, it implicates that a similar reactivity should be observed for proto-imogolite and allophane. For both, the ratio between single coordinated Al–OH over bridging Al₂(OH) is higher compared to imogolite. Thus, their reactivity should be higher and their presence can influence the observations that are made by X-ray scattering and spectroscopic methods. Therefore, there are three tasks that need to be taken care of to advance in the field of imogolite surface modification.

First, other solvents that can be used to perfectly disperse imogolite without aggregation have to be identified. Such solvents will increase the potential chemistry that is applicable to dispersed imogolite, since as for now it is constricted to water. Thus, a small survey on common polar aprotic solvents will be presented.

Second, imogolite has to be separated from proto-imogolite and allophane without tube aggregation. Conventional methods aggregate the tubes by flocculating them with salt or pH change and by consecutive centrifugation. To achieve better separation, dialysis will be

studied, which is frequently used for the isolation and purification of proteins.

Third, the exploration of viable approaches to yield isolated modified tubes by surface modification on the presumably weakly reactive imogolite surface without perturbing the structure have to be explored. An approach that was shown to adhere to different surfaces is polydopamine coating.^[234,235] It is inspired from mussels, that excrete a protein to adhere to wet surfaces.^[236] Dopamine was found to have the necessary functional groups to mimic the mussel protein and was shown to coat even PTFE.^[234] In general, the substrate is introduced into a solution of dopamine (Figure IV.1) at basic pH. Dissolved oxygen initiates the oxidation and a polymeric layer forms on the substrate. However, neither the polymer structure, nor the binding modes are fully understood.^[234,235,237] Apart from flat surfaces and macroscopic objects it was also used for the coating of magnetite^[238,239] and gold^[240–242] nanoparticles. To obtain a hydrophobic surface the use of a dopamine derivative is necessary, since the formed polydopamine shell is hydrophilic. Another strategy could be to utilize the reactivity of free functional groups on the surface of polydopamine, e.g. amino or hydroxyl groups, to graft other molecules onto the polydopamine layer. However,

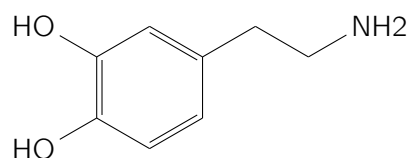


Figure IV.1: Skeletal formula of dopamine.

for imogolite there is also another challenge. The reaction is typically performed at basic pH at which imogolite would aggregate and form tube bundles. At acidic pH, at which imogolite stays dispersed, dopamine does not polymerize under conventional conditions. Alternatively, there are several approaches that use an additional oxidant^[235] or UV light to polymerize dopamine.^[243] The polymerization of dopamine by UV light can also be performed at acidic pH and is based on the generation of reactive oxygen species from oxygen and water. To avoid the use of additional oxidants the UV polymerization of dopamine will be studied regarding the surface coating of suspended imogolite tubes.

2 Materials and Methods

2.1 Synthesis of Imogolite

Imogolite synthesis was performed as described in the previous chapter.

2.2 Dispersion Tests

Acetone, acetonitrile, ethylacetate, dimethylformamide, dimethylsulfoxide, propylene carbonate and tetrahydrofuran were purchased from Sigma-Aldrich and used as received.

2.3 Dialysis

Dialysis membranes with a molecular weight cut-off (MWCO) of 8 and 100 kDa were purchased from Spectrumlabs. The membranes were soaked in deionized water for at least 30 min and rinsed before use. After filling them with the imogolite dispersion, they were closed with clips and immersed into deionized water. The water was changed after 24 h for five days.

2.4 Polymerization of Dopamine

Acetic acid, sodium acetate and dopamine hydrochloride were purchased from Sigma-Aldrich and used as received.

Imogolite dispersions in 0.1 M acetate buffer with a pH of 5 were prepared by weighing out the appropriate mass of sodium acetate and acetic acid, dissolving them in deionized water in a volumetric flask, adding the appropriate amount of imogolite dispersion and filling the flask to the mark with deionized water.

Dopamine solutions were freshly prepared by weighing out the appropriate mass of dopamine, dissolving it in a volumetric flask with the respective solution and filling the flask to the mark. The solutions were transferred to capped beakers and protected from ambient UV light.

Polymerization was initiated by a UV lamp (LC8-L9588-01A, Hamamatsu), equipped with a direct beam uniform illumination unit and no filters (Figure IV.2). Since no filter was available the emitted wavelengths are distributed from 290 to 450 nm. The sample was stirred at 23 cm from the lamp head. A fixed sample volume of 20 mL was used to yield a reproducible liquid column of 3.5 cm. The power of the lamp was measured with a power meter (Nova II, Ophir Optronics) and is plotted in Figure IV.3. Afterwards, the samples were dialyzed with 8 kDa membranes (SpectrumLabs) against deionized water for four days. The water was exchanged every 24 h.

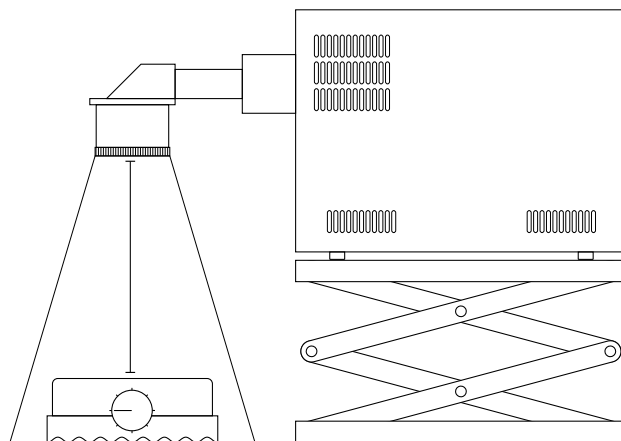


Figure IV.2: Experimental set-up for the polymerization of dopamine. The sample is placed on a magnetic stirring plate and illuminated at a fixed distance by the UV lamp.

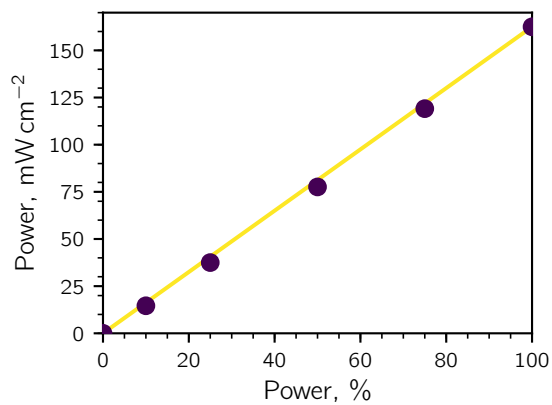


Figure IV.3: Measured lamp power at a distance of 23 cm

2.5 Characterization

UV-Visible Spectroscopy

UV-Vis emission spectra were collected on a Shimadzu UV-2550. The spectra were background and baseline corrected. To acquire the polymerization kinetics, the sample was irradiated for 10 min before a 3 mL aliquot was used for UV-Vis spectroscopy in a quartz cuvette with 1 cm path length. After the spectrum was acquired, the aliquot was reunited with the remaining solution and the process was repeated.

Thermo Gravimetric Analysis

TGA measurements were performed on TGA/DSC 1 analyzer (Mettler-Toledo). Analysis was made in aluminum oxide crucibles under a flow of $50 \text{ mL} \cdot \text{min}^{-1}$ of O_2 with an empty crucible as the reference. The sample was heated from 25°C to 100°C at a rate of $20^\circ\text{C} \cdot \text{min}^{-1}$, held at 100°C for 10 min to remove all adsorbed water from imogolite and heated again with $20^\circ\text{C} \cdot \text{min}^{-1}$ to 1000°C .

Small Angle X-ray Scattering

SAXS was acquired under vacuum with a Xeuss 2.0 apparatus (Xenocs) equipped with a Pilatus3 R 1M detector (Dectris). The intensity is plotted against the scattering vector $q = 4\pi \cdot \sin(\theta) \cdot \lambda^{-1}$, with λ as the wavelength (1.542 \AA) and 2θ as the scattering angle. The sample detector distance can be adjusted (used distances were 42.3, 53.7 and 119.4 cm) and was calibrated with tetradecanol. The detector count was normalized by the direct beam and the calibration was verified with Lupolen. Standard procedures were applied to subtract background scattering and to normalize the intensities.^[33] Samples were sealed in glass capillaries (diameter 1.5 mm, wall thickness 0.1 mm, WJM-Glas) or in Kapon capillaries (diameter 1.506 mm, wall thickness $41.9 \mu\text{m}$, MicroLumen).

Dry samples were measured between two layers of sticky Kapton that were separated by a flat washer. Samples were prepared by dissolving $5 \text{ g} \cdot \text{L}^{-1}$ trehalose (Sigma-Aldrich) in the sample solution, followed by freeze-drying.

Atomic Force Microscopy

Atomic force microscopy (AFM) measurements were carried out using a Bruker Nano Dimension 3000 AFM equipped with a Nanoscope V controller in tapping mode using NanoWorld ARROW-NCR silicon cantilevers. Samples were deposited on freshly cleaved mica substrate by consecutively dipping the mica sheet into the sample solution and three times in fresh deionized water. The specimens were left to dry before analysis. Images were treated with Gwyddion.^[244]

Transmission Electron Microscopy

Transmission electron Microscopy (TEM) was performed on a Philips CM12 electron microscope operated at 80 kV. A drop of the solution was deposited on a carbon film covered copper grid (Agar Scientific). The excess liquid was blotted off with filter paper after a few seconds.

Cryo-TEM observations were conducted at low temperature (-180°C) on a JEOL 2010 FEG microscope operated at 200 kV. Images were recorded with a Gatan camera. A drop of the solution was deposited on a copper grid covered with a holey carbon film (Quantifoil R2/2) that was previously treated by a plasma glow discharge. Excess of liquid on the grid was blotted out with filter paper and the grid was quickly plunged in liquid ethane to form a thin vitreous ice film. The whole process was performed using a Vitrobot apparatus (FEI Company).

3 Results and Discussion

3.1 Dispersion Tests

To access chemistry that is not limited to water as solvent, several polar aprotic solvents were tested by mixing an aqueous $5\text{ g} \cdot \text{L}^{-1}$ imogolite dispersion in a 1:1 ratio. Acetone, acetonitrile, ethylacetate and tetrahydrofuran yielded a precipitate of imogolite tube bundles.

Propylene carbonate yielded, as expected, two phases for a 1:1 (v/v) ratio.^[245] By increasing the propylene carbonate to water ratio, the volume of the water-rich phase decreased by dissolution until a single phase was achieved for a solvent ratio of 10:1. Imogolite

instantaneously precipitated on the wall of the glass sample vial as soon as no water phase was present anymore. Figure IV.4 shows samples at different solvent ratios that are between crossed polarizers. The sample with a 2:1 ratio has an isotropic water-rich and propylene carbonate-rich phase. For a solvent ratio of 4:1 and 6:1, the water-rich phase shows birefringence, indicating the presence of a liquid crystal. For the 10:1 sample, only one phase is visible and imogolite precipitates. It is visible as small bright dots on the wall of the glass vial. Although imogolite is not dispersible in the propylene carbonate-rich phase, propylene carbonate might still be useful to concentrate imogolite in the water-rich phase. At 25 °C the water rich phase contains approximately 17.5 % of propylene carbonate by weight. [245]

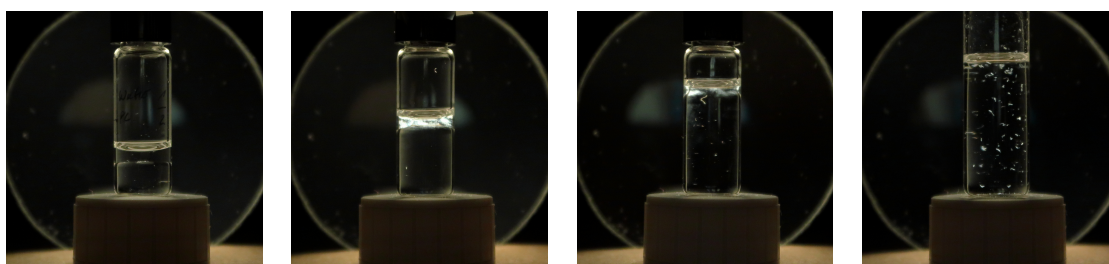


Figure IV.4: From left to right: 2:1, 4:1, 6:1 and 10:1 (v/v) solvent ratios for propylene carbonate and the aqueous dispersion of imogolite. Samples are between crossed polarizers.

Dimethylformamide (DMF) and dimethylsulfoxide (DMSO) yielded a single phase that both show flow birefringence. By rotary evaporation under reduced pressure, the water content of the two phases was reduced without any sign of imogolite tube aggregation. By repeatedly adding aqueous imogolite dispersion and evaporating water, the imogolite concentration of the DMF and DMSO dispersion were increased. At elevated imogolite concentrations, some imogolite remained on the glassware during evaporation, but was easily removed from the remaining dispersion. The concentrated dispersions show different birefringence patterns (Figure IV.5), indicating the presence of different liquid crystalline phases. [246,247] SAXS evidences different scattering patterns (Figure IV.6) for an increasing imogolite concentration. The sample containing $\approx 5 \text{ g} \cdot \text{L}^{-1}$ shows the typical imogolite scattering curve and the first minimum due to the tubular shape of the particles. For ($\approx 10 \text{ g} \cdot \text{L}^{-1}$) two bumps are visible at 0.20 and 0.40 nm^{-1} , which indicate the presence of a nematic phase. The imogolite tubes have no positional order and are loosely oriented along a common direction, giving rise to the observed bumps that are indicative for the tube-tube distance. These bumps develop into peaks for a concentration of $\approx 25 \text{ g} \cdot \text{L}^{-1}$.

These peaks are at 0.37, 0.64, 0.74 and 0.98 nm⁻¹. The relative ratio of these positions is 1 : $\sqrt{3}$: 2 : $\sqrt{7}$, which indicates the presence of a hexagonal packed structure, typical for a columnar phase. In the columnar phase, the particles are oriented in one direction and have a long range positional order in the plane perpendicular to the orientation axis. Due to the high X-ray absorption of DMSO ($\mu = 45.6 \text{ cm}^{-1}$ for $\lambda = 1.542 \text{ \AA}$) no scattering signal could be collected from the DMSO dispersions. It has to be noted that rotary evaporation is not able to completely remove all the water, especially since the tubes are filled by water, which may, or may not leave the tube. The water content has not been quantified.

DMSO and DMF will open new possibilities to use imogolite and give access to a richer chemistry. In particular, the solvents could be used for silanization procedures with dispersed imogolite tubes in a non-aqueous environment without tube aggregation.^[169–173]

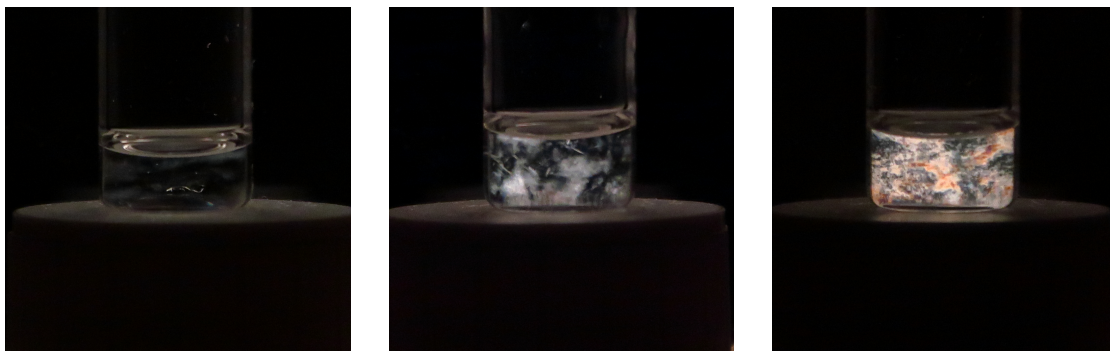
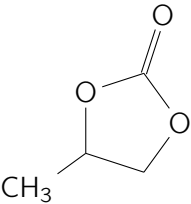
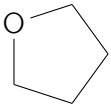


Figure IV.5: Dispersed imogolite at different concentrations. **Left:** $\approx 5 \text{ g} \cdot \text{L}^{-1}$. **Center:** $\approx 10 \text{ g} \cdot \text{L}^{-1}$. **Right:** $\approx 25 \text{ g} \cdot \text{L}^{-1}$.

3.2 Dialysis

To reduce the content of proto-imogolite and allophane in imogolite dispersions, those side products have to be removed after imogolite synthesis. Dialysis is a well established technique to separate different size fractions of large molecules, e.g. proteins or polymers, and has already been employed for imogolite to remove salt contamination.^[202] The chosen MCWO was however not enough to remove Allophane and proto-imogolite. Allophane has a structural molecular weight of approximately 55 kDa.^[248] Thus, a membrane with a MWCO of 100 kDa is tested. To obtain an idea of the tube size fraction that will be lost through dialysis, the molecular mass of a imogolite tube can be approximated by the number of formula units along one circumference and the repeat distance of this circumference (0.42 nm^[149]). Synthetic imogolite has approximately 14 formula units per circumference,

Table IV.1: Dispersion behavior of an aqueous imogolite dispersion in different polar aprotic solvents.

Solvent	Structural formula	Behavior
Acetone	$\begin{array}{c} \text{O} \\ \parallel \\ \text{H}_3\text{C}-\text{C}-\text{CH}_3 \end{array}$	aggregation
Acetonitrile	$\text{H}_3\text{C}-\text{C}\equiv\text{N}$	aggregation
Ethylacetate	$\begin{array}{c} \text{O} \\ \parallel \\ \text{H}_3\text{C}-\text{C}-\text{O}-\text{CH}_2-\text{CH}_3 \end{array}$	aggregation
Dimethylformamide	$\begin{array}{c} \text{O} \\ \parallel \\ \text{H}-\text{C}-\text{N}(\text{CH}_3)_2 \end{array}$	dispersion
Dimethylsulfoxide	$\begin{array}{c} \text{O} \\ \parallel \\ \text{H}_3\text{C}-\text{S}-\text{CH}_3 \end{array}$	dispersion
Propylene carbonate		phase separation
Tetrahydrofurane		aggregation

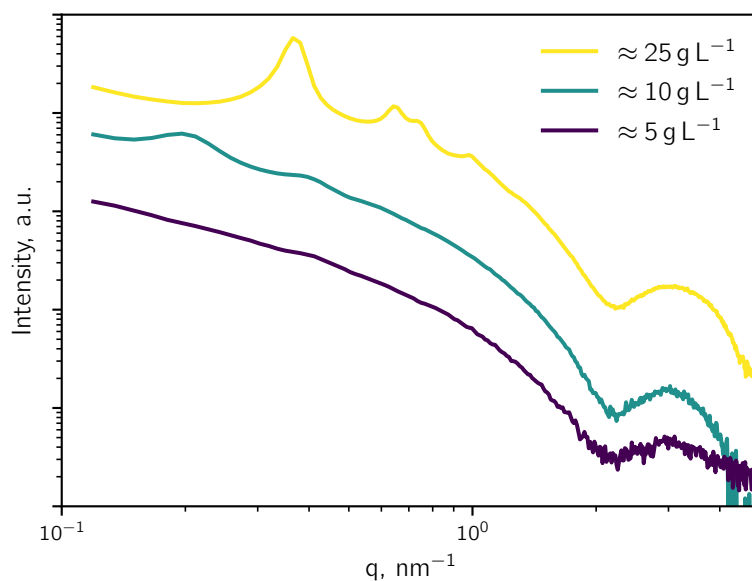


Figure IV.6: SAXS patterns of imogolite dispersed in DMF at different concentrations. Curves are displaced for clarity.

giving a molecular weight of $2773 \text{ g} \cdot \text{mol}^{-1}$ per ring. Consequently tubes that are smaller than 15 nm may be lost for a MWCO of 100 kDa.

After dialysis, the samples are analyzed by SAXS and TEM. The SAXS patterns (Figure IV.7) show that the scattering for the dialyzed samples is overall lower and that the first minimum is more pronounced. Due to the loss of scattering objects and the dilution by osmotic pressure during dialysis, the scattering intensity is reduced. Furthermore, the background scattering caused by small objects is decreased, which makes the scattering of the remaining tubes better observable in the dialyzed samples.

In cryo-TEM (Figure IV.8) the loss of proto-imogolite can be observed as the absence of small undefined objects that are present in the 8 kDa sample. Apart from imogolite (long objects), allophane (small round objects) is still present in the 100 kDa sample. Similar observations are made by AFM (Figure IV.9). The sample that was dialysed with a 8 kDa membrane shows many small objects that are not present in the sample that was dialysed with a 100 kDa membrane.

Allophane and proto-imogolite are typical for the synthesis of Si-imogolite. Although these side products are not dominant in mass, they dominate in number. Due to their high ratio of single coordinated Al–OH groups, their presence might influence the observed reactivity of

the whole sample. Thus they have to be removed to understand the reactivity of imogolite alone. Dialysis with a 100 kDa MWCO is a suitable method to remove proto-imogolite but not allophane. If it is possible to remove allophane by higher MWCO membranes remains to be seen. Nonetheless, removing proto-imogolite by dialysis will be a useful tool for future investigations.

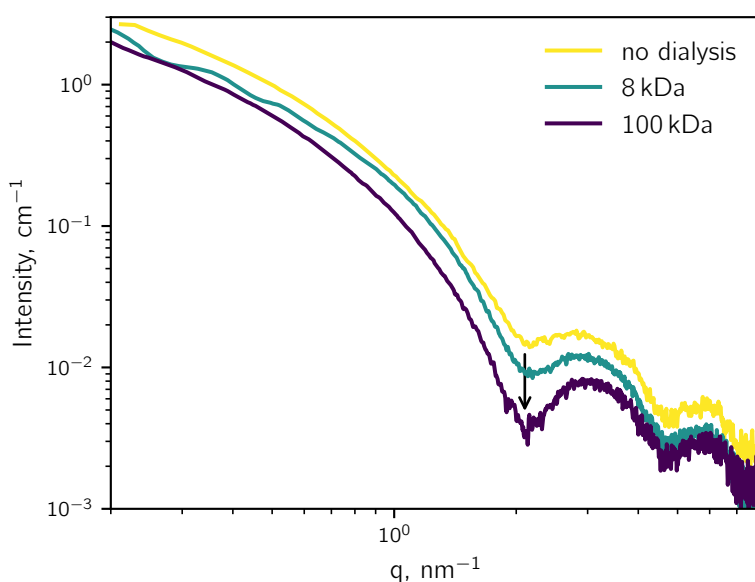


Figure IV.7: SAXS patterns of imogolite dispersions that have been dialyzed with different molecular weight cut-offs.

3.3 Polymerization of Dopamine

Macroscopic Observations and UV-Visible Absorbance

Dopamine solutions ($2 \text{ g} \cdot \text{L}^{-1}$) were transparent and turned orange-brown after 1 h of UV irradiation at $162.5 \text{ mW} \cdot \text{cm}^{-2}$. The pH changed from ≈ 6 to ≈ 4 after irradiation. Both color and pH did not change significantly after one more hour of irradiation. Consequently, solutions were prepared in a pH 5 acetate buffer, which yielded dark brown solutions after irradiation.

To study the evolution of the reaction a dopamine solution ($2 \text{ g} \cdot \text{L}^{-1}$ dopamine in 0.1 M acetate buffer) was irradiated for a total of 2 h and a UV-Vis absorbance spectrum was collected every 10 min. The same procedure was repeated for a mixture that additionally

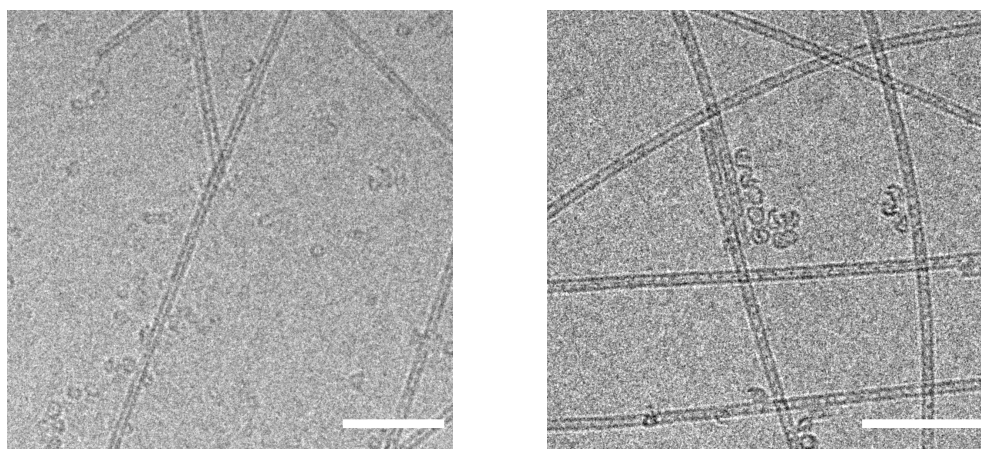


Figure IV.8: Left: Cryo-TEM after dialysis with a 8 kDa MWCO membrane. **Right:** Cryo-TEM after dialysis with 100 kDa MWCO membrane. Scale bars are 25 nm.

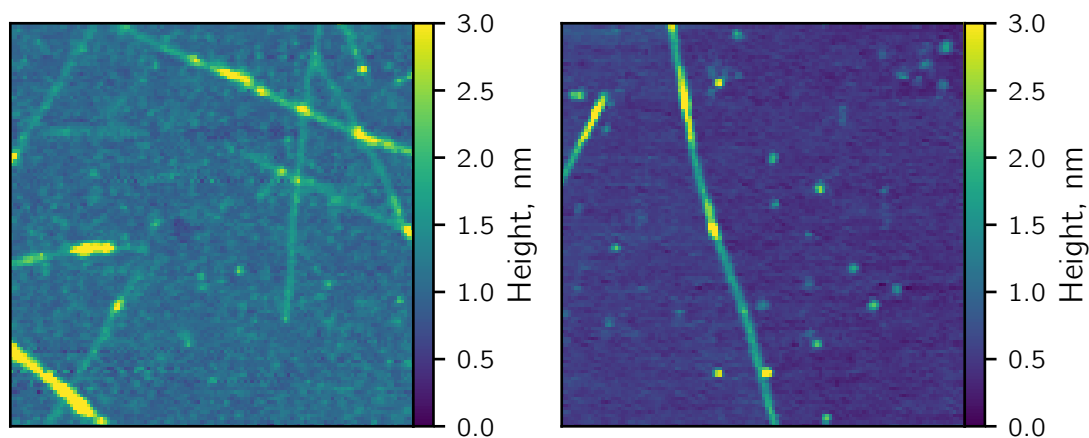


Figure IV.9: Left: AFM picture after dialysis with a 8 kDa MWCO membrane. **Right:** AFM picture after dialysis with 100 kDa MWCO membrane.

contained $1 \text{ g} \cdot \text{L}^{-1}$ of imogolite (Figure IV.11). Both experiments yielded dark brown to black colored samples. The UV spectra show a steadily increasing absorbance for both samples. However, the shape of the spectra and the rate of change is different for the sample that contains imogolite. The shape of the spectra of the sample containing imogolite behave similar to reactivity that has been observed by Du et al. for pH 7.^[243] Also the final absorption value is higher, which means that the presence of imogolite somehow increased the reaction yield.



Figure IV.10: Polydopamine samples. **Left:** Glass vial after polymerization without imogolite present. **Right:** Sample after polymerization with imogolite present. Note that there is no deposit on the glass vial. **Right:** Sample after polymerization with imogolite present. When left to rest, a gel forms that turns liquid again after agitating the sample.

Additionally, there are macroscopic differences between the samples. While the sample without imogolite forms a brown deposit on glass sample vials, the sample with imogolite does not (Figure IV.10). This might be linked to the high available surface area of imogolite. With an approximate area per formula unit of 0.3 nm^2 and $\approx 20 \%$ water in the imogolite dry weight, the surface area is approximately $730 \text{ m}^2 \cdot \text{L}^{-1}$ for a $1 \text{ g} \cdot \text{L}^{-1}$ imogolite dispersion. Furthermore, the sample with imogolite shows a gel like behavior if left to rest (Figure IV.10), but turns liquid again when the sample is agitated. Similar behavior is known from mixtures of imogolite and dicarboxylic acids.^[249] The buffered imogolite stock solution does not show this behavior. Overall, the results strongly suggest that the imogolite sample and the formed polydopamine interact. It is however not clear if polydopamine covers the tube surface.

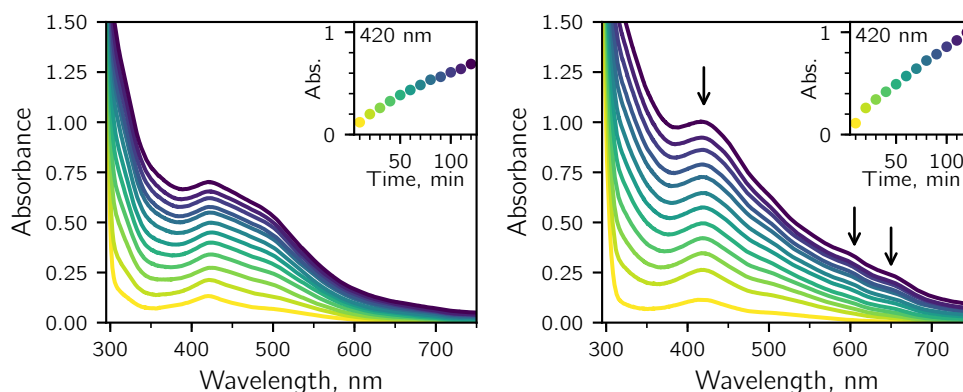


Figure IV.11: UV spectra acquired after 10 min of irradiation for a total of 120 min at $119 \text{ mW} \cdot \text{cm}^{-2}$. Insets show the absorbance at 420 nm for each individual spectrum. **Left:** $2 \text{ g} \cdot \text{L}^{-1}$ dopamine in 0.1 M acetate buffer solution. **Right:** $2 \text{ g} \cdot \text{L}^{-1}$ dopamine in $1 \text{ g} \cdot \text{L}^{-1}$ imogolite and 0.1 M acetate buffer solution. Arrows indicate differences.

TGA

A solution of $2 \text{ g} \cdot \text{L}^{-1}$ dopamine in 0.1 M acetate buffer and a dispersion of $1 \text{ g} \cdot \text{L}^{-1}$ imogolite with $2 \text{ g} \cdot \text{L}^{-1}$ dopamine in 0.1 M acetate buffer were irradiated for 1 h at $162.5 \text{ mW} \cdot \text{cm}^{-2}$ under stirring. Afterwards, the imogolite dispersion was divided and one part was dialyzed. A pristine imogolite dispersion and all three irradiated samples were freeze dried before TGA. Dopamine was analyzed as received.

Figure IV.12 shows the TGA curves of the prepared samples. Dopamine and polydopamine show two pronounced mass losses around 350°C and 600°C . Above 750°C no changes take place anymore. Imogolite shows a mass loss of more than 10% at 100°C due to the adsorbed water in-between the tubes. The mass loss around 150°C is contributed to water inside the tubes, while the mass loss around 300°C comes from the loss of structural water and the irreversible transformation of imogolite.^[215] The dialysed polydopamine-imogolite sample has a similar curve shape as pure imogolite but a lower residual weight (61.8%), indicating the presence of organic compounds in the sample. The approximate content of polydopamine in the polydopamine-imogolite sample after dialysis can be calculated from the residual weight of imogolite (69.8%) as 11.5%. For the polydopamine-imogolite sample before dialysis (17.8% residual weight) the same calculation yields a polydopamine content of 75%. However, the theoretical polydopamine content should be 66%, indicating inhomogeneities in the sample. Also, the curve shape of the polydopamine-imogolite sample

before dialysis is different from the dopamine and polydopamine curves. It is especially evident when a theoretical curve of 75 % polydopamine and 25 % imogolite is calculated. The difference in curve shape indicates a different degradation behavior of polydopamine after polymerization with imogolite present. From the different residual weight of the samples before and after dialysis it can be concluded that the majority of polydopamine was small enough to pass the membrane and was not permanently bound to a surface. However, no direct conclusions can be drawn regarding a surface modification of imogolite.

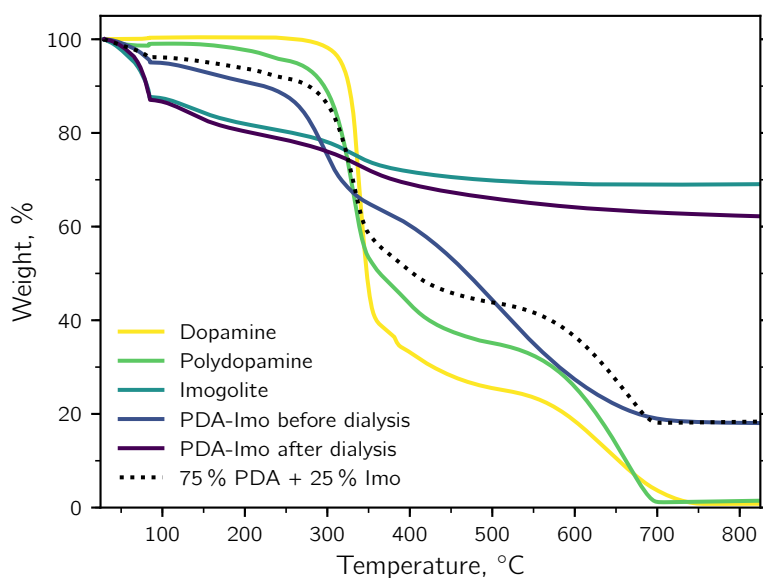


Figure IV.12: TGA curves of dopamine, polydopamine, imogolite and polymerized dopamine in presence of imogolite (PDA-Imo) before and after dialysis. The dotted line is calculated from the curves of polydopamine (75 %) and imogolite (25 %).

AFM and TEM

AFM images show the presence of dispersed imogolite tubes and small spherical objects, which are especially visible in the phase image (Figure IV.13). TEM images show similar structures, but the small objects are aggregated due to the drying (Figure IV.14). From the images it is hard to differentiate between allophane, potentially present polydopamine particles and particles that might be covered in polydopamine.

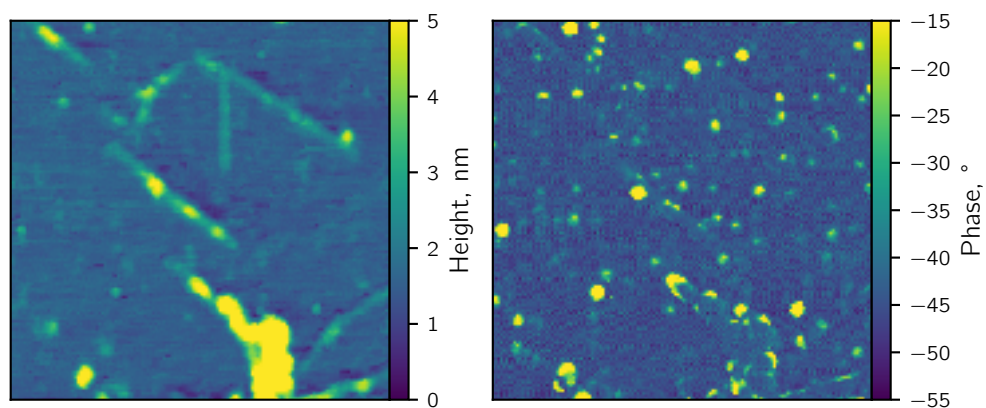


Figure IV.13: AFM image of a sample that was irradiated at $162.5 \text{ mW} \cdot \text{cm}^{-2}$ for 1 h with $2 \text{ g} \cdot \text{L}^{-1}$ dopamine, $1 \text{ g} \cdot \text{L}^{-1}$ imogolite and 0.1 M acetate buffer after dialysis. **Left:** Height profile. **Right:** Phase shift.

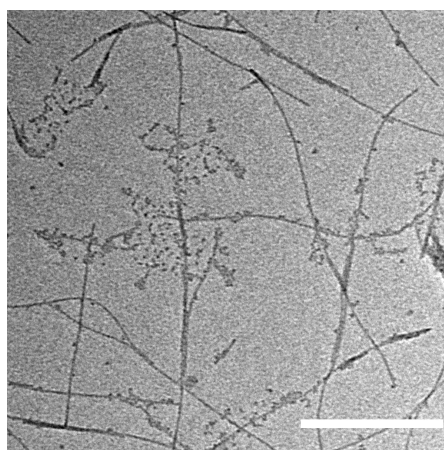


Figure IV.14: TEM image of a sample that was irradiated at $162.5 \text{ mW} \cdot \text{cm}^{-2}$ for 1 h with $2 \text{ g} \cdot \text{L}^{-1}$ dopamine, $1 \text{ g} \cdot \text{L}^{-1}$ imogolite and 0.1 M acetate buffer after dialysis. Scale bar is 200 nm.

SAXS

SAXS was used to probe the particle shape. However, the solutions were too diluted to obtain a good signal. To improve the scattering signal from imogolite it was concentrated by freeze-drying. Aggregation was prevented by adding $5 \text{ g} \cdot \text{L}^{-1}$ trehalose to the sample solution before freezing.^[250,251] Figure IV.15 shows the scattering patterns of imogolite, polymerized dopamine with imogolite, polydopamine and trehalose. The trehalose background was not subtracted. Imogolite shows nice oscillations due to its tubular structure and a bit of trehalose background. A peak around 0.8 nm^{-1} is visible that is normally not observed for imogolite. It is the result of the spatial proximity and alignment of the tubes in the trehalose matrix. Through the relation $d = 2\pi q^{-1}$ the real space distance can be calculated as 7 to 9 nm, which is approximately 3 times the tube diameter. The sample containing polydopamine that was polymerized in presence of imogolite does not show this peak, but a small indentation that might come from the superposition of the imogolite and polydopamine curve. Polydopamine and trehalose have only a simple slope of $\approx q^{-4}$ below 2 nm^{-1} due to a large sample grain. Overall, the use of trehalose seems to be well suited to observe imogolite, but its usefulness regarding polydopamine is not evident.

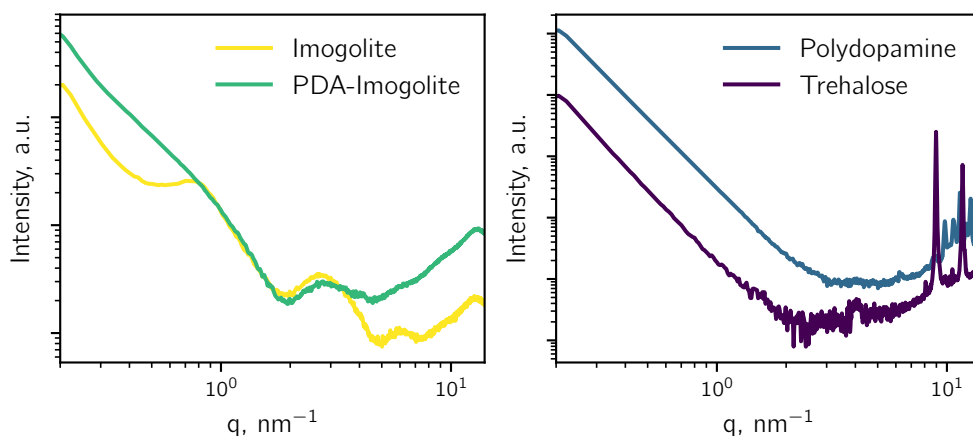


Figure IV.15: SAXS patterns of freeze dried samples in trehalose. **Left:** Imogolite and imogolite with polydopamine. **Right:** Polydopamine and trehalose alone.

Summary

Polydopamine seems to be an interesting candidate for the surface modification of imogolite. UV-Vis spectroscopy evidences a change in reactivity when imogolite is present during the

polymerization of dopamine with UV light and the dried material changes its degradation behavior. Furthermore, the tubes are still dispersed and do not degrade during the reaction. However, most of the organic part is removed from the sample by dialysis and the presence of allophane and proto-imogolite complicate the analysis by AFM and TEM.

SAXS does not allow a final conclusion, too. To continue the investigations into this surface modification approach a pure imogolite sample should be prepared that has no traces of allophane and proto-imogolite. Another approach that should be studied in parallel is the use of oxidants to initiate the polymerization.

4 Conclusion

In this chapter three major steps towards the surface modification of individual imogolite tubes were made. Solvents like DMF and DMSO might extend the way that imogolite can be worked with and might also open the road for non-aqueous based surface modification reactions. Dialysis is a facile way to remove proto-imogolite and might also be able to even remove allophane. Purifying imogolite in this way, opens the path to study imogolite without the presence of potentially more reactive side products. It is not clear if polydopamine coats imogolite. The results however are encouraging, since evidence for an interaction between imogolite and polydopamine has been found, imogolite stays dispersed and does not degrade during the procedure. Hence, the approach should be further studied.

V General Conclusion and Perspective

In this thesis, two different approaches have been pursued to study precipitation processes by confining them into droplets.

The first approach consisted of the development of a droplet microfluidic device that is compatible with organic solvents, e.g. mineral oil, alkanes and fluorinated oils, and usable for SAXS experiments at the same time. Although time consuming and challenging to achieve, a protocol has been developed to prepare such microfluidic devices from OSTE+. The properties of this material make it interesting to build sample environments for X-ray experiments, especially since it is resistant to beam damage when prepared appropriately. From the experimental session at the synchrotron SOLEIL, first results were collected. The strategy for data acquisition and treatment proved to be viable and it was possible to isolate the droplet and oil scattering signal in a single procedure. Applying the method to study the precipitation of cerium oxalate provided first insights. Inside the droplets, a scattering signal from 3-dimensional organized objects was observable, while a swelling of reverse micelles was observed in the oil phase. The size of the swollen micelles suggested that their growth is not only related to the extraction of water and reactants from the droplets, but might be linked to a reaction inside the micelle core. Experiments with a binary solution of water and 1,2-propanediol as solvent, provided evidence that it is possible to observe cerium oxalate crystals inside the droplets. To solve some problems with the experimental setup a new device holder was designed, which simplifies the use of the microfluidic device in the future. In these future experiments, a microfocused beam should be employed to improve the data quality. These experiments will give access to the first instants of precipitation and crystallization processes. The properties of the device and the acquisition method will also allow to study more complicated systems than pure mixing inside droplets. Especially, processes that involve coupling between the carrier and droplet phase can be studied, e.g. phase transfer of a compound and consecutive reactivity.

The second approach aimed to utilize the interfacial stabilization of water-in-oil droplets by imogolite nanotubes to study their reactant transport properties through their inner

lumen and to use this transport to control reactant-feeding rates into the droplets. In order to be able to stabilize droplets, a modification of the imogolite surface is however necessary. By conducting the first thorough characterization of the reaction of imogolite and alkylphosphonic acids, a surprising result was obtained. Although the protocol was claimed to be working well in literature, no evidence was found for grafted alkylphosphonic acid on the imogolite surface. Instead, the reaction produces interconnected domains of lamellar aluminum alkylphosphonates and residual imogolite tube bundles. This mixture has the same stabilization properties that were previously ascribed to modified imogolite and can be used to stabilize macroscopic aqueous droplets on an oil-water interface. The stabilization mechanism might be related to the hierarchical structure of the material, but needs further investigation. The observed reactivity with alkylphosphonic acids was explained by the surface chemistry of imogolite and questions the knowledge about its surface modification in general. To advance this field, novel approaches to obtain individually dispersed surface modified imogolite nanotubes have been explored. By screening different compounds, DMF and DMSO have been identified to be suitable solvents to stabilize imogolite dispersions and to be able to form liquid crystalline phases of imogolite. The use of these solvents gives access to a richer chemistry in combination with imogolite. In order to better understand the chemistry of imogolite, dialysis with high MWCO membranes was shown to remove the always present and potentially more reactive proto-imogolite from the imogolite dispersion. Using membranes with an even higher MWCO might remove allophane as well. Additionally, the surface modification of imogolite by polydopamine has been explored. Although not entirely conclusive, the UV-Vis and TGA results suggest that imogolite and polydopamine interact. Consequently, this approach should be further pursued. After all, there is still no direct experimental evidence for individually dispersed imogolite nanotubes with a hydrophobic exterior. Successful surface modification would also be a first step towards the experimental characterization of the imogolite transport properties.

While the imogolite Pickering emulsion approach needs more research effort, the droplet microfluidic in-situ SAXS approach has been proved a viable option that will be able to give concrete results in the near future. The future identification of the precipitation mechanism of cerium oxalate inside the droplets will be a milestone in the corresponding field and provide the foundation to study processes in adjacent fields (e.g. pigment production, plant protection and pharmaceuticals) by the developed method. Furthermore, it can be expected that the droplet microfluidic in-situ approach can be combined with other techniques, making it even more interesting to study all kinds of processes that benefit from, or require, a confinement inside droplets.

Appendix A

Characterization of Gold Nanoparticles

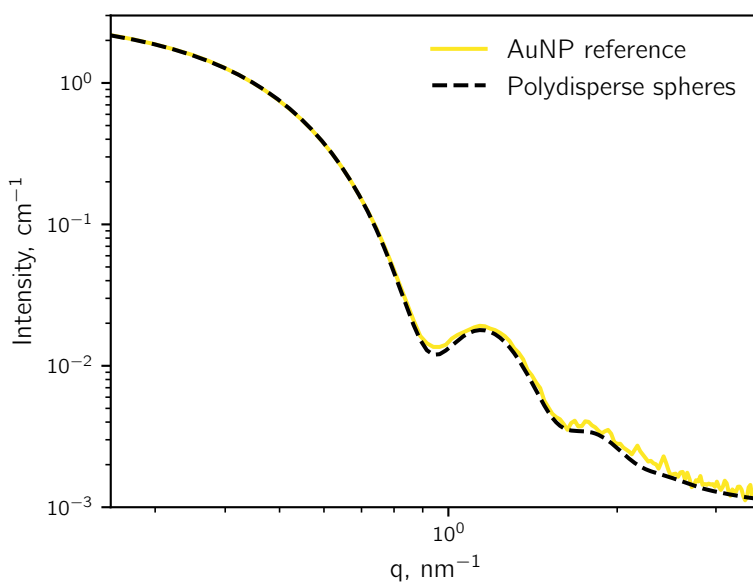


Figure A.1: SAXS pattern of the synthesized gold nanoparticles and a fit by polydisperse spheres. The fit yields a mean diameter of $9.4 \pm 1.0 \text{ nm}$ and a particle concentration of $8.8 \cdot 10^{12} \text{ cm}^{-3}$. The scattering length density (SLD) of the particles is $1.314 \cdot 10^{12} \text{ cm}^{-3}$ and the SLD of the medium is $9.396 \cdot 10^{10} \text{ cm}^{-3}$. A background of $1 \cdot 10^{-3} \text{ cm}^{-1}$ is added.

Transmission electron microscopy was performed on a Philips CM12 electron microscope operated at 80 kV. A drop of the solution was deposited on a copper grid covered with a carbon film (Agar Scientific). The excess liquid was blotted off with filter paper after a few seconds.

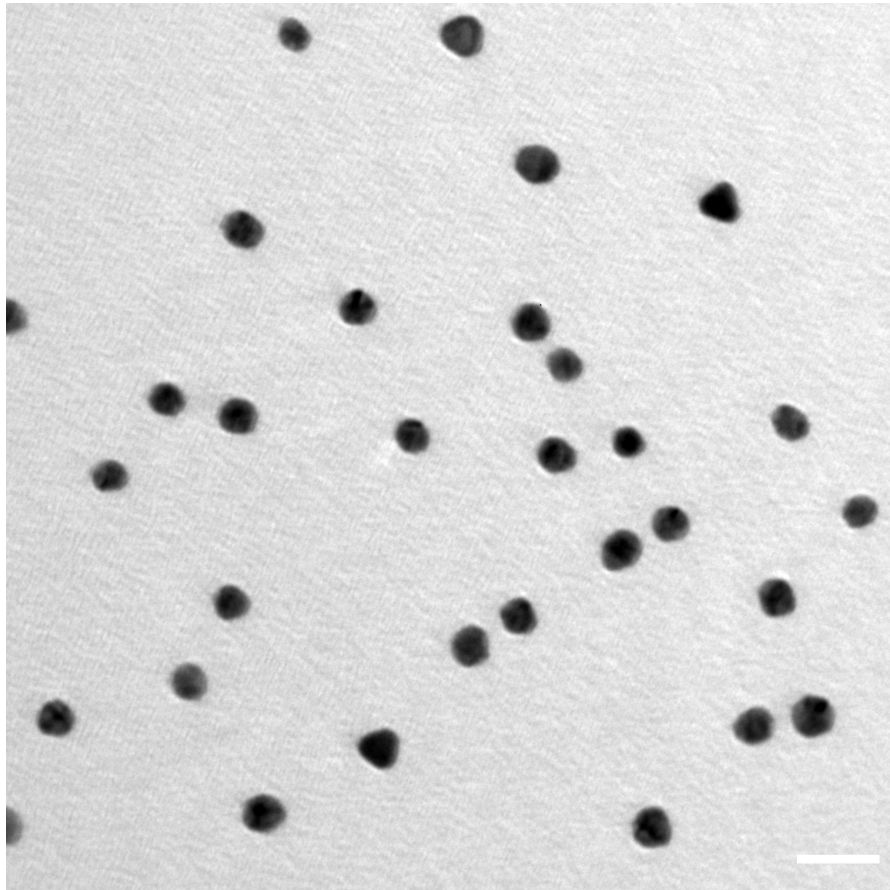


Figure A.2: TEM micrograph of the synthesized gold nanoparticles. Scale is 20 nm.

Appendix B

Microfluidic Device Holders

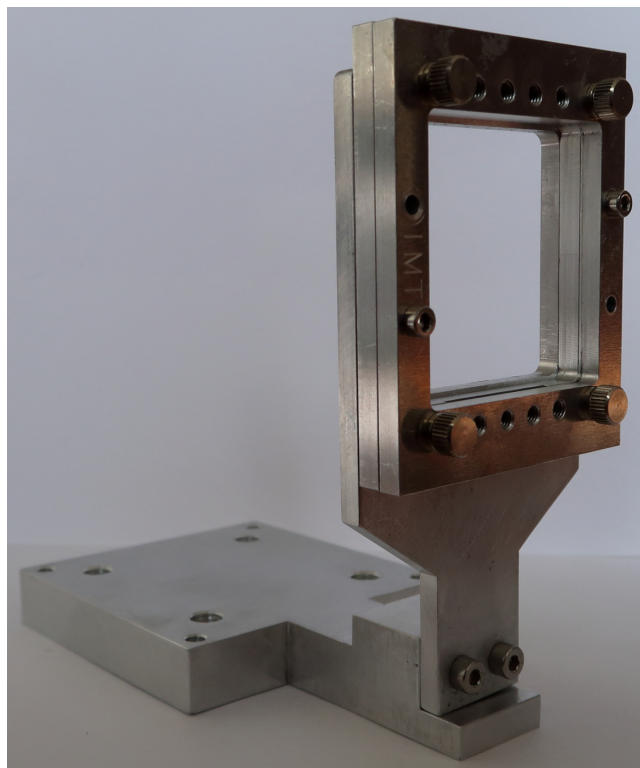


Figure B.1: IMT device holder mounted on the interface to the SWING beamline.

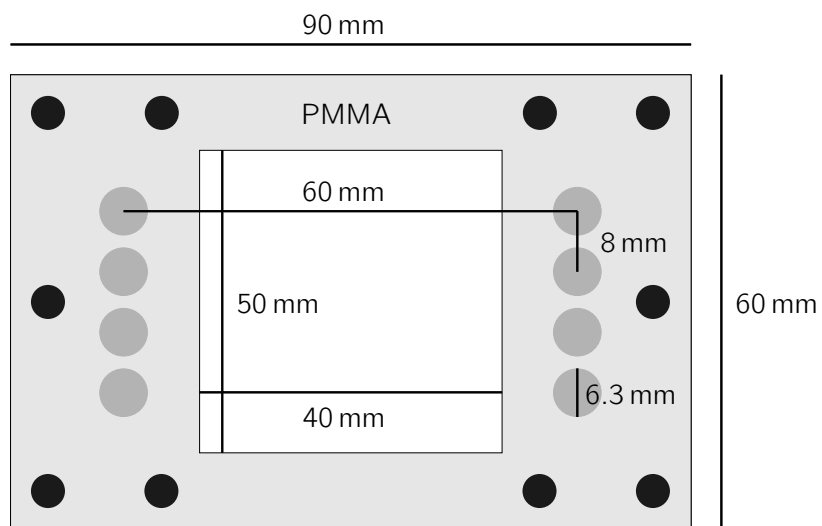


Figure B.2: Measurements for the PMMA device holder.

Appendix C

Python 3 Code for In-situ SAXS Data Treatment

Import Packages

```
import nexusformat.nexus as nx
import numpy as np
import os
```

Samplefile

```
#read parameters from representative samplefile
samplefile = "C:\\\\Samplefile"
dc=nx.nxload(samplefile)
im=dc[list(dc)[0]].scan_data.eiger_image.nxvalue

#Photon energy
energy=dc[list(dc)[0]].SWING['i11-c-c03__op__mono']
```

#Detector parameters

```
Eiger=dc[list(dc)[0]].SWING['EIGER-4M']
```

Maskfile

```
# read mask
maskname='maskname'
MaskFilepath="C:\\\\MaskFilepath"
f=open(MaskFilepath+'/' +maskname)
```

```

#convert mask
m=f.read()
m=m.replace("\n",";")
m=m.split(';')
am=np.array(m)
am=am.astype(bool)
am=am.reshape((np.shape(im)[1],np.shape(im)[2]))
am=np.invert(am)

```

pyFAI Set-up

```

from pyFAI import azimuthalIntegrator

fai=azimuthalIntegrator.AzimuthalIntegrator()
fai.setFit2D(
    float(Eiger['distance']), #distance
    centerX=float(Eiger['dir_beam_x']), #xpos
    centerY=float(Eiger['dir_beam_z']), #ypos
    tilt=0,
    pixelX=float(Eiger['binning_x'])*
        float(Eiger['pixel_size_x']),
    pixelY=float(Eiger['binning_y'])*
        float(Eiger['pixel_size_z']),)
fai.set_wavelength(float(energy['wavelength'])*1e-9)

```

Function: Read Data

```

#Function: read data
def read_nexus(NXSfile):
    nxsfile=nx.nxload(NXSfile)
    name=str(nxsfile[list(nxsfile)[0]])
    namesplit=str(nxsfile[list(nxsfile)[0])).split('_')
    name=namesplit[-1]+'_'+name
    image=nxsfile[list(nxsfile)[0]].scan_data.eiger_image.nxvalue
    Eiger=nxsfile[list(nxsfile)[0]].SWING['EIGER-4M']
    expT=float(Eiger['exposure_time'])*0.001
    mi8b=nxsfile[list(nxsfile)[0]].SWING['i11-c-c09__dt__mi_diode.8b']

```

```

gain=mi8b['Gain']
intensity=mi8b['intensity']
transFlux=gain*intensity
Klist = transFlux * expT
return name, image, Klist , intensity

```

Function: Azimuthal Integration

```

def Radial_Average(image):
    datalist = []
    for j in range(1, len(image)):
        K = Klist[j]*N
        q,i,s=fai.integrate1d(image[j],
                               1000,
                               correctSolidAngle=True,
                               error_model="poisson",
                               mask=am,
                               normalization_factor = K,
                               )
        data = np.column_stack((q,i,s))
        datalist.append(data)
    return datalist

```

Function: Find Threshold

```

def Threshold(data_array, low_q, high_q):
    mean_list=[]
    somelist=[]
    for j in data_array:
        q = j[:,0]
        i = j[:,1]
        loc = np.where(np.logical_and(q>=low_q, q<=high_q))
        d = np.mean(i[min(loc[0]):max(loc[0])])
        b = np.mean(i)
        mean_list.append(d)
        somelist.append(b)
    a = [x+2 for x in range(0, len(mean_list))]

```

```

# +1 because frame 0 is sometimes bad,
# and +1 because python starts counting at 0
threshold_oil = np.percentile(mean_list, 90)
# x > threshold
threshold_droplet = np.percentile(mean_list, 10)
# x < threshold
return a,
        mean_list,
        threshold_oil,
        threshold_droplet,
        somelist

```

Function: Select Data

```

def Select(data_array, low_q, high_q):
    droplet_list = []
    oil_list = []
    for j in data_array:
        q = j[:, 0]
        i = j[:, 1]
        loc = np.where(np.logical_and(q >= low_q, q <= high_q))
        d = np.mean(i[min(loc[0]):max(loc[0])])
        if d < threshold_droplet:
            droplet_list.append(j)
        if d > threshold_oil and threshold_oil > 0:
            oil_list.append(j)
    return droplet_list, oil_list

```

Function: Average Data

```

# Function: Average data and save file
def AverageData(selected_data):
    nq = 0
    ni = 0
    ns = 0
    for j in selected_data:
        q = j[:, 0]

```

```

    i = j[:,1]
    s = j[:,2]
    nq+=q
    ni+=i
    ns+=s
q_avg=nq/len(selected_data)
i_avg=ni/len(selected_data)
s_avg=ns
return q_avg, i_avg, s_avg

```

Function: Export Data

```

def exportData(selected_data, suffix):
    q_avg, i_avg, s_avg = AverageData(selected_data)
    np.savetxt(name+"_"+suffix+".txt",
               np.c_[q_avg, i_avg, s_avg],
               delimiter="\t",
               newline='\n')

```

Read a Folder and Show Content

```

folder="D:\\test"
filelist = []
for i in os.listdir(folder):
    filelist.append(folder+os.sep+i)
list(filelist)

```

Manually Define Files from Previous List

```

filelist = []
filelist = [
'TestFile'
]
list(filelist)

```

Data Treatment

```

Qmin = 1.0 #for selection

```

```
Qmax = 1.16 #for selection
N=1 #normalization factor
T=1 #Thickness

for i in filelist:
    name, image, Klist, diode = read_nexus(i)
    data_list = Radial_Average(image)
    a,
    mean_list,
    threshold_oil,
    threshold_droplet,
    somelist = Threshold(data_list, Qmin, Qmax)
    droplet, oil = Select(data_list, Qmin, Qmax)

exportData(droplet, "droplet")
exportData(oil, "oil")
exportData(data_list, "all")
```

Appendix D

Additional In-situ SAXS Data

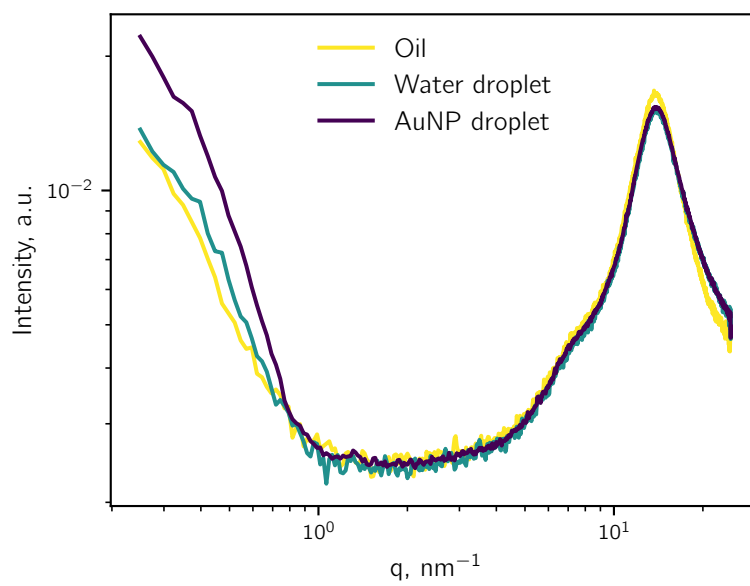


Figure D.1: Raw SAXS for the oil phase, water droplets and droplets that contain gold nanoparticles (AuNP).

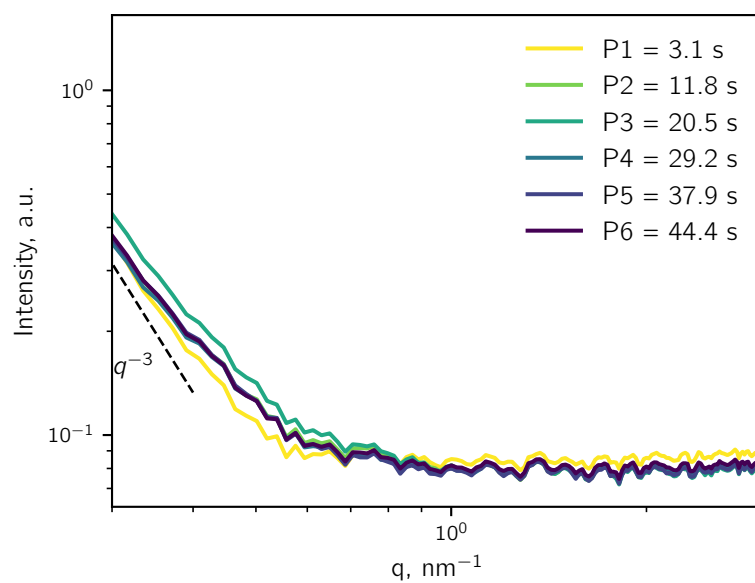


Figure D.2: SAXS pattern at different reaction times along the microfluidic channel for the droplet phase. The data was normalized and the contribution of OSTE+ was subtracted as background. Due to the lack of the appropriate data, the background subtraction of air and the sealing material of the vacuum tubes is not performed.

Appendix E

^{27}Al MAS NMR Deconvolution of Imogolite Samples

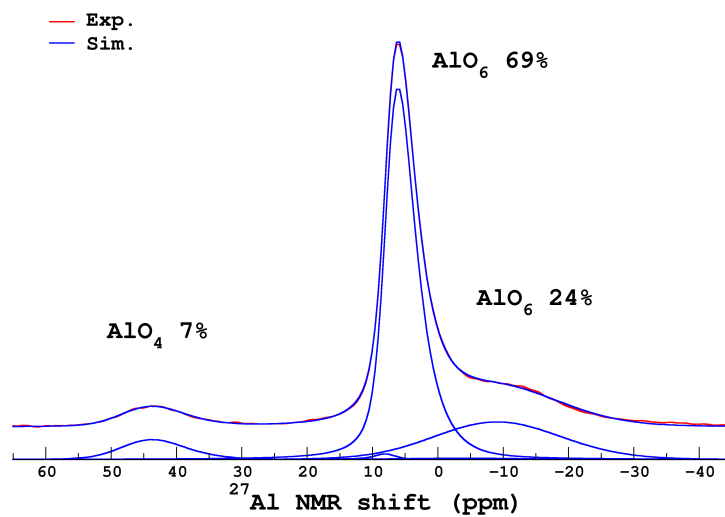


Figure E.1: Deconvolution of the ^{27}Al MAS NMR spectrum of Sample A1.

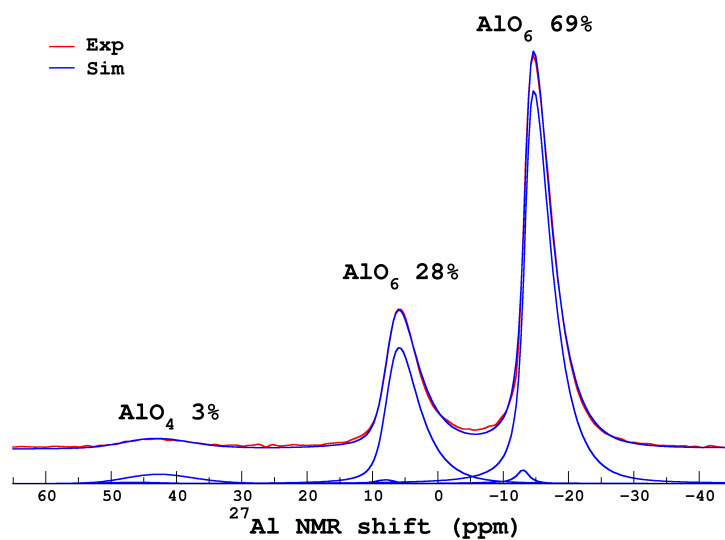


Figure E.2: Deconvolution of the ^{27}Al MAS NMR spectrum of Sample B.

Appendix F

Conductivity Measurements

Experiments to probe if there is ion transport between an imogolite stabilized droplet and a bulk water phase were made with the apparatus depicted in Figure F.1. The apparatus was filled with high purity water ($18.2 \text{ M}\Omega \cdot \text{cm}$) until the conductivity probe (InLab 751-4mm, MettlerToledo) was covered. Then the water was layered by a toluene dispersion that contained modified imogolite. To see if ion transport takes place, a droplet of an aqueous salt solution (NaCl or $\text{Ce}(\text{NO}_3)_3$) was deposited on the interface. For the case of droplet coalescence, the high purity water phase was exchanged with the help of the access ports and a peristaltic pump (101U, Watson Marlow). Temperature control was achieved by a thermostatic jacket that was connected to a thermostat (Julabo, F20-HC). The conductivity probe was connected to a conductivity meter (CDM210, Radiometer Analytical). Data read out was managed by a computer and a custom Python code. No significant change of conductivity was observable. Long observation periods were hard to achieve due to occasionally occurring communication errors between the computer and the conductivity meter. A major drawback of the experimental setup are the access ports for the conductivity probe. This area is not well mixed and leads to a residual pollution that results in a signal increase for the measured conductivity after the water is exchanged (Figure F.2). After this initial increase no change is visible anymore. Since the reaction with phosphonic acid did not yield surface modified imogolite, the experiments were not continued.

If individual surface modification of imogolite is achieved and these particles are able to stabilize droplets against coalescence, the experiments should be repeated. However, a stable interface to record the measurement data should be created. Furthermore, a new apparatus should be developed that does not have issues with badly accessible water volumes. Also a conductivity probe head with a larger cross-sectional area might be useful.

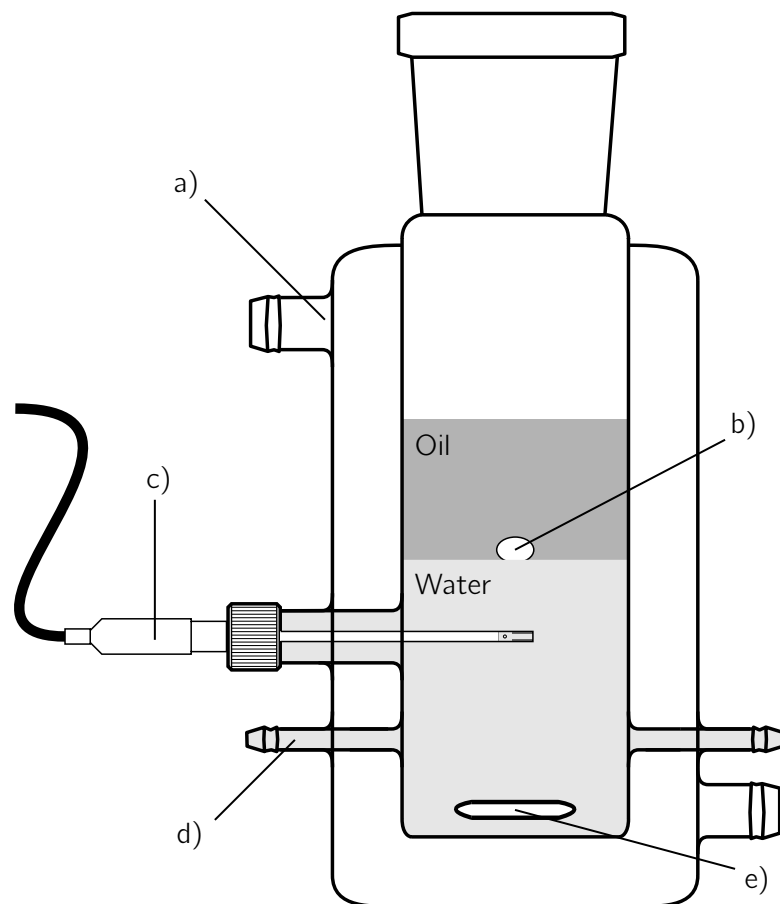


Figure F.1: Custom experimental setup to measure ion transport by conductivity made from glass. a) Thermostatic jacket connected to a thermostat. b) Aqueous salt solution droplet at the interface between oil and water. c) Conductivity sensor connected to a conductivity meter. d) Access to exchange water. e) Magnetic stirring bar.

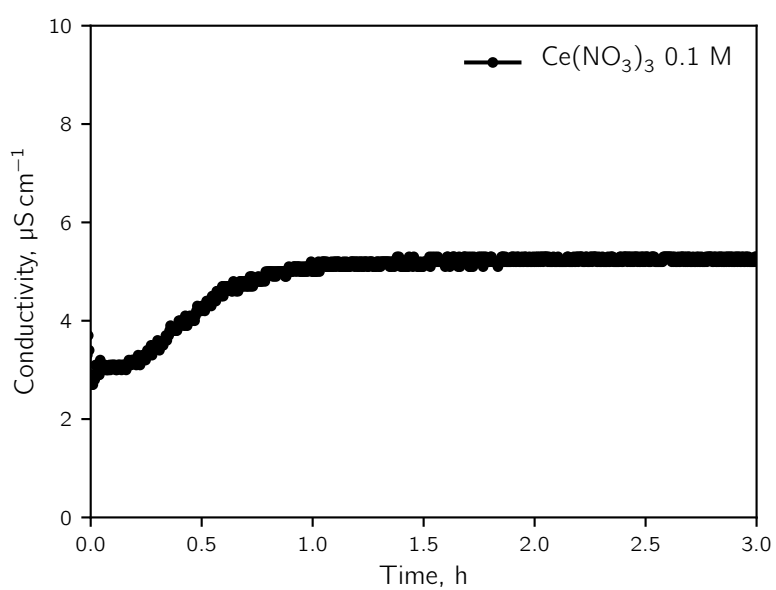


Figure F.2: Example for the temporal evolution of the measured conductivity after exchanging the water. The droplet on the interface is 0.1 M in $\text{Ce}(\text{NO}_3)_3$.

Appendix G

Dialysis of Methyl Modified Imogolite

Methyl imogolite has been synthesized by Marie-Claire Pignie using a protocol inspired from Bottero et al.^[159]

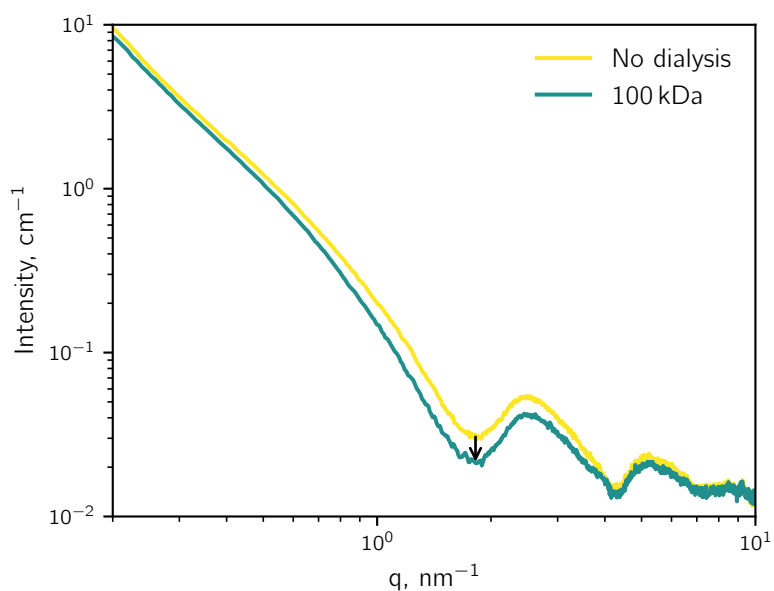


Figure G.1: SAXS patterns of methyl imogolite dispersions before and after dialysis with a 100 kDa membrane.

Appendix H

Additional AFM Images of Imogolite Samples

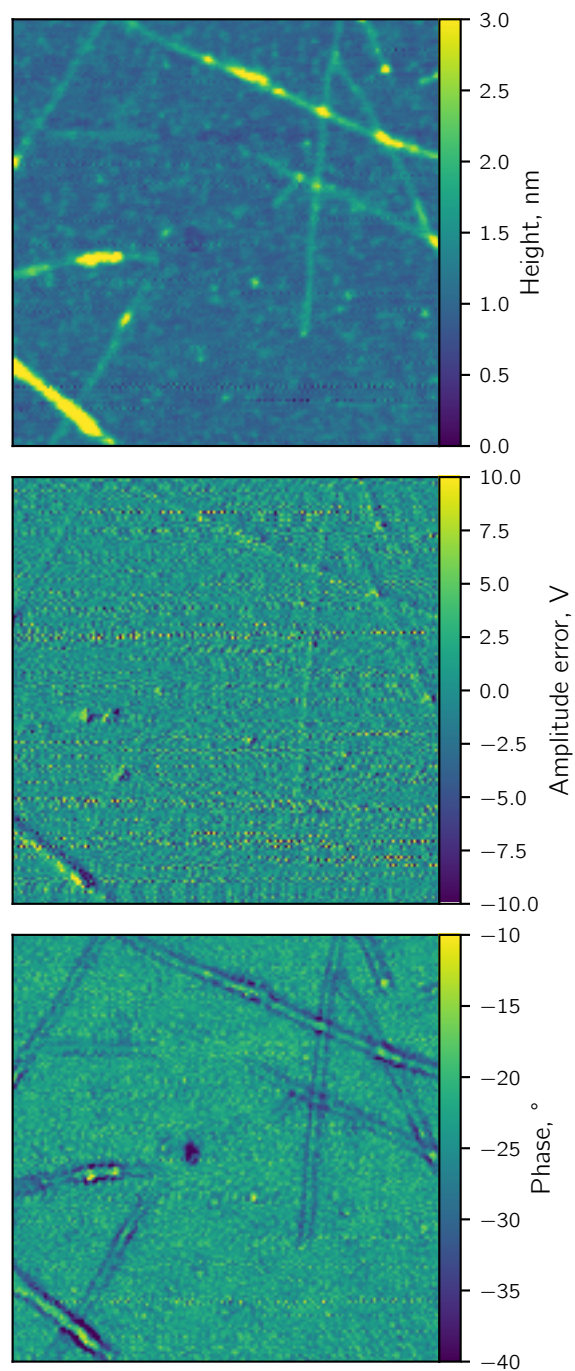


Figure H.1: AFM image of imogolite that was dialysed with a 8 kDa. Image is $1 \times 1 \mu\text{m}^2$.

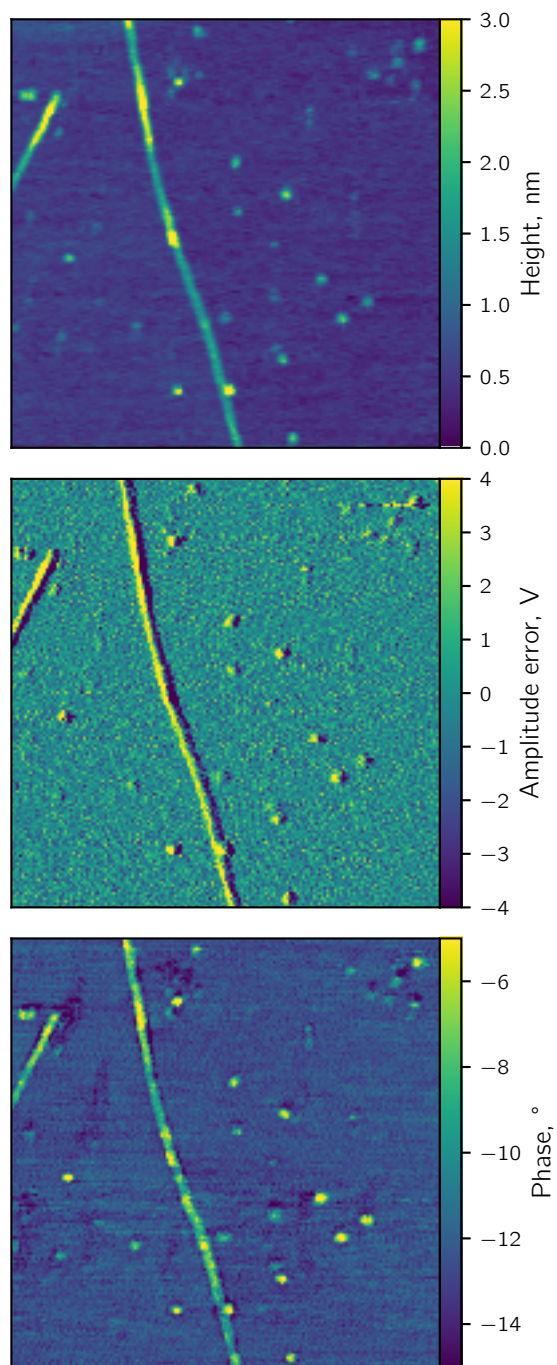


Figure H.2: AFM image of imogolite that was dialysed with a 100 kDa. Image is $1 \times 1 \mu\text{m}^2$.

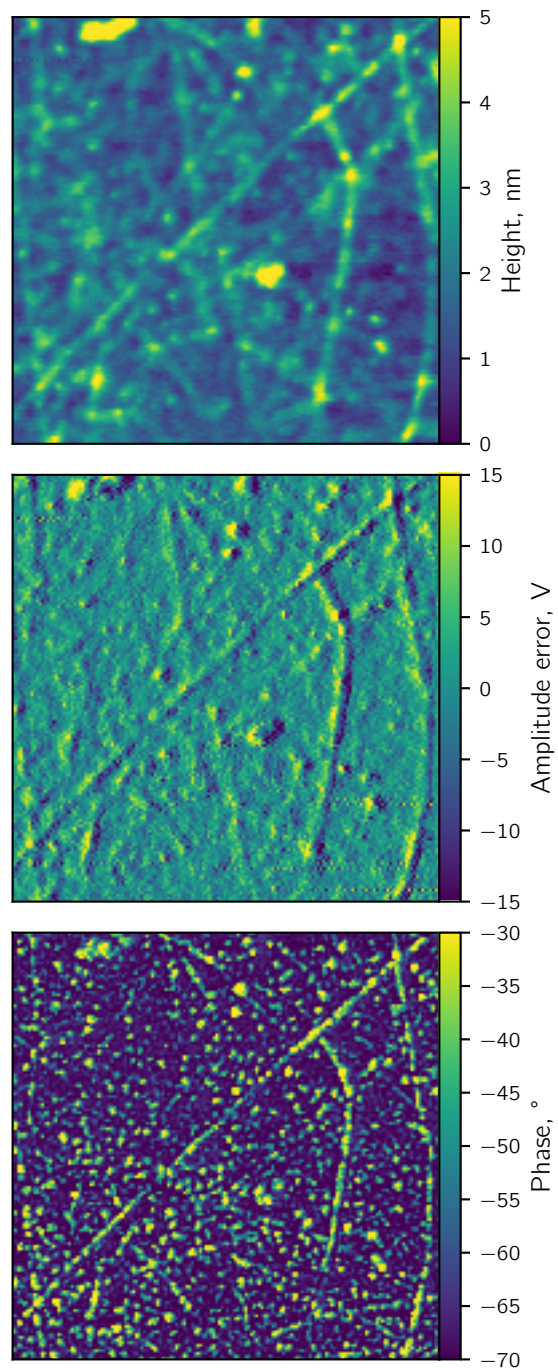


Figure H.3: AFM image of a sample after dopamine polymerization in the presence of imogolite and 0.1 M acetate buffer without dialysis. Image is $1 \times 1 \mu\text{m}^2$.

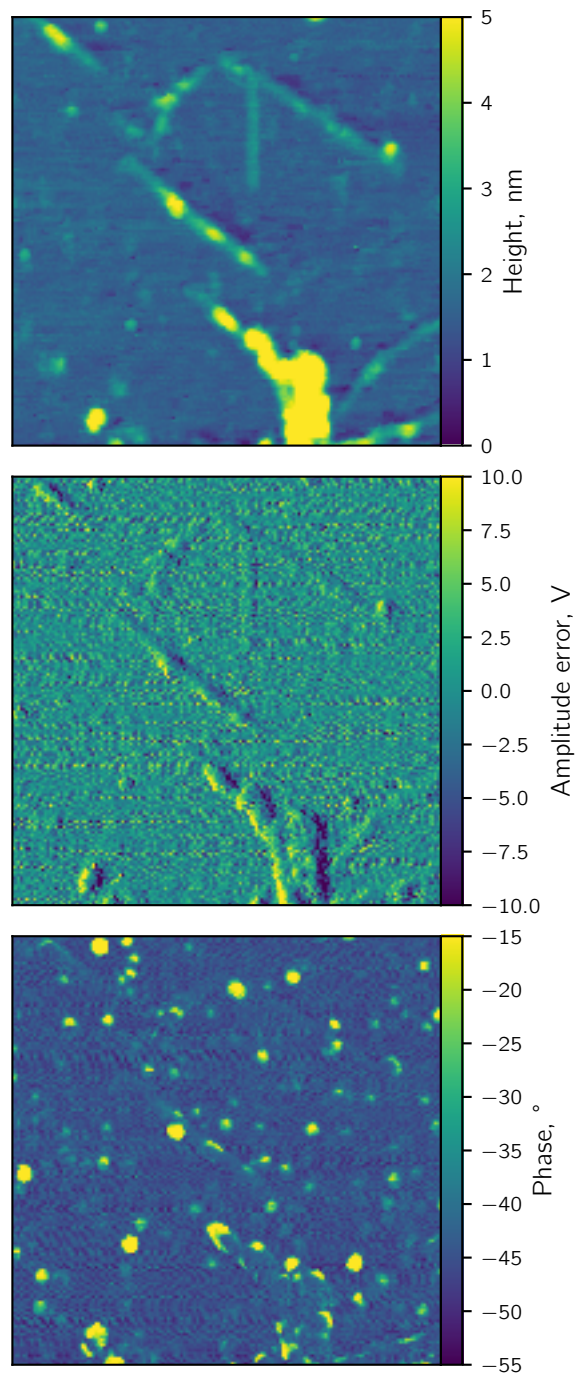


Figure H.4: AFM image of a sample after dopamine polymerization in the presence of imogolite and 0.1 M acetate buffer after dialysis. Image is $1 \times 1 \mu\text{m}^2$.

Appendix I

Résumé français

De nombreux secteurs industriels tels que la production de pigments, de catalyseurs, de produits pharmaceutiques, de minerais ou de combustibles nucléaires font intervenir des étapes de précipitation et de cristallisation. La morphologie et la structure des composés obtenus, qui dépendent de ces procédés et de leurs conditions de mise en œuvre, ont un impact direct sur leurs propriétés. Il est donc important de pouvoir contrôler ces étapes. Bien que ces procédés soient utilisés à grande échelle avec un contrôle relatif des solides formés, les mécanismes de formation ne sont que partiellement compris. Une meilleure compréhension des différentes étapes de formation permettrait d'obtenir des leviers de contrôle adaptés à chaque composé et application. Cette thèse se place dans ce cadre très général du contrôle de la précipitation et plus particulièrement de la précipitation en gouttes d'émulsion eau dans l'huile. En effet, il a été démontré récemment l'intérêt de l'utilisation de procédés de dispersion de gouttes d'eau (contenant des réactifs) dans huile pour faire de la précipitation. Cette approche qui consiste à diviser le milieu réactionnel en gouttelettes, peut être facilement extrapolée à l'échelle industrielle via les colonnes pulsées. Outre les perspectives prometteuses en termes de contrôle notamment de la taille et de la filtrabilité des précipités, ce procédé continu est particulièrement intéressant pour l'industrie nucléaire, dans le cadre du traitement-recyclage du combustible irradié, car il permettrait à la fois d'augmenter les cadences de production, tout en maîtrisant la sûreté. Pour approfondir la maîtrise de la précipitation dans ces milieux complexes, deux approches différentes ont été explorées. L'objectif était de trouver des leviers de contrôle pour moduler et suivre la réactivité dans une goutte d'émulsion. La première approche était basée sur le couplage d'une puce microfluidique génératrice de train gouttes avec la diffusion de rayons X aux petits angles (SAXS) pour des suivis de réactivité in situ. Le matériau choisi, le polymère non stœchiométrique thiol-ene-epoxy (OSTE+) a été caractérisé pour confirmer sa compatibilité avec la diffusion des rayons X aux petits angles, en particulier, le vieillissement

sous faisceau et sa transparence aux X. Une puce de géométrie spécialement conçue a ensuite été développée dans ce matériau pour suivre la réactivité dans une goutte d'eau dispersée dans différentes huiles (huile fluorés, alcane, huile minérale en présence ou non de tensioactif). L'obtention, en OSTE+ uniquement, d'une puce de faible épaisseur (200 à 400 nm) a permis une utilisation du système sous faisceau synchrotron. Un traitement original des données a été mis au point pour séparer le signal des gouttes de phase aqueuse du signal de la phase continue (huile) ce qui a permis de valider le montage dans le cas de la précipitation d'oxalate de cérium. Ces premiers résultats valident l'approche de l'utilisation du matériau OSTE+ pour des études in situ SAXS de réactivité en puce microfluidique et ouvre l'utilisation de ces puces à d'autres types d'expérience sur synchrotron. La deuxième approche de cette thèse avait pour objectif de contrôler le transport de réactifs entre gouttes d'émulsion eau dans huile. Pour cela, des nanotubes d'aluminosilicate (imogolites) ont été choisis pour stabiliser les gouttes d'émulsion et étudier le transport de réactifs entre gouttes via ces nanotubes. Ces nanotubes solubles dans l'eau devaient être fonctionnalisés pour être dispersables en milieu organique. La caractérisation poussée de la fonctionnalisation des imogolites par des acides alkylphosphoniques (réaction décrite dans la littérature) a montré pour la première fois que cette réaction ne conduisait pas à une fonctionnalisation de surface mais à un matériau composite aux propriétés interfaciales remarquables. La structure multi-échelle (nanotubes et phases lamellaires imbriquées) est probablement à l'origine de ces propriétés. De nouvelles voies de fonctionnalisation de surface ont ensuite été développées pour rendre les imogolites hydrophobes. Une approche originale basée sur la réduction de la dopamine sous rayonnement UV a été initiée. Il a été démontré une interaction forte entre la dopamine et les imogolites. Cette voie très prometteuse mérite d'être suivie pour obtenir des imogolites hydrophobe en surface autour d'une cavité hydrophile. Ces travaux exploratoires sur de nouveaux leviers de contrôle de la réactivité dans des émulsions eau dans huile ont ouvert de nouvelles directions. Grâce à un protocole rigoureux de fabrication de puces complètes en OSTE+, le suivi de la réactivité sous rayonnement X est aujourd'hui envisageable. Le matériau composite imogolite/alkylphosphonique identifié et caractérisé, dont les propriétés interfaciales sont proches de celles observées dans les « liquid marble », pourrait être mis à profit pour le transfert de réactif, en contrôlant par exemple sa porosité. Enfin la fonctionnalisation des imogolites par la polydopamine laisse entrevoir des possibilités de chimie plus complexe à la surface des imogolites.

List of Figures

I.1	LaMer diagram describing a separated nucleation and growth process. . .	2
II.1	Left: Typical numerical values of the Reynolds number for water ($\nu = 1 \cdot 10^{-6} \text{ Pa} \cdot \text{s}$) at different hydraulic diameters and fluid velocities. Right: Typical numerical values of the Péclet number for small ions in water ($D = 1 \cdot 10^{-9} \text{ m}^2 \cdot \text{s}^{-1}$).	9
II.2	The capillary number at a fluid velocity of $u = 1 \text{ m} \cdot \text{s}^{-1}$	10
II.3	Photolithographic process.	11
II.4	Replication molding process.	12
II.5	Examples for different droplet generation geometries for a fluid flow. . .	13
II.6	Droplet flow behaviours in a T-junction.	14
II.7	Schematic representation of a SAXS experiment showing the incident, the transmitted and scattered part of the beam.	15
II.8	Scattering of two points. Their relative positions are characterized by \vec{r}	17
II.9	Droplet generation in a microfluidic device in the path of a rectangular X-ray beam.	20
II.10	Example for an acquisition frequency that is higher than the droplet frequency. The obtained scattering patterns are isolated droplet and oil phases and mixtures of both.	21
II.11	The three potential acquisition possibilities in droplet microfluidics.	21
II.12	Lamination of WBR dryfilm onto a Si wafer with a hot-roll laminator.	22
II.13	OSTE+ device fabrication.	24
II.14	Left: IMT device holder with tube connector. Right: IMT tube connector with PTFE gasket.	27
II.15	Schematic representation of the microfluidic device.	27
II.16	Left: WBR/Si Master. Right: Finished OSTE+ device.	30
II.17	width=0.15	33
II.18	Surface roughness profile of the flat side of a OSTE+ device in μm	34

II.19	Left: Height profile for the channels on the WBR/Si master and in the finished device. Right: Microscopy image for a channel in an open OSTE+ Device. The channel has a width of 190 μm . Scale bar is 100 μm .	34
II.20	Regions probed by a digital micrometer.	36
II.21	Left to right: Growth of precipitate in the inlet and subsequent break-off for too low center channel flow rates. Scale bars are 200 μm .	38
II.22	A fluorescent colorant is mixed with water inside the droplets at a total flow rate of 15 $\mu\text{L} \cdot \text{min}^{-1}$. The fourth droplet shows homogeneous fluorescence. Scale bar is 300 μm .	39
II.23	Droplets with a concentration of 0.0010 M $\text{Ce}(\text{NO}_3)_3$ and 0.0015 M $\text{H}_2\text{C}_2\text{O}_4$.	40
II.24	Droplets with a concentration of 0.010 M $\text{Ce}(\text{NO}_3)_3$ and 0.015 M $\text{H}_2\text{C}_2\text{O}_4$.	41
II.25	Calculated transmission of OSTE+ at different sample thickness and different photon energies. Data was calculated with the help of xraylib. ^[127]	43
II.26	Calculated linear attenuation coefficient μ of different polymers.	45
II.28	Left: OSTE+ device after normal curing at 90 °C. Right: OSTE+ device after additional curing at 150 °C for 7 days.	47
II.29	Staining observed on an OSTE+ device after an in-situ experiment.	47
II.30	Comparison of the aging behaviour of OSTE+.	47
II.31	Device mounted on the SWING beamline.	48
II.32	Raw scattering patterns that were acquired at one sampling point.	49
II.33	Scattering patterns after selection (Figure II.32).	50
II.34	SAXS patterns of gold nanoparticles from a Kapton capillary as reference and inside the microfluidic device from the feeding channel and from the droplets.	51
II.35	SAXS patterns of the oil phase at different points in the microfluidic channel.	54
II.36	SAXS patterns of 1 % Span 80 (w/w) in light mineral oil before and after equilibration with H_2O , 0.15 M $\text{H}_2\text{C}_2\text{O}_4$ (Ox_{aq}) and 0.10 M $\text{Ce}(\text{NO}_3)_3$ (Ce_{aq}).	54
II.37	SAXS patterns of the droplet phase at different points in the microfluidic channel.	55
II.38	Droplet scattering patterns after subtraction of the q^{-3} slope.	55
II.39	In-situ scattering patterns of cerium oxalate formation in binary solvent.	57

II.40	Typical detector photon counts after 20 ms of acquisition at 16 keV for an in-situ experiment.	58
II.41	Relative alignment of the beam and the channel.	58
II.42	Top view on the PMMA device holder.	59
II.43	Side view on the PMMA device holder.	59
III.1	Scheme of oil in water emulsion droplets.	63
III.2	A segment of the imogolite structure according to Cradwick et al. ^[149] The unit cell is highlighted by the red line.	65
III.3	Imogolite structure viewed down the tube axis as suggested by Cradwick et al., ^[149] adapted from MacKenzie et al. ^[155] The tube interior is filled with water. ^[156]	66
III.4	Cryo-TEM picture of imogolite.	74
III.5	SAXS pattern of dispersed imogolite and its corresponding fit by a core-shell cylinder, yielding an outer diameter of 2.8 nm.	75
III.6	IR spectra of imogolite, samples A1 – A5, sample B and DPA.	76
III.7	Left: ³¹ P MAS NMR spectra of DPA, sample A1 and sample B. Right: ²⁹ Si MAS NMR spectra of imogolite, sample A1 and sample B, normalized to highest peak intensity.	78
III.8	Left: ²⁷ Al MAS NMR spectra of imogolite, sample A1 and sample B, normalized to highest peak intensity. Right: ²⁷ Al{ ³¹ P} REDOR signals of the sites observed in sample A1 and sample B. Lines between data points are for clarity.	79
III.9	²⁷ Al MQMAS (triple quantum) spectra.	80
III.10	Powder X-ray scattering patterns of imogolite, samples A1 – A5 and sample B.	82
III.11	Left: Scattering patterns of samples C, D and E. Peaks from aluminum alkyl phosphonate are indicated. The scattering patterns of samples D and E were collected from the wet sediment after centrifugation. Right: Repeat distance d in relation to the used alkylphosphonic acid chain length in several phosphonate phases by Lassiaz et al., ^[196] Picot et al., ^[30] Gao et al., ^[194] Park et al., ^[178] Bac et al. ^[179] and the presented data.	83

III.12	Left and center: SEM image of sample A5. Right: TEM image of sample A5. At least two interconnected phases are visible, as pointed out by the arrows: elongated bundles of aggregated imogolite and plate-like objects with a lamellar structuration. Scale bars are 5 μm (left), 100 nm (center) and 25 nm (right).	84
III.13	Schematic representation of an imogolite tube. Arrows indicate the positions of bridging $\text{Al}_2(\text{OH})$ groups that cover the tube wall and $\text{Al}-\text{OH}$ (and $\text{Al}-\text{OH}_2^+$) groups on the terminal points.	85
III.14	Water-in-oil emulsion stabilized by sample A5 in toluene. The aqueous phase is stained with fluorescein in the center image. Scale bars are 50 μm . 86	
III.15	Left: A 20 μL water droplet stabilized by modified imogolite at the toluene/water interface. Right: The same stabilized droplet, illuminated from below. Scale bars are 1 mm.	86
IV.1	Skeletal formula of dopamine.	90
IV.2	Experimental set-up for the polymerization of dopamine. The sample is placed on a magnetic stirring plate and illuminated at a fixed distance by the UV lamp.	92
IV.3	Measured lamp power at a distance of 23 cm	92
IV.4	From left to right: 2:1, 4:1, 6:1 and 10:1 (v/v) solvent ratios for propylene carbonate and the aqueous dispersion of imogolite. Samples are between crossed polarizers.	95
IV.5	Dispersed imogolite at different concentrations. Left: $\approx 5 \text{ g} \cdot \text{L}^{-1}$. Center: $\approx 10 \text{ g} \cdot \text{L}^{-1}$. Right: $\approx 25 \text{ g} \cdot \text{L}^{-1}$	96
IV.6	SAXS patterns of imogolite dispersed in DMF at different concentrations. Curves are displaced for clarity.	98
IV.7	SAXS patterns of imogolite dispersions that have been dialyzed with different molecular weight cut-offs.	99
IV.8	Left: Cryo-TEM after dialysis with a 8 kDa MWCO membrane. Right: Cryo-TEM after dialysis with 100 kDa MWCO membrane. Scale bars are 25 nm.	100
IV.9	Left: AFM picture after dialysis with a 8 kDa MWCO membrane. Right: AFM picture after dialysis with 100 kDa MWCO membrane.	100

IV.10	Polydopamine samples. Left: Glass vial after polymerization without imogolite present. Right: Sample after polymerization with imogolite present. Note that there is no deposit on the glass vial. Right: Sample after polymerization with imogolite present. When left to rest, a gel forms that turns liquid again after agitating the sample.	101
IV.11	UV spectra acquired after 10 min of irradiation for a total of 120 min at $119 \text{ mW} \cdot \text{cm}^{-2}$	102
IV.12	TGA curves of dopamine, polydopamine, imogolite and polymerized dopamine in presence of imogolite (PDA-Imo) before and after dialysis. The dotted line is calculated from the curves of polydopamine (75 %) and imogolite (25 %).	103
IV.13	AFM image of a sample that was irradiated at $162.5 \text{ mW} \cdot \text{cm}^{-2}$ for 1 h with $2 \text{ g} \cdot \text{L}^{-1}$ dopamine, $1 \text{ g} \cdot \text{L}^{-1}$ imogolite and 0.1 M acetate buffer after dialysis. Left: Height profile. Right: Phase shift.	104
IV.14	TEM image of a sample that was irradiated at $162.5 \text{ mW} \cdot \text{cm}^{-2}$ for 1 h with $2 \text{ g} \cdot \text{L}^{-1}$ dopamine, $1 \text{ g} \cdot \text{L}^{-1}$ imogolite and 0.1 M acetate buffer after dialysis. Scale bar is 200 nm.	104
IV.15	SAXS patterns of freeze dried samples in trehalose. Left: Imogolite and imogolite with polydopamine. Right: Polydopamine and trehalose alone.	105
A.1	SAXS pattern of the synthesized gold nanoparticles and a fit by polydisperse spheres.	I
A.2	TEM micrograph of the synthesized gold nanoparticles. Scale is 20 nm.	II
B.1	IMT device holder mounted on the interface to the SWING beamline.	III
B.2	Measurements for the PMMA device holder.	IV
D.1	Raw SAXS for the oil phase, water droplets and droplets that contain gold nanoparticles (AuNP).	XI
D.2	SAXS pattern at different reaction times along the microfluidic channel for the droplet phase.	XII
E.1	Deconvolution of the ^{27}Al MAS NMR spectrum of Sample A1.	XIV
E.2	Deconvolution of the ^{27}Al MAS NMR spectrum of Sample B.	XIV

F.1	Custom experimental setup to measure ion transport by conductivity made from glass.	XVI
F.2	Example for the temporal evolution of the measured conductivity after exchanging the water. The droplet on the interface is 0.1 M in $\text{Ce}(\text{NO}_3)_3$.XVII	
G.1	SAXS patterns of methyl imogolite dispersions before and after dialysis with a 100 kDa membrane.	XIX
H.1	AFM image of imogolite that was dialysed with a 8 kDa. Image is $1 \times 1 \mu\text{m}^2$.XXII	
H.2	AFM image of imogolite that was dialysed with a 100 kDa. Image is $1 \times 1 \mu\text{m}^2$	XXIII
H.3	AFM image of a sample after dopamine polymerization in the presence of imogolite and 0.1 M acetate buffer without dialysis. Image is $1 \times 1 \mu\text{m}^2$.XXIV	
H.4	AFM image of a sample after dopamine polymerization in the presence of imogolite and 0.1 M acetate buffer after dialysis. Image is $1 \times 1 \mu\text{m}^2$. XXV	

List of Tables

II.1	Generic functional groups in the OSTE+ pre-polymer.	12
II.2	Digital micrometer measurements for the thickness of a closed device and a device before closing. Probed positions can be seen in Figure II.20	36
II.3	Main components of an OSTE+ formulation from literature and its relative composition used to calculate the linear attenuation coefficient. ^[93,139,140] .	42
II.4	Generic repeat unit formulas and densities used in the calculation of the linear attenuation coefficient for the different materials.	43
III.1	Literature overview for the external surface modification of imogolite after synthesis.	68
III.2	Most popular anchoring groups for the modification of imogolite.	69
III.3	Investigated reaction conditions between imogolite and different phosphonic acids.	71
III.4	²⁷ Al MAS NMR distribution parameters.	79
IV.1	Dispersion behavior of an aqueous imogolite dispersion in different polar aprotic solvents.	97

Bibliography

- [1] **B. Libert and V. R. Franceschi.** "Oxalate in crop plants." *In Journal of Agricultural and Food Chemistry*, 35(6) 926–938. **1987.**
- [2] **V. R. Franceschi and P. A. Nakata.** "Calcium oxalate in plants: formation and function." *In Annual review of plant biology*, 56 41–71. **2005.**
- [3] **M. Daudon.** "Epidemiology of nephrolithiasis in France." *In Annales d'urologie*, 39(6) 209–231. **2005.**
- [4] **F. L. Coe, A. Evan and E. Worcester.** "Kidney stone disease." *In The Journal of clinical investigation*, 115(10) 2598–2608. **2005.**
- [5] **E. Rademacher and M. Harz.** "Oxalic acid for the control of varroosis in honey bee colonies – a review." *In Apidologie*, 37(1) 98–120. **2006.**
- [6] **C. W. Forsberg.** "Separation of Americium, Curium, and Trivalent Lanthanides from High-Level Wastes by Oxalate Precipitation: Experiments with Synthetic Waste Solutions." *In Nuclear Technology*, 49(2) 243–252. **1980.**
- [7] **P. M. Smith.** "High-Purity Rare Earth Oxides Produced via Precipitation Stripping." *In Metallurgical and Materials Transactions B*, 38(5) 763–768. **2007.**
- [8] **G. Borda, E. Brackx, L. Boisset, J. Duhamet and D. Ode.** "Use of a pulsed column contactor as a continuous oxalate precipitation reactor." *In Nuclear Engineering and Design*, 241(3) 809–814. **2011.**
- [9] **S. Charton, A. Kacem, A. Amokrane, G. Borda, F. Puel and J.-P. Klein.** "Actinides oxalate precipitation in emulsion modeling: From the drop scale to the industrial process: From the drop scale to the industrial process." *In Chemical Engineering Research & Design*, 91(4) 660–669. **2013.**

- [10] **K. Binnemans, P. T. Jones, B. Blanpain, T. van Gerven, Y. Yang, A. Walton and M. Buchert.** "Recycling of rare earths: a critical review." *In Journal of Cleaner Production*, 51 1–22. **2013**.
- [11] **J. D. Dunitz and J. Bernstein.** "Disappearing Polymorphs." *In Accounts of Chemical Research*, 28(4) 193–200. **1995**.
- [12] **S. R. Chemburkar, J. Bauer, K. Deming, H. Spiwek, K. Patel, J. Morris, R. Henry, S. Spanton, W. Dziki, W. Porter, J. Quick, P. Bauer, J. Donaubaue, B. A. Narayanan, M. Soldani, D. Riley and K. McFarland.** "Dealing with the Impact of Ritonavir Polymorphs on the Late Stages of Bulk Drug Process Development." *In Organic Process Research & Development*, 4(5) 413–417. **2000**.
- [13] **M. Kind.** "Colloidal aspects of precipitation processes." *In Chemical Engineering Science*, 57(20) 4287–4293. **2002**.
- [14] **J. J. de Yoreo, P. U. P. A. Gilbert, N. A. J. M. Sommerdijk, R. L. Penn, S. Whitelam, D. Joester, H. Zhang, J. D. Rimer, A. Navrotsky, J. F. Banfield, A. F. Wallace, F. M. Michel, F. C. Meldrum, H. Cölfen and P. M. Dove.** "CRYSTAL GROWTH. Crystallization by particle attachment in synthetic, biogenic, and geologic environments." *In Science*, 349(6247) aaa6760. **2015**.
- [15] **F. C. Meldrum and H. Cölfen.** "Controlling mineral morphologies and structures in biological and synthetic systems." *In Chemical Reviews*, 108(11) 4332–4432. **2008**.
- [16] **A. Dhall and W. Self.** "Cerium Oxide Nanoparticles: A Brief Review of Their Synthesis Methods and Biomedical Applications." *In Antioxidants (Basel, Switzerland)*, 7(8). **2018**.
- [17] **S. Sutherland-Harper, R. Taylor, J. Hobbs, S. Pimblott, R. Pattrick, M. Sarsfield, M. Denecke, F. Livens, N. Kaltsoyannis, B. Arey, L. Kovarik, M. Engelhard, J. Waters and C. Pearce.** "Surface speciation and interactions between adsorbed chloride and water on cerium dioxide." *In Journal of Solid State Chemistry*, 262 16–25. **2018**.
- [18] **C. T. Campbell and C. H. F. Peden.** "Chemistry. Oxygen vacancies and catalysis on ceria surfaces." *In Science*, 309(5735) 713–714. **2005**.
- [19] **W. Liu, L. Feng, C. Zhang, H. Yang, J. Guo, X. Liu, X. Zhang and Y. Yang.** "A facile hydrothermal synthesis of 3D flowerlike CeO₂ via a cerium oxalate precursor." *In Journal of Materials Chemistry A*, 1(23) 6942–6948. **2013**.

- [20] **Y. Altaş and H. Tel.** “Structural and thermal investigations on cerium oxalate and derived oxide powders for the preparation of (Th,Ce)O₂ pellets.” *In Journal of Nuclear Materials*, 298(3) 316–320. **2001.**
- [21] **V. Tyrpekl, P. Markova, M. Dopita, P. Brázda and M. A. Vacca.** “Cerium Oxalate Morphotypes: Synthesis and Conversion into Nanocrystalline Oxide.” *In Inorganic chemistry*, 58(15) 10 111–10 118. **2019.**
- [22] **W. Ollendorff and F. Weigel.** “The crystal structure of some lanthanide oxalate decahydrates, Ln₂(C₂O₄)₃·10H₂O, with Ln = La, Ce, Pr, and Nd.” *In Inorganic and Nuclear Chemistry Letters*, 5(4) 263–269. **1969.**
- [23] **M. Jehannin, S. Charton, S. Karpitschka, T. Zemb, H. Möhwald and H. Riegler.** “Periodic Precipitation Patterns during Coalescence of Reacting Sessile Droplets.” *In Langmuir*, 31(42) 11 484–11 490. **2015.**
- [24] **J.-B. Yu, Z.-G. Yang, Z.-H. Wang, T.-S. Tu, Z.-Q. Zhang, J.-Y. Li, Y.-B. Zhong and Z.-M. Ren.** “Synthesis of cerium oxalate hydrate by precipitation technique under external magnetic field.” *In Rare Metals*, 391(1–2) 43. **2017.**
- [25] **I. Rodríguez-Ruiz, S. Charton, D. Radajewski, T. Bizien and S. Teychené.** “Ultra-fast precipitation of transient amorphous cerium oxalate in concentrated nitric acid media.” *In CrystEngComm*, 20(24) 3302–3307. **2018.**
- [26] **M. Jehannin.** *About the role of physico-chemical properties and hydrodynamics on the progress of a precipitation reaction: the case of cerium oxalate particles produced during coalescence of drops.* PhD Thesis, Université de Montpellier, Potsdam University. **2015.**
- [27] **M. Jehannin, S. Charton, B. Corso, H. Mohwald, H. Riegler and T. Zemb.** “Structured solvent effects on precipitation.” *In Colloid and Polymer Science*, 295(10) 1817–1826. **2017.**
- [28] **Y. Vitry, S. Teychené, S. Charton, F. Lamadie and B. Biscans.** “Investigation of a microfluidic approach to study very high nucleation rates involved in precipitation processes.” *In Chemical Engineering Science*, 133 54–61. **2015.**
- [29] **R. Stehle, G. Goerigk, D. Wallacher, M. Ballauff and S. Seiffert.** “Small-angle X-ray scattering in droplet-based microfluidics.” *In Lab on a Chip*, 13(8) 1529–1537. **2013.**

- [30] **P. Picot, O. Taché, F. Malloggi, T. Coradin and A. Thill.** “Behaviour of hybrid inside/out Janus nanotubes at an oil/water interface. A route to self-assembled nanofluidics?” *In Faraday Discussions*, 191 391–406. **2016.**
- [31] **T. Narayanan, H. Wacklin, O. Konovalov and R. Lund.** “Recent applications of synchrotron radiation and neutrons in the study of soft matter.” *In Crystallography Reviews*, 23(3) 160–226. **2017.**
- [32] **T. Narayanan.** “Synchrotron Small-Angle X-Ray Scattering Studies of Colloidal Suspensions.” *In Applications of synchrotron light to scattering and diffraction in materials and life sciences* (Edited by **T. A. Ezquerra**), Lecture notes in physics, 0075-8450, 133–156 (Springer, Berlin). **2009.**
- [33] **P. Lindner and T. Zemb** (Editors). *Neutrons, X-rays and light: Scattering methods applied to soft condensed matter.* North-Holland delta series (Elsevier, Amsterdam and Oxford), new ed. edition. **2002.**
- [34] **O. Glatter and O. Kratky.** *Small angle x-ray scattering* (Academic Press, London). **1982.**
- [35] **T. Li, A. J. Senesi and B. Lee.** “Small Angle X-ray Scattering for Nanoparticle Research.” *In Chemical Reviews*, 116(18) 11 128–11 180. **2016.**
- [36] **T. Narayanan.** “Small-Angle Scattering.” *In Structure from diffraction methods* (Edited by **D. W. Bruce, D. O’Hare and R. I. Walton**), *Inorganic materials series*, volume 45, 259–324 (John Wiley et Sons Ltd, Chichester, West Sussex). **2014.**
- [37] **F. Hubert, F. Testard, A. Thill, Q. Kong, O. Tache and O. Spalla.** “Growth and Overgrowth of Concentrated Gold Nanorods: Time Resolved SAXS and XANES.” *In Crystal Growth & Design*, 12(3) 1548–1555. **2012.**
- [38] **T. Narayanan.** “High brilliance small-angle X-ray scattering applied to soft matter.” *In Current Opinion in Colloid & Interface Science*, 14(6) 409–415. **2009.**
- [39] **P. Panine, S. Finet, T. M. Weiss and T. Narayanan.** “Probing fast kinetics in complex fluids by combined rapid mixing and small-angle X-ray scattering.” *In Advances in Colloid and Interface Science*, 127(1) 9–18. **2006.**
- [40] **S. Schmolzer, D. Gräbner, M. Gradzielski and T. Narayanan.** “Millisecond-range time-resolved small-angle x-ray scattering studies of micellar transformations.” *In Physical Review Letters*, 88(25 Pt 1) 258 301. **2002.**

- [41] **B. Abécassis, F. Testard, O. Spalla and P. Barboux.** “Probing in situ the nucleation and growth of gold nanoparticles by small-angle X-ray scattering.” *In Nano Letters*, 7(6) 1723–1727. **2007.**
- [42] **B. Abécassis, C. Bouet, C. Garnero, D. Constantin, N. Lequeux, S. Ithurria, B. Dubertret, B. R. Pauw and D. Pontoni.** “Real-time in situ probing of high-temperature quantum dots solution synthesis.” *In Nano Letters*, 15(4) 2620–2626. **2015.**
- [43] **S. Saha, S. Springer, M. E. Schweinefuß, D. Pontoni, M. Wiebcke and K. Huber.** “Insight into Fast Nucleation and Growth of Zeolitic Imidazolate Framework-71 by In Situ Time-Resolved Light and X-ray Scattering Experiments.” *In Crystal Growth & Design*, 16(4) 2002–2010. **2016.**
- [44] **B. F. B. Silva.** “SAXS on a chip: from dynamics of phase transitions to alignment phenomena at interfaces studied with microfluidic devices.” *In Physical Chemistry Chemical Physics*, 19(35) 23 690–23 703. **2017.**
- [45] **S. A. Watkin, T. M. Ryan, A. G. Miller, V. M. Nock, F. G. Pearce and R. C. Dobson.** “Microfluidics for Small-Angle X-ray Scattering.” *In X-ray Scattering* (Edited by **A. E. Ares**), Ch. 04 (InTech, Rijeka). **2017.**
- [46] **A. Ghazal, J. P. Lafleur, K. Mortensen, J. P. Kutter, L. Arleth and G. V. Jensen.** “Recent advances in X-ray compatible microfluidics for applications in soft materials and life sciences.” *In Lab on a Chip*, 16(22) 4263–4295. **2016.**
- [47] **T. M. Squires and S. R. Quake.** “Microfluidics: Fluid physics at the nanoliter scale.” *In Reviews of Modern Physics*, 77(3) 977. **2005.**
- [48] **L. Pollack, M. W. Tate, A. C. Finnefrock, C. Kalidas, S. Trotter, N. C. Darnton, L. Lurio, R. H. Austin, C. A. Batt, S. M. Gruner and S. G. Mochrie.** “Time resolved collapse of a folding protein observed with small angle x-ray scattering.” *In Physical Review Letters*, 86(21) 4962–4965. **2001.**
- [49] **L. Pollack, M. W. Tate, N. C. Darnton, J. B. Knight, S. M. Gruner, W. A. Eaton and R. H. Austin.** “Compactness of the denatured state of a fast-folding protein measured by submillisecond small-angle x-ray scattering.” *In Proceedings of the National Academy of Sciences of the United States of America*, 96(18) 10 115–10 117. **1999.**

- [50] **J. B. Knight, A. Vishwanath, J. P. Brody and R. H. Austin.** “Hydrodynamic Focusing on a Silicon Chip: Mixing Nanoliters in Microseconds.” *In Physical Review Letters*, 80(17) 3863. **1998.**
- [51] **R. Graceffa, R. P. Nobrega, R. A. Barrea, S. V. Kathuria, S. Chakravarthy, O. Bilsel and T. C. Irving.** “Sub-millisecond time-resolved SAXS using a continuous-flow mixer and X-ray microbeam.” *In Journal of synchrotron radiation*, 20(Pt 6) 820–825. **2013.**
- [52] **S. Akiyama, S. Takahashi, T. Kimura, K. Ishimori, I. Morishima, Y. Nishikawa and T. Fujisawa.** “Conformational landscape of cytochrome c folding studied by microsecond-resolved small-angle x-ray scattering.” *In Proceedings of the National Academy of Sciences of the United States of America*, 99(3) 1329–1334. **2002.**
- [53] **A. D. Stroock, S. K. W. Dertinger, A. Ajdari, I. Mezic, H. A. Stone and G. M. Whitesides.** “Chaotic mixer for microchannels.” *In Science*, 295(5555) 647–651. **2002.**
- [54] **H. Song and R. F. Ismagilov.** “Millisecond kinetics on a microfluidic chip using nanoliters of reagents.” *In Journal of the American Chemical Society*, 125(47) 14 613–14 619. **2003.**
- [55] **H. Song, J. D. Tice and R. F. Ismagilov.** “A microfluidic system for controlling reaction networks in time.” *In Angewandte Chemie International Edition*, 42(7) 768–772. **2003.**
- [56] **B. Zheng, J. D. Tice, L. S. Roach and R. F. Ismagilov.** “A droplet-based, composite PDMS/glass capillary microfluidic system for evaluating protein crystallization conditions by microbatch and vapor-diffusion methods with on-chip X-ray diffraction.” *In Angewandte Chemie International Edition*, 43(19) 2508–2511. **2004.**
- [57] **N. Pham, D. Radajewski, A. Round, M. Brennich, P. Pernot, B. Biscans, F. Bonneté and S. Teychené.** “Coupling High Throughput Microfluidics and Small-Angle X-ray Scattering to Study Protein Crystallization from Solution.” *In Analytical Chemistry*, 89(4) 2282–2287. **2017.**
- [58] **I. Rodríguez-Ruiz, D. Radajewski, S. Charton, N. Phamvan, M. Brennich, P. Pernot, F. Bonneté and S. Teychené.** “Innovative High-Throughput SAXS

- Methodologies Based on Photonic Lab-on-a-Chip Sensors: Application to Macromolecular Studies: Application to Macromolecular Studies." *In Sensors (Basel)*, 17(6) 1266. **2017**.
- [59] **O. Saldanha, R. Graceffa, C. Y. J. Hémonnot, C. Ranke, G. Brehm, M. Liebi, B. Marmiroli, B. Weinhausen, M. Burghammer and S. Köster**. "Rapid Acquisition of X-Ray Scattering Data from Droplet-Encapsulated Protein Systems." *In ChemPhysChem*, 18(10) 1220–1223. **2017**.
- [60] **M. A. Levenstein, C. Anduix-Canto, Y.-Y. Kim, M. A. Holden, C. González Niño, D. C. Green, S. E. Foster, A. N. Kulak, L. Govada, N. E. Chayen, S. J. Day, C. C. Tang, B. Weinhausen, M. Burghammer, N. Kapur and F. C. Meldrum**. "Droplet Microfluidics XRD Identifies Effective Nucleating Agents for Calcium Carbonate." *In Advanced Functional Materials*, 114 1808172. **2019**.
- [61] **A. Merlin, J. Angly, L. Daubersies, C. Madeira, S. Schöder, J. Leng and J.-B. Salmon**. "Time-resolved microfocused small-angle X-ray scattering investigation of the microfluidic concentration of charged nanoparticles." *In The European Physical Journal E*, 34(6) 58. **2011**.
- [62] **R. Barrett, M. Faucon, J. Lopez, G. Cristobal, F. Destremaut, A. Dodge, P. Guillot, P. Laval, C. Masselon and J.-B. Salmon**. "X-ray microfocussing combined with microfluidics for on-chip X-ray scattering measurements." *In Lab on a Chip*, 6(4) 494–499. **2006**.
- [63] **A. Ghazal, M. Gontsarik, J. P. Kutter, J. P. Lafleur, D. Ahmadvand, A. Labrador, S. Salentinig and A. Yaghmur**. "Microfluidic Platform for the Continuous Production and Characterization of Multilamellar Vesicles: A Synchrotron Small-Angle X-ray Scattering (SAXS) Study." *In The journal of physical chemistry letters*, 8(1) 73–79. **2017**.
- [64] **A. Ghazal, M. Gontsarik, J. P. Kutter, J. P. Lafleur, A. Labrador, K. Mortensen and A. Yaghmur**. "Direct monitoring of calcium-triggered phase transitions in cubosomes using small-angle X-ray scattering combined with microfluidics." *In Journal of Applied Crystallography*, 49(6) 2005–2014. **2016**.
- [65] **V. Lutz-Bueno, J. Zhao, R. Mezzenga, T. Pfohl, P. Fischer and M. Liebi**. "Scanning-SAXS of microfluidic flows: nanostructural mapping of soft matter." *In Lab on a Chip*, 16(20) 4028–4035. **2016**.

- [66] **S. With, M. Trebbin, C. B. A. Bartz, C. Neuber, M. Dulle, S. Yu, S. V. Roth, H.-W. Schmidt and S. Förster.** “Fast diffusion-limited lyotropic phase transitions studied in situ using continuous flow microfluidics/microfocus-SAXS.” *In Langmuir*, 30(42) 12 494–12 502. **2014.**
- [67] **K. N. Toft, B. Vestergaard, S. S. Nielsen, D. Snakenborg, M. G. Jeppesen, J. K. Jacobsen, L. Arleth and J. P. Kutter.** “High-throughput small angle X-ray scattering from proteins in solution using a microfluidic front-end.” *In Analytical chemistry*, 80(10) 3648–3654. **2008.**
- [68] **J. P. Lafleur, D. Snakenborg, S. S. Nielsen, M. Møller, K. N. Toft, A. Menzel, J. K. Jacobsen, B. Vestergaard, L. Arleth and J. P. Kutter.** “Automated microfluidic sample-preparation platform for high-throughput structural investigation of proteins by small-angle X-ray scattering.” *In Journal of Applied Crystallography*, 44(5) 1090–1099. **2011.**
- [69] **T. D. Murray, A. Y. Lyubimov, C. M. Ogata, H. Vo, M. Uervirojnangkoorn, A. T. Brunger and J. M. Berger.** “A high-transparency, micro-patternable chip for X-ray diffraction analysis of microcrystals under native growth conditions.” *In Acta crystallographica. Section D, Biological crystallography*, 71(Pt 10) 1987–1997. **2015.**
- [70] **O. Saldanha, M. E. Brennich, M. Burghammer, H. Herrmann and S. Köster.** “The filament forming reactions of vimentin tetramers studied in a serial-inlet microflow device by small angle x-ray scattering.” *In Biomicrofluidics*, 10(2) 024 108. **2016.**
- [71] **M. E. Brennich, J.-F. Nolting, C. Dammann, B. Nöding, S. Bauch, H. Herrmann, T. Pfohl and S. Köster.** “Dynamics of intermediate filament assembly followed in micro-flow by small angle X-ray scattering.” *In Lab on a Chip*, 11(4) 708–716. **2011.**
- [72] **M. Denz, G. Brehm, C. Y. J. Hémonnot, H. Spears, A. Wittmeier, C. Cassini, O. Saldanha, E. Perego, A. Diaz, M. Burghammer and S. Köster.** “Cyclic olefin copolymer as an X-ray compatible material for microfluidic devices.” *In Lab on a Chip*, 18(1) 171–178. **2017.**
- [73] **I. Rodriguez-Ruiz, S. Charton, D. Radajewski, T. Bizien and S. Teychené.** “Unstable amorphous cerium oxalate precipitation in concentrated HNO₃ media.” *In*

Acta Crystallographica Section A Foundations and Advances, 73(a2) C350–C350. **2017**.

- [74] **D. Radajewski**. *Etudes de nucléation de protéines à l'aide de dispositifs expérimentaux microfluidiques*. PhD, Institut National Polytechnique de Toulouse, Toulouse. **2017**.
- [75] **D. Sticker, S. Lechner, C. Jungreuthmayer, J. Zanghellini and P. Ertl**. “Microfluidic Migration and Wound Healing Assay Based on Mechanically Induced Injuries of Defined and Highly Reproducible Areas.” *In Analytical chemistry*, 89(4) 2326–2333. **2017**.
- [76] **A. Martin, S. Teychene, S. Camy and J. Aubin**. “Fast and inexpensive method for the fabrication of transparent pressure-resistant microfluidic chips.” *In Microfluidics and Nanofluidics*, 20(6) 92. **2016**.
- [77] **N. van Pham**. *Development of high throughput microfluidic platforms for the measurement of the protein solution thermodynamic properties*. PhD, Université de Toulouse, Toulouse. **2016**.
- [78] **N. Sandström, R. Z. Shafagh, A. Vastesson, C. F. Carlborg, W. van der Wijngaart and T. Haraldsson**. “Reaction injection molding and direct covalent bonding of OSTE+ polymer microfluidic devices.” *In Journal of Micromechanics and Micro-engineering*, 25(7) 075 002. **2015**.
- [79] **D. Sticker, M. Rothbauer, S. Lechner, M.-T. Hehenberger and P. Ertl**. “Multi-layered, membrane-integrated microfluidics based on replica molding of a thiol-ene epoxy thermoset for organ-on-a-chip applications.” *In Lab on a Chip*, 15(24) 4542–4554. **2015**.
- [80] **L. Capretto, W. Cheng, M. Hill and X. Zhang**. “Micromixing within microfluidic devices.” *In Microfluidics: Technologies and Applications* (Edited by **B. Lin**), volume 304, 27–68 (Springer Berlin Heidelberg, Berlin and Heidelberg). **2011**.
- [81] **H. Song, M. R. Bringer, J. D. Tice, C. J. Gerdtts and R. F. Ismagilov**. “Experimental test of scaling of mixing by chaotic advection in droplets moving through microfluidic channels.” *In Applied Physics Letters*, 83(12) 4664–4666. **2003**.
- [82] **R. Dreyfus, P. Tabeling and H. Willaime**. “Ordered and disordered patterns in two-phase flows in microchannels.” *In Physical Review Letters*, 90(14) 144 505. **2003**.

- [83] **H. Becker and C. Gärtner.** “Polymer microfabrication technologies for microfluidic systems.” *In Analytical and bioanalytical chemistry*, 390(1) 89–111. **2008.**
- [84] **P. N. Nge, C. I. Rogers and A. T. Woolley.** “Advances in microfluidic materials, functions, integration, and applications.” *In Chemical Reviews*, 113(4) 2550–2583. **2013.**
- [85] **K. Ren, J. Zhou and H. Wu.** “Materials for microfluidic chip fabrication.” *In Accounts of Chemical Research*, 46(11) 2396–2406. **2013.**
- [86] **D. R. Reyes, D. Iossifidis, P.-A. Auroux and A. Manz.** “Micro total analysis systems. 1. Introduction, theory, and technology.” *In Analytical Chemistry*, 74(12) 2623–2636. **2002.**
- [87] **A. Berg, W. Olthuis and P. Bergveld** (Editors). *Micro Total Analysis Systems 2000: Proceedings of the μ TAS 2000 Symposium, held in Enschede, The Netherlands, 14–18 May 2000* (Springer Netherlands, Dordrecht and s.l.). **2000.**
- [88] **Y. Xia and G. M. Whitesides.** “Soft Lithography.” *In Angewandte Chemie International Edition*, 37(5) 550–575. **1998.**
- [89] **J. C. McDonald and G. M. Whitesides.** “Poly(dimethylsiloxane) as a Material for Fabricating Microfluidic Devices.” *In Accounts of Chemical Research*, 35(7) 491–499. **2002.**
- [90] **J. Friend and L. Yeo.** “Fabrication of microfluidic devices using polydimethylsiloxane.” *In Biomicrofluidics*, 4(2). **2010.**
- [91] **F. Saharil, F. Forsberg, Y. Liu, P. Bettotti, N. Kumar, F. Niklaus, T. Haraldsson, W. van der Wijngaart and K. B. Gylfason.** “Dry adhesive bonding of nanoporous inorganic membranes to microfluidic devices using the OSTE(+) dual-cure polymer.” *In Journal of Micromechanics and Microengineering*, 23(2) 025 021. **2013.**
- [92] **C. F. Carlborg, T. Haraldsson, K. Öberg, M. Malkoch and W. van der Wijngaart.** “Beyond PDMS: off-stoichiometry thiol-ene (OSTE) based soft lithography for rapid prototyping of microfluidic devices: off-stoichiometry thiol-ene (OSTE) based soft lithography for rapid prototyping of microfluidic devices.” *In Lab on a Chip*, 11(18) 3136–3147. **2011.**
- [93] **C. F. Carlborg, A. Vastesson, Y. Liu, W. van der Wijngaart, M. Johansson and T. Haraldsson.** “Functional off-stoichiometry thiol-ene-epoxy thermosets featuring

- temporally controlled curing stages via an UV/UV dual cure process." *In Journal of Polymer Science Part A: Polymer Chemistry*, 52(18) 2604–2615. **2014**.
- [94] **C. E. Hoyle and C. N. Bowman**. "Thiol-ene click chemistry." *In Angewandte Chemie International Edition*, 49(9) 1540–1573. **2010**.
- [95] **F. Carlborg, F. Moraga, F. Saharil, W. van der Wijngaart and T. Haraldsson**. "Rapid permanent hydrophilic and hydrophobic patterning of polymer surfaces via off-stoichiometry thiol-ene (OSTE) photografting." *In Proceedings of The Sixteenth International Conference on Miniaturized Systems for Chemistry and Life Sciences (μ TAS 2012): μ TAS 2012* (Edited by **T. Fujii, A. Hibara, S. Takeuchi and T. Fukuba**), 677–679 (Chemical and Biological Microsystems Society). **2012**.
- [96] **L. Shang, Y. Cheng and Y. Zhao**. "Emerging Droplet Microfluidics." *In Chemical Reviews*, 117(12) 7964–8040. **2017**.
- [97] **S. L. Anna**. "Droplets and Bubbles in Microfluidic Devices." *In Annual Review of Fluid Mechanics*, 48(1) 285–309. **2016**.
- [98] **P. Zhu and L. Wang**. "Passive and active droplet generation with microfluidics: a review: a review." *In Lab on a Chip*, 17(1) 34–75. **2016**.
- [99] **Z. Z. Chong, S. H. Tan, A. M. Gañán-Calvo, S. B. Tor, N. H. Loh and N.-T. Nguyen**. "Active droplet generation in microfluidics." *In Lab on a Chip*, 16(1) 35–58. **2015**.
- [100] **R. Seemann, M. Brinkmann, T. Pfohl and S. Herminghaus**. "Droplet based microfluidics." *In Reports on progress in physics. Physical Society (Great Britain)*, 75(1) 016 601. **2012**.
- [101] **C. N. Baroud, F. Gallaire and R. Dangla**. "Dynamics of microfluidic droplets." *In Lab on a Chip*, 10(16) 2032–2045. **2010**.
- [102] **S.-Y. Teh, R. Lin, L.-H. Hung and A. P. Lee**. "Droplet microfluidics." *In Lab on a Chip*, 8(2) 198–220. **2008**.
- [103] **G. F. Christopher and S. L. Anna**. "Microfluidic methods for generating continuous droplet streams." *In Journal of Physics D-Applied Physics*, 40(19) R319–R336. **2007**.
- [104] **J. N. Lee, C. Park and G. M. Whitesides**. "Solvent compatibility of poly(dimethylsiloxane)-based microfluidic devices." *In Analytical Chemistry*, 75(23) 6544–6554. **2003**.

- [105] **J. H. Xu, S. W. Li, J. Tan, Y. J. Wang and G. S. Luo.** "Controllable preparation of monodisperse O/W and W/O emulsions in the same microfluidic device." *In Langmuir*, 22(19) 7943–7946. **2006.**
- [106] **J.-C. Baret.** "Surfactants in droplet-based microfluidics." *In Lab on a Chip*, 12(3) 422–433. **2012.**
- [107] **Z. Nie, J. I. Park, W. Li, S. A. F. Bon and E. Kumacheva.** "An "inside-out" microfluidic approach to monodisperse emulsions stabilized by solid particles." *In Journal of the American Chemical Society*, 130(49) 16 508–16 509. **2008.**
- [108] **L. S. Roach, H. Song and R. F. Ismagilov.** "Controlling nonspecific protein adsorption in a plug-based microfluidic system by controlling interfacial chemistry using fluorinated-phase surfactants." *In Analytical Chemistry*, 77(3) 785–796. **2005.**
- [109] **T. Thorsen, R. W. Roberts, F. H. Arnold and S. R. Quake.** "Dynamic pattern formation in a vesicle-generating microfluidic device." *In Physical Review Letters*, 86(18) 4163–4166. **2001.**
- [110] **P. Guillot and A. Colin.** "Stability of parallel flows in a microchannel after a T junction." *In Physical Review E*, 72(6) 066 301. **2005.**
- [111] **M. de MENECH, P. Garstecki, F. JOUSSE and H. A. STONE.** "Transition from squeezing to dripping in a microfluidic T-shaped junction." *In Journal of Fluid Mechanics*, 595 141–161. **2008.**
- [112] **J. H. Xu, S. W. Li, J. Tan, Y. J. Wang and G. S. Luo.** "Preparation of highly monodisperse droplet in a T-junction microfluidic device." *In AIChE Journal*, 52(9) 3005–3010. **2006.**
- [113] **D. T. Papageorgiou.** "On the breakup of viscous liquid threads." *In Physics of Fluids*, 7(7) 1529–1544. **1995.**
- [114] **B. R. Pauw.** "Everything SAXS: small-angle scattering pattern collection and correction." *In Journal of Physics: Condensed Matter*, 25(38) 383 201. **2013.**
- [115] **D. S. Sivia.** *Elementary Scattering Theory: For X-ray and neutron users* (Oxford University Press). **2011.**
- [116] **T. Narayanan.** "Synchrotron Small-Angle X-Ray Scattering." *In Soft matter characterization* (Edited by **R. Borsali and R. Pecora**), 899–952 (Springer, New York and London). **2008-**.

- [117] **S. Seltzer**. “X-ray Form Factor, Attenuation and Scattering Tables, NIST Standard Reference Database 66.”
- [118] **T. Narayanan, O. Diat and P. Bösecke**. “SAXS and USAXS on the high brilliance beamline at the ESRF.” *In Nuclear Instruments and Methods in Physics Research Section A: Accelerators, Spectrometers, Detectors and Associated Equipment*, 467-468 1005–1009. **2001**.
- [119] **T. C. Huang, H. Toraya, T. N. Blanton and Y. Wu**. “X-ray powder diffraction analysis of silver behenate, a possible low-angle diffraction standard.” *In Journal of Applied Crystallography*, 26(2) 180–184. **1993**.
- [120] **G. W. Brindley**. “Long-Spacing Organics for Calibrating Long Spacings of Interstratified Clay Minerals.” *In Clays and Clay Minerals*, 29(1) 67–68. **1981**.
- [121] **O. Taché, S. Rouzière, P. Joly, M. Amara, B. Fleury, A. Thill, P. Launois, O. Spalla and B. Abécassis**. “MOMAC: a SAXS/WAXS laboratory instrument dedicated to nanomaterials.” *In Journal of Applied Crystallography*, 49(5) 1624–1631. **2016**.
- [122] **D. Orthaber, A. Bergmann and O. Glatter**. “SAXS experiments on absolute scale with Kratky systems using water as a secondary standard.” *In Journal of Applied Crystallography*, 33(2) 218–225. **2000**.
- [123] **L. B. Shaffer and R. W. Hendricks**. “Calibration of polyethylene (lupolen) as a wavelength-independent absolute intensity standard.” *In Journal of Applied Crystallography*, 7(2) 159–163. **1974**.
- [124] **F. Zhang, J. Ilavsky, G. G. Long, J. P. G. Quintana, A. J. Allen and P. R. Jemian**. “Glassy Carbon as an Absolute Intensity Calibration Standard for Small-Angle Scattering.” *In Metallurgical and Materials Transactions A*, 41(5) 1151–1158. **2010**.
- [125] **T. P. Russell, J. S. Lin, S. Spooner and G. D. Wignall**. “Intercalibration of small-angle X-ray and neutron scattering data.” *In Journal of Applied Crystallography*, 21(6) 629–638. **1988**.
- [126] **S. K. Sivaraman, S. Kumar and V. Santhanam**. “Monodisperse sub-10 nm gold nanoparticles by reversing the order of addition in Turkevich method—the role of chloroauric acid.” *In Journal of colloid and interface science*, 361(2) 543–547. **2011**.

- [127] **T. Schoonjans, A. Brunetti, B. Golosio, M. Sanchez del Rio, V. A. Solé, C. Ferrero and L. Vincze.** “The xraylib library for X-ray–matter interactions. Recent developments.” *In Spectrochimica Acta Part B: Atomic Spectroscopy*, 66(11-12) 776–784. **2011.**
- [128] **G. Ashiotis, A. Deschildre, Z. Nawaz, J. P. Wright, D. Karkoulis, F. E. Picca and J. Kieffer.** “The fast azimuthal integration Python library: pyFAI.” *In Journal of Applied Crystallography*, 48(Pt 2) 510–519. **2015.**
- [129] **D. Bartolo, G. Degré, P. Nghe and V. Studer.** “Microfluidic stickers.” *In Lab on a Chip*, 8(2) 274–279. **2008.**
- [130] **L. El Fissi, R. Fernández, P. García, M. Calero, J. V. García, Y. Jiménez, A. Arnau and L. A. Francis.** “OSTEMER polymer as a rapid packaging of electronics and microfluidic system on PCB.” *In Sensors and Actuators A: Physical*, 285 511–518. **2019.**
- [131] **D. J. Harrison, A. van den Berg, P. Galambos and F. K. Forster** (Editors). *Micro-Fluidic Diffusion Coefficient Measurement: Micro Total Analysis Systems '98* (Springer Netherlands). **1998.**
- [132] **F. Martelli, S. Abadie, J.-P. Simonin, R. Vuilleumier and R. Spezia.** “Lanthanoids(III) and actinoids(III) in water: Diffusion coefficients and hydration enthalpies from polarizable molecular dynamics simulations.” *In Pure and Applied Chemistry*, 85(1) 237–246. **2012.**
- [133] **J. Wang, J. Wang, L. Feng and T. Lin.** “Fluid mixing in droplet-based microfluidics with a serpentine microchannel.” *In RSC Advances*, 5(126) 104 138–104 144. **2015.**
- [134] **J. D. Tice, H. Song, A. D. Lyon and R. F. Ismagilov.** “Formation of Droplets and Mixing in Multiphase Microfluidics at Low Values of the Reynolds and the Capillary Numbers.” *In Langmuir*, 19(22) 9127–9133. **2003.**
- [135] **A. R. Thiam, N. Bremond and J. Bibette.** “Breaking of an Emulsion under an ac Electric Field.” *In Physical Review Letters*, 102(18) 188 304. **2009.**
- [136] **J. I. O. Masson.** “XI.—The solubility of electrolytes in aqueous solutions. Part II. Solubility of oxalic acid in other acids.” *In Journal of the Chemical Society, Transactions*, 101(0) 103–108. **1912.**

- [137] **J. R. Rumble**. *CRC handbook of chemistry and physics: A ready-reference book of chemical and physical data* (CRC Press, Boca Raton, Fla.), 100th edition. **2019**.
- [138] **I. Rodríguez-Ruiz, S. Teychené, Y. Vitry, B. Biscans and S. Charton**. “Thermodynamic modeling of neodymium and cerium oxalates reactive precipitation in concentrated nitric acid media.” *In Chemical Engineering Science*, 183 20–25. **2018**.
- [139] **Z. Yassin**. *Characterization of OSTE-based polymers for acoustofluidic applications*. Master’s Thesis, Royal Institute of Technology, Stockholm, Sweden. **2017**.
- [140] **F. Saharil, K. B. Gylfason, Y. Liu, T. Haraldsson, P. Bettotti, N. Kumar and W. van der Wijngaart**. “Dry transfer bonding of porous silicon membranes to OSTE(+) polymer microfluidic devices.” *In MEMS 2012*, 232–234 ([IEEE], [Piscataway, N.J.]). **2012**.
- [141] **A. Huerre, O. Theodoly, A. M. Leshansky, M.-P. Valignat, I. Cantat and M.-C. Jullien**. “Droplets in Microchannels: Dynamical Properties of the Lubrication Film.” *In Physical Review Letters*, 115(6) 064 501. **2015**.
- [142] **I. Liascukiene, S. Charton and F. Testard**. *In preparation*.
- [143] **T. Lange, T. Charpentier, F. Gobeaux, S. Charton, F. Testard and A. Thill**. “Partial Transformation of Imogolite by Decylphosphonic Acid Yields an Interface Active Composite Material.” *In Langmuir*, 35(11) 4068–4076. **2019**.
- [144] **W. Ramsden**. “Separation of solids in the surface-layers of solutions and ‘suspensions’ (observations on surface-membranes, bubbles, emulsions, and mechanical coagulation).—Preliminary account.” *In Proceedings of the Royal Society of London*, 72(477-486) 156–164. **1904**.
- [145] **S. U. Pickering**. “CXCVI.—Emulsions.” *In Journal of the Chemical Society, Transactions*, 91(0) 2001–2021. **1907**.
- [146] **B. P. Binks and S. O. Lumsdon**. “Influence of Particle Wettability on the Type and Stability of Surfactant-Free Emulsions †.” *In Langmuir*, 16(23) 8622–8631. **2000**.
- [147] **R. von Klitzing, D. Stehl, T. Pogrzeba, R. Schomäcker, R. Minullina, A. Panchal, S. Konnova, R. Fakhrullin, J. Koetz, H. Möhwald and Y. Lvov**. “Halloysites Stabilized Emulsions for Hydroformylation of Long Chain Olefins.” *In Advanced Materials Interfaces*, 4(1) 1600 435. **2017**.

- [148] **N. Yoshinaga and S. Aomine.** "Imogolite in some ando soils." *In Soil Science and Plant Nutrition*, 8(3) 22–29. **1962.**
- [149] **P. D. G. Cradwick, V. C. Farmer, J. D. Russell, C. R. Masson, K. Wada and N. Yoshinaga.** "Imogolite, a Hydrated Aluminium Silicate of Tubular Structure." *In Nature Physical Science*, 240(104) 187–189. **1972.**
- [150] **V. C. Farmer, A. R. Fraser and J. M. Tait.** "Synthesis of imogolite: a tubular aluminium silicate polymer: a tubular aluminium silicate polymer." *In Journal of the Chemical Society, Chemical Communications*, (13) 462. **1977.**
- [151] **S. Wada.** "Imogolite Synthesis at 25-Degrees-C." *In Clays and Clay Minerals*, 35(5) 379–384. **1987.**
- [152] **B. Bonelli, I. Bottero, N. Ballarini, S. Passeri, F. Cavani and E. Garrone.** "IR spectroscopic and catalytic characterization of the acidity of imogolite-based systems." *In Journal of Catalysis*, 264(1) 15–30. **2009.**
- [153] **G. I. Yucelen, D.-Y. Kang, R. C. Guerrero-Ferreira, E. R. Wright, H. W. Beckham and S. Nair.** "Shaping single-walled metal oxide nanotubes from precursors of controlled curvature." *In Nano Letters*, 12(2) 827–832. **2012.**
- [154] **S. Konduri, S. Mukherjee and S. Nair.** "Strain energy minimum and vibrational properties of single-walled aluminosilicate nanotubes." *In Physical Review B*, 74(3) 033401. **2006.**
- [155] **K. J. D. MacKenzie, M. E. Bowden, I. W. M. Brown and R. H. Meinhold.** "Structure and thermal transformations of imogolite studied by ²⁹Si and ²⁷Al high-resolution solid-state nuclear magnetic resonance." *In Clays and Clay Minerals*, 37(4) 317–324. **1989.**
- [156] **Y. Liao, P. Picot, M. Lainé, J.-B. Brubach, P. Roy, A. Thill and S. Le Caër.** "Tuning the properties of confined water in standard and hybrid nanotubes: An infrared spectroscopic study." *In Nano Research*, 11(9) 4759–4773. **2018.**
- [157] **H. Lee, Y. Jeon, Y. Lee, S. U. Lee, A. Takahara and D. Sohn.** "Thermodynamic Control of Diameter-Modulated Aluminosilicate Nanotubes." *In The Journal of Physical Chemistry C*, 118(15) 8148–8152. **2014.**
- [158] **S.-I. Wada.** "Effects of Substitution of Germanium for Silicon in Imogolite." *In Clays and Clay Minerals*, 30(2) 123–128. **1982.**

- [159] **I. Bottero, B. Bonelli, S. E. Ashbrook, P. A. Wright, W. Zhou, M. Tagliabue, M. Armandi and E. Garrone.** “Synthesis and characterization of hybrid organic/inorganic nanotubes of the imogolite type and their behaviour towards methane adsorption.” *In Physical Chemistry Chemical Physics*, 13(2) 744–750. **2011.**
- [160] **E. Belorizky, P. H. Fries, A. Guillermo and O. Poncelet.** “Almost ideal 1D water diffusion in imogolite nanotubes evidenced by NMR relaxometry.” *In ChemPhysChem*, 11(9) 2021–2026. **2010.**
- [161] **G. N. B. Baroña, J. Lim, M. Choi and B. Jung.** “Interfacial polymerization of polyamide-aluminosilicate SWNT nanocomposite membranes for reverse osmosis.” *In Desalination*, 325 138–147. **2013.**
- [162] **K. H. Liou, D. Y. Kang and L. C. Lin.** “Investigating the Potential of Single-Walled Aluminosilicate Nanotubes in Water Desalination.” *In ChemPhysChem*, 18(2) 179–183. **2017.**
- [163] **K. Yamamoto, H. Otsuka and A. Takahara.** “Preparation of Novel Polymer Hybrids from Imogolite Nanofiber.” *In Polymer Journal*, 39(1) 1–15. **2007.**
- [164] **K. Yamamoto, H. Otsuka, S.-I. Wada, D. Sohn and A. Takahara.** “Preparation and properties of [poly(methyl methacrylate)/imogolite] hybrid via surface modification using phosphoric acid ester.” *In Polymer*, 46(26) 12 386–12 392. **2005.**
- [165] **K. Yamamoto, H. Otsuka, S.-I. Wada, D. Sohn and A. Takahara.** “Transparent polymer nanohybrid prepared by in situ synthesis of aluminosilicate nanofibers in poly(vinyl alcohol) solution.” *In Soft Matter*, 1(5) 372–377. **2005.**
- [166] **K. Yamamoto, H. Otsuka, A. Takahara and S.-I. Wada.** “Preparation of a novel (polymer/inorganic nanofiber) composite through surface modification of natural aluminosilicate nanofiber.” *In Journal of Adhesion*, 78(7) 591–602. **2002.**
- [167] **L. M. Johnson and T. J. Pinnavaia.** “Hydrolysis of (γ -aminopropyl)triethoxysilane-silylated imogolite and formation of a silylated tubular silicate-layered silicate nanocomposite.” *In Langmuir*, 7(11) 2636–2641. **1991.**
- [168] **L. M. Johnson and T. J. Pinnavaia.** “Silylation of a tubular aluminosilicate polymer (imogolite) by reaction with hydrolyzed (γ -aminopropyl)triethoxysilane.” *In Langmuir*, 6(2) 307–311. **1990.**

- [169] **J. Guilment, D. Martin and O. Poncelet.** “Hybrid organic-inorganic materials designed to clean wash water in photographic processing: Genesis of a sol-gel industrial product: the Kodak Water Saving Treatment System.” *In MRS Proceedings*, 726 Q6.55. **2002.**
- [170] **X. Qi, H. Yoon, S.-H. Lee, J. Yoon and S.-J. Kim.** “Surface-modified imogolite by 3-APS–OsO₄ complex: Synthesis, characterization and its application in the dihydroxylation of olefins: Synthesis, characterization and its application in the dihydroxylation of olefins.” *In Journal of Industrial and Engineering Chemistry*, 14(1) 136–141. **2008.**
- [171] **D. L. Guerra, A. C. Batista, R. R. Viana and C. Airoidi.** “Adsorption of rubidium on raw and MTZ- and MBI-imogolite hybrid surfaces: An evidence of the chelate effect.” *In Desalination*, 275(1) 107–117. **2011.**
- [172] **D. L. Guerra, A. C. Batista, R. R. Viana and C. Airoidi.** “Adsorption of methylene blue on raw and MTZ/imogolite hybrid surfaces: effect of concentration and calorimetric investigation: effect of concentration and calorimetric investigation.” *In Journal of Hazardous Materials*, 183(1-3) 81–86. **2010.**
- [173] **C. Zanzottera, A. Vicente, E. Celasco, C. Fernandez, E. Garrone and B. Bonelli.** “Physico-Chemical Properties of Imogolite Nanotubes Functionalized on Both External and Internal Surfaces.” *In Journal of Physical Chemistry C*, 116(13) 7499–7506. **2012.**
- [174] **W. Ma, J. Kim, H. Otsuka and A. Takahara.** “Surface Modification of Individual Imogolite Nanotubes with Alkyl Phosphate from an Aqueous Solution.” *In Chemistry Letters*, 40(2) 159–161. **2011.**
- [175] **W. Ma, H. Otsuka and A. Takahara.** “Poly(methyl methacrylate) grafted imogolite nanotubes prepared through surface-initiated ARGET ATRP.” *In Chemical Communications*, 47(20) 5813–5815. **2011.**
- [176] **W. Ma, H. Otsuka and A. Takahara.** “Preparation and properties of PVC/PMMA-g-imogolite nanohybrid via surface-initiated radical polymerization.” *In Polymer*, 52(24) 5543–5550. **2011.**
- [177] **K. Yamamoto, H. Otsuka, S.-I. Wada and A. Takahara.** “Surface Modification of Aluminosilicate Nanofiber “Imogolite”.” *In Chemistry Letters*, 30(11) 1162–1163. **2001.**

- [178] **S. Park, Y. Lee, B. Kim, J. Lee, Y. Jeong, J. Noh, A. Takahara and D. Sohn.** “Two-dimensional alignment of imogolite on a solid surface.” *In Chemical Communications*, (28) 2917–2919. **2007.**
- [179] **B. H. Bac, Y. Song, M. H. Kim, Y.-B. Lee and I. M. Kang.** “Surface-modified aluminogermanate nanotube by OPA: Synthesis and characterization: Synthesis and characterization.” *In Inorganic Chemistry Communications*, 12(10) 1045–1048. **2009.**
- [180] **W. O. Yah, A. Irie, N. Jiravanichanun, H. Otsuka and A. Takahara.** “Molecular Aggregation State and Electrical Properties of Terthiophenes/Imogolite Nanohybrids.” *In Bulletin of the Chemical Society of Japan*, 84(9) 893–902. **2011.**
- [181] **W. O. Yah, A. Irie, H. Otsuka, S. Sasaki, N. Yagi, M. Sato, T. Koganezawa and A. Takahara.** “Molecular Aggregation States of Imogolite/P3HT Nanofiber Hybrid.” *In Journal of Physics: Conference Series*, 272(1) 012 021. **2011.**
- [182] **M. Li and J. A. Brant.** “Dispersing surface-modified imogolite nanotubes in polar and non-polar solvents.” *In Journal of Nanoparticle Research*, 20(2) 19. **2018.**
- [183] **M. Li and J. A. Brant.** “Synthesis of polyamide thin-film nanocomposite membranes using surface modified imogolite nanotubes.” *In Journal of Membrane Science*, 563 664–675. **2018.**
- [184] **K. Shikinaka, A. Abe and K. Shigehara.** “Nanohybrid film consisted of hydrophobized imogolite and various aliphatic polyesters.” *In Polymer*, 68 279–283. **2015.**
- [185] **S. Miura, N. Teramoto and M. Shibata.** “Nanocomposites composed of poly(epsilon-caprolactone) and oligocaprolactone-modified imogolite utilizing biomimetic chelating method.” *In Journal of Polymer Research*, 23(2). **2016.**
- [186] **H. Lee, J. Ryu, D. Kim, Y. Joo, S. U. Lee and D. Sohn.** “Preparation of an imogolite/poly(acrylic acid) hybrid gel.” *In Journal of Colloid and Interface Science*, 406 165–171. **2013.**
- [187] **J. Ryu, H. Kim, J. Kim, J. Ko and D. Sohn.** “Dynamic behavior of hybrid poly(acrylic acid) gel prepared by γ -ray irradiated imogolite.” *In Colloids and Surfaces A: Physicochemical and Engineering Aspects*, 535 166–174. **2017.**
- [188] **A. Stein, B. J. Melde and R. C. Schroden.** “Hybrid Inorganic-Organic Mesoporous Silicates—Nanoscope Reactors Coming of Age.” *In Advanced Materials*, 12(19) 1403–1419. **2000.**

- [189] **N. Impens, P. van der Voort and E. Vansant.** "Silylation of micro-, meso- and non-porous oxides: a review." *In Microporous and Mesoporous Materials*, 28(2) 217–232. **1999.**
- [190] **E. P. Plueddemann.** *Silane Coupling Agents* (Springer US, Boston, MA). **1991.**
- [191] **P. H. Mutin, G. Guerrero and A. Vioux.** "Hybrid materials from organophosphorus coupling molecules." *In Journal of Materials Chemistry*, 15(35-36) 3761–3768. **2005.**
- [192] **R. L. Parfitt.** "Adsorption of Phosphate on Imogolite." *In Clays and Clay Minerals*, 22(5–6) 455–456. **1974.**
- [193] **Gardolinski, J. E. F. C., G. Lagaly and M. Czank.** "On the destruction of kaolinite and gibbsite by phenylphosphonic, phenylphosphinic and phenylarsonic acids: evidence for the formation of new Al compounds." *In Clay Minerals*, 39(04) 391–404. **2004.**
- [194] **W. Gao, L. Dickinson, C. Grozinger, F. G. Morin and L. Reven.** "Self-Assembled Monolayers of Alkylphosphonic Acids on Metal Oxides." *In Langmuir*, 12(26) 6429–6435. **1996.**
- [195] **G. Guerrero, P. H. Mutin and A. Vioux.** "Organically modified aluminas by grafting and sol–gel processes involving phosphonate derivatives." *In Journal of Materials Chemistry*, 11(12) 3161–3165. **2001.**
- [196] **S. Lassiaz, A. Galarneau, P. Trens, D. Labarre, H. Mutin and D. Brunel.** "Organo-lined alumina surface from covalent attachment of alkylphosphonate chains in aqueous solution." *In New Journal of Chemistry*, 34(7) 1424–1435. **2010.**
- [197] **D. Massiot, B. Touzo, D. Trumeau, J. P. Coutures, J. Virlet, P. Florian and P. J. Grandinetti.** "Two-dimensional magic-angle spinning isotropic reconstruction sequences for quadrupolar nuclei." *In Solid State Nuclear Magnetic Resonance*, 6(1) 73–83. **1996.**
- [198] **F. Angeli, T. Charpentier, D. de Ligny and C. Cailleteau.** "Boron Speciation in Soda-Lime Borosilicate Glasses Containing Zirconium." *In Journal of the American Ceramic Society*, 93(9) 2693–2704. **2010.**
- [199] **C. A. Fyfe, K. T. Mueller, H. Grondey and K. C. Wong-Moon.** "Solid-state double-resonance NMR experiments involving quadrupolar and spin 1/2 nuclei." *In Journal of Physical Chemistry*, 97(51) 13 484–13 495. **1993.**

- [200] **P. Du, P. Yuan, A. Thill, F. Annabi-Bergaya, D. Liu and S. Wang.** “Insights into the formation mechanism of imogolite from a full-range observation of its sol-gel growth.” *In Applied Clay Science*, 150 115–124. **2017.**
- [201] **M. S. Amara, E. Paineau, S. Rouzière, B. Guiose, M.-E. M. Krapf, O. Taché, P. Launois and A. Thill.** “Hybrid, Tunable-Diameter, Metal Oxide Nanotubes for Trapping of Organic Molecules.” *In Chemistry of Materials*, 27(5) 1488–1494. **2015.**
- [202] **P. Picot, Y. Y. Liao, E. Barruet, F. Gobeaux, T. Coradin and A. Thill.** “Exploring hybrid imogolite nanotubes formation via Si/Al stoichiometry control.” *In Langmuir*, 34(44) 13 225–13 234. **2018.**
- [203] **Y. Liao, P. Picot, J.-B. Brubach, P. Roy, S. Le Caër and A. Thill.** “Self-supporting thin films of imogolite and imogolite-like nanotubes for infrared spectroscopy.” *In Applied Clay Science*. **2017.**
- [204] **A. Thill.** “Characterisation of Imogolite by Microscopic and Spectroscopic Methods.” *In Nanosized tubular clay minerals* (Edited by **P. Yuan, A. Thill and F. Bergaya**), *Developments in clay science*, volume 7, 223–253 (Elsevier, Amsterdam). **2016.**
- [205] **M. A. Wilson, G. S. Lee and R. C. Taylor.** “Tetrahedral rehydration during imogolite formation.” *In Journal of Non-Crystalline Solids*, 296(3) 172–181. **2001.**
- [206] **B. Creton, D. Bougeard, K. S. Smirnov, J. Guilment and O. Poncelet.** “Molecular Dynamics Study of Hydrated Imogolite. 1. Vibrational Dynamics of the Nanotube.” *In Journal of Physical Chemistry C*, 112(27) 10 013–10 020. **2008.**
- [207] **D. Boczula, A. Cały, D. Dobrzyńska, J. Janczak and J. Zoń.** “Structural and vibrational characteristics of amphiphilic phosphonate salts.” *In Journal of Molecular Structure*, 1007 220–226. **2012.**
- [208] **U. Dietze.** “Infrarotspektren von Phosphonsäuren. I Alkanphosphonsäuren.” *In Journal für Praktische Chemie*, 316(2) 293–298. **1974.**
- [209] **S. Szillies, P. Thissen, D. Tabatabai, F. Feil, W. Fürbeth, N. Fink and G. Grundmeier.** “Formation and stability of organic acid monolayers on magnesium alloy AZ31: The role of alkyl chain length and head group chemistry.” *In Applied Surface Science*, 283 339–347. **2013.**
- [210] **W. O. Yah, A. Takahara and Y. M. Lvov.** “Selective modification of halloysite lumen with octadecylphosphonic acid: new inorganic tubular micelle: new inorganic

- tubular micelle." *In Journal of the American Chemical Society*, 134(3) 1853–1859. **2012**.
- [211] **L. Peng, J. Yu, J. Li, Y. Li and R. Xu**. "Lamellar Mesostuctured Aluminophosphates: Intercalation of n-Alkylamines into Layered Aluminophosphate by Ultrasonic Method." *In Chemistry of Materials*, 17(8) 2101–2107. **2005**.
- [212] **G. Chaplais, J. Le Bideau, D. Leclercq, H. Mutin and A. Vioux**. "Novel aluminium phenyl, benzyl, and bromobenzylphosphonates: structural characterisation and hydration–dehydration reactions: structural characterisation and hydration–dehydration reactions." *In Journal of Materials Chemistry*, 10(7) 1593–1601. **2000**.
- [213] **P. F. Barron, M. A. Wilson, A. S. Campbell and R. L. Frost**. "Detection of imogolite in soils using solid state ^{29}Si NMR." *In Nature*, 299(5884) 616–618. **1982**.
- [214] **G. I. Yucelen, R. P. Choudhury, A. Vyalikh, U. Scheler, H. W. Beckham and S. Nair**. "Formation of single-walled aluminosilicate nanotubes from molecular precursors and curved nanoscale intermediates." *In Journal of the American Chemical Society*, 133(14) 5397–5412. **2011**.
- [215] **D. Y. Kang, J. Zang, E. R. Wright, A. L. McCanna, C. W. Jones and S. Nair**. "Dehydration, dehydroxylation, and rehydroxylation of single-walled aluminosilicate nanotubes." *In ACS Nano*, 4(8) 4897–4907. **2010**.
- [216] **D. Müller, W. Gessner, A. Samoson, E. Lippmaa and G. Scheler**. "Solid-state aluminium-27 nuclear magnetic resonance chemical shift and quadrupole coupling data for condensed AlO 4 tetrahedra." *In Journal of the Chemical Society, Dalton Transactions*, (6) 1277–1281. **1986**.
- [217] **A. Cabeza, M. A. G. Aranda, S. Bruque, D. M. Poojary, A. Clearfield and J. Sanz**. "Aluminum Phenylphosphonates: A Fertile Family of Compounds: A Fertile Family of Compounds." *In Inorganic Chemistry*, 37(17) 4168–4178. **1998**.
- [218] **J. E. Haky, J. B. Brady, N. Dando and D. Weaver**. "Synthesis and structural studies of layered aluminum phenylphosphonate." *In Materials Research Bulletin*, 32(3) 297–303. **1997**.
- [219] **S. Lassiaz, D. Labarre, A. Galarneau, D. Brunel and P. H. Mutin**. "Modification of silica by an organic monolayer in aqueous medium using octylphosphonic acid and aluminium species." *In Journal of Materials Chemistry*, 21(22) 8199–8205. **2011**.

- [220] **H. Tanaka, A. Yasukawa, K. Kandori and T. Ishikawa.** "Modification of Calcium Hydroxyapatite Using Alkyl Phosphates." *In Langmuir*, 13(4) 821–826. **1997.**
- [221] **H. Tanaka, T. Watanabe, M. Chikazawa, K. Kazuhiko and T. Ishikawa.** "Formation and structure of calcium alkyl phosphates." *In Colloids and Surfaces A: Physicochemical and Engineering Aspects*, 139(3) 341–349. **1998.**
- [222] **H. Tanaka and M. Chikazawa.** "Modification of amorphous aluminum phosphate with alkyl phosphates." *In Materials Research Bulletin*, 35(1) 75–84. **2000.**
- [223] **R. L. Parfitt, A. R. Fraser, J. D. Russell and V. C. Farmer.** "ADSORPTION ON HYDROUS OXIDES: II. OXALATE, BENZOATE AND PHOSPHATE ON GIBBSITE." *In Journal of Soil Science*, 28(1) 40–47. **1977.**
- [224] **M. B. McBride and L. G. Wesselink.** "Chemisorption of Catechol on Gibbsite, Boehmite, and Noncrystalline Alumina Surfaces." *In Environmental Science & Technology*, 22(6) 703–708. **1988.**
- [225] **T. J. van Emmerik, D. E. Sandstrom, O. N. Antzutkin, M. J. Angove and B. B. Johnson.** "³¹P solid-state nuclear magnetic resonance study of the sorption of phosphate onto gibbsite and kaolinite." *In Langmuir*, 23(6) 3205–3213. **2007.**
- [226] **C. V. Luengo, N. J. Castellani and R. M. Ferullo.** "Quantum chemical study on surface complex structures of phosphate on gibbsite." *In Spectrochimica Acta, Part A*, 147 193–199. **2015.**
- [227] **E. Laiti, P. Persson and L. O. Ohman.** "Balance between surface complexation and surface phase transformation at the alumina/water interface." *In Langmuir*, 14(4) 825–831. **1998.**
- [228] **G. Cao, H. G. Hong and T. E. Mallouk.** "Layered metal phosphates and phosphonates: from crystals to monolayers." *In Accounts of Chemical Research*, 25(9) 420–427. **1992.**
- [229] **H. Abe, T. Matsue and H. Yabu.** "Reversible Shape Transformation of Ultrathin Polydopamine-Stabilized Droplet." *In Langmuir*, 33(25) 6404–6409. **2017.**
- [230] **P. Aussillous and D. Quéré.** "Liquid marbles." *In Nature*, 411(6840) 924–927. **2001.**

- [231] **Y. Liu, X. Zhang, S. Poyraz, C. Zhang and J. H. Xin.** “One-Step Synthesis of Multifunctional Zinc-Iron-Oxide Hybrid Carbon Nanowires by Chemical Fusion for Supercapacitors and Interfacial Water Marbles.” *In ChemNanoMat*, 4(6) 546–556. **2018.**
- [232] **B. Bonelli.** “Surface Chemical Modifications of Imogolite.” *In Nanosized tubular clay minerals* (Edited by **P. Yuan, A. Thill and F. Bergaya**), *Developments in clay science*, volume 7, 279–307 (Elsevier, Amsterdam). **2016.**
- [233] **E. Paineau.** “Imogolite Nanotubes: A Flexible Nanoplatform with Multipurpose Applications.” *In Applied Sciences*, 8(10) 1921. **2018.**
- [234] **H. Lee, S. M. Dellatore, W. M. Miller and P. B. Messersmith.** “Mussel-inspired surface chemistry for multifunctional coatings.” *In Science*, 318(5849) 426–430. **2007.**
- [235] **J. H. Ryu, P. B. Messersmith and H. Lee.** “Polydopamine Surface Chemistry: A Decade of Discovery.” *In ACS Applied Materials & Interfaces*, 10(9) 7523–7540. **2018.**
- [236] **J. H. Waite and M. L. Tanzer.** “Polyphenolic Substance of *Mytilus edulis*: Novel Adhesive Containing L-Dopa and Hydroxyproline.” *In Science*, 212(4498) 1038–1040. **1981.**
- [237] **J. Liebscher, R. Mrówczyński, H. A. Scheidt, C. Filip, N. D. Hädade, R. Turcu, A. Bende and S. Beck.** “Structure of polydopamine: a never-ending story?” *In Langmuir*, 29(33) 10 539–10 548. **2013.**
- [238] **L.-S. Lin, Z.-X. Cong, J.-B. Cao, K.-M. Ke, Q.-L. Peng, J. Gao, H.-H. Yang, G. Liu and X. Chen.** “Multifunctional Fe₃O₄@Polydopamine Core–Shell Nanocomposites for Intracellular mRNA Detection and Imaging-Guided Photothermal Therapy.” *In ACS Nano*, 8(4) 3876–3883. **2014.**
- [239] **M. Martín, P. Salazar, R. Villalonga, S. Campuzano, J. M. Pingarrón and J. L. González-Mora.** “Preparation of core–shell Fe₃O₄@poly(dopamine) magnetic nanoparticles for biosensor construction.” *In Journal of Materials Chemistry B*, 2(6) 739–746. **2014.**
- [240] **B. N. Khlebtsov, A. M. Burov, T. E. Pylaev and N. G. Khlebtsov.** “Polydopamine-coated Au nanorods for targeted fluorescent cell imaging and photothermal therapy.” *In Beilstein Journal of Nanotechnology*, 10(1) 794–803. **2019.**

- [241] **W. Ye, H. Huang, W. Yang, X. Wang, C. Ren, Q. Hu, Y. Li and B. Ren.** "Ultrathin polydopamine film coated gold nanoparticles: a sensitive, uniform, and stable SHINERS substrate for detection of benzotriazole." *In Analyst*, 142(18) 3459–3467. **2017.**
- [242] **Y. S. Lee, J. Y. Bae, H. Y. Koo, Y. B. Lee and W. S. Choi.** "A remote-controlled generation of gold@polydopamine (core@shell) nanoparticles via physical-chemical stimuli of polydopamine/gold composites." *In Scientific Reports*, 6 22 650. **2016.**
- [243] **X. Du, L. Li, J. Li, C. Yang, N. Frenkel, A. Welle, S. Heissler, A. Nefedov, M. Grunze and P. A. Levkin.** "UV-triggered dopamine polymerization: control of polymerization, surface coating, and photopatterning." *In Advanced Materials*, 26(47) 8029–8033. **2014.**
- [244] **D. Nečas and P. Klapetek.** "Gwyddion: an open-source software for SPM data analysis." *In Open Physics*, 10(1) 99. **2012.**
- [245] **A. G. Williamson and N. F. Catherall.** "Mutual solubilities of propylene carbonate and water." *In Journal of Chemical & Engineering Data*, 16(3) 335–336. **1971.**
- [246] **P. Davidson and I. Dozov.** "Liquid-Crystalline Phases of Imogolite and Halloysite Dispersions." *In Nanosized tubular clay minerals* (Edited by **P. Yuan, A. Thill and F. Bergaya**), *Developments in clay science*, volume 7, 308–330 (Elsevier, Amsterdam). **2016.**
- [247] **E. Paineau, M.-E. M. Krapf, M.-S. Amara, N. V. Matskova, I. Dozov, S. Rouzière, A. Thill, P. Launois and P. Davidson.** "A liquid-crystalline hexagonal columnar phase in highly-dilute suspensions of imogolite nanotubes." *In Nature Communications*, 7 10 271. **2016.**
- [248] **B. Creton, D. Bougeard, K. S. Smirnov, J. Guilment and O. Poncelet.** "Structural Model and Computer Modeling Study of Allophane." *In Journal of Physical Chemistry C*, 112(2) 358–364. **2008.**
- [249] **K. Shikinaka, K. Kaneda, S. Mori, T. Maki, H. Masunaga, Y. Osada and K. Shigehara.** "Direct Evidence for Structural Transition Promoting Shear Thinning in Cylindrical Colloid Assemblies." *In Small*, 10(9) 1813–1820. **2014.**
- [250] **W. Abdelwahed, G. Degobert, S. Stainmesse and H. Fessi.** "Freeze-drying of nanoparticles: Formulation, process and storage considerations." *In Advanced Drug Delivery Reviews*, 58(15) 1688–1713. **2006.**

- [251] **K. S. Tang, S. M. Hashmi and E. M. Shapiro.** “The effect of cryoprotection on the use of PLGA encapsulated iron oxide nanoparticles for magnetic cell labeling.” *In Nanotechnology*, 24(12) 125 101. **2013.**

Titre: Précipitation confinée en gouttes - Développement d'approches microfluidique et émulsion Pickering à base d'imogolite

Mots clés: OSTE+; in situ SAXS; modification de surface; acide alkylphosphonique

Résumé: Dans de nombreux secteurs industriels tels que la production de pigments, de catalyseurs, de produits pharmaceutiques, de minerais ou le recyclage de combustibles nucléaire, les étapes de précipitation et de cristallisation sont cruciales. Bien que ces procédés soient utilisés à grandes échelles avec un contrôle relatif des solides formés, les mécanismes de formation ne sont pas toujours bien compris, en particulier à l'échelle microscopique. Une meilleure compréhension des différentes étapes de formation permettrait d'obtenir des leviers de contrôle adaptés à chaque composé et application.

Cette thèse se place dans ce cadre très général du contrôle de la précipitation et plus particulièrement de la précipitation en gouttes d'émulsion eau dans l'huile. Deux approches différentes ont été explorées pour moduler et suivre la réactivité dans une goutte d'émulsion. La première approche était basée sur le couplage d'une puce microfluidique générateur de gouttes avec la diffusion de rayons X aux petits angles (SAXS) in situ. Après une caractérisation complète de la compatibilité du polymère non stœchiométrique thiol-ene-epoxy (OSTE+) avec le SAXS, une puce en OSTE+ compatible avec le suivi in situ SAXS a été développée. Un traitement original permettant d'extraire séparément le signal des gouttes du signal de l'huile a permis de valider le montage dans le cas de la précipitation d'oxalate de cérium. La deuxième approche avait pour but l'utilisation de nanotubes d'imogolites pour stabiliser des gouttes d'émulsion et étudier le transport de réactifs entre gouttes via ces nanotubes. Cette approche nécessitait de fonctionnaliser les nanotubes pour les rendre hydrophobe. La caractérisation poussée de la fonctionnalisation des imogolites par des alkylphosphoniques a montré pour la première fois que cette réaction ne conduisait pas à une fonctionnalisation de surface mais à un matériau composite aux propriétés interfaciales remarquables. De nouvelles voies de fonctionnalisation de surface ont été développées pour rendre les imogolites hydrophobes.

Title: Precipitation in Confined Droplets - Development of Microfluidic and Imogolite Pickering Emulsion Approaches

Keywords: OSTE+; in-situ SAXS; surface modification; alkylphosphonic acid

Abstract: Precipitation and crystallization play a fundamental role in the industrial production of pigments, catalysts, plant protection agents, nuclear fuel and pharmaceuticals. Although these processes are often applied and a relative control over the formed solids can be achieved, they are not always well understood on a microscopic level. Identification of how the solids are formed and which mechanisms govern their formation, potentially gives the capabilities to better control such processes.

In this thesis, two different approaches are explored to study precipitation and crystallization by confining reactions into droplets. The first approach focuses on the combination of a droplet microfluidic device and in-situ small angle X-ray scattering. An off-stoichiometry thiol-ene-epoxy polymer is characterized for the use with in-situ X-ray scattering and a protocol is presented to prepare suitable microfluidic devices from this material. An original approach to isolate the scattering signal of the carrier phase and the droplets is then used to study the precipitation of cerium oxalate in droplets. The second approach aims to use imogolite nanotubes to stabilize droplets against coalescence and to study their transport properties to control reactant feeding into droplets. By fully characterizing the necessary surface modification by alkylphosphonic acids for the first time, evidence is found that the reaction does not yield surface modified tubes. Consequentially, new approaches are explored to obtain individually dispersed imogolite nanotubes with a hydrophobic surface.

